Short duration presynaptic action potentials shape calcium dynamics and transmitter release at the neuromuscular junction in healthy and diseased states

by

Scott Patrick Ginebaugh

B.S., Wayne State University, 2016

Submitted to the Graduate Faculty of the

School of Medicine in partial fulfillment

of the requirements for the degree of

Doctor of Philosophy

University of Pittsburgh

2021

UNIVERSITY OF PITTSBURGH

SCHOOL OF MEDICINE

This dissertation was presented

by

Scott Patrick Ginebaugh

It was defended on

January 27, 2021

and approved by

James R. Faeder, Ph.D., Associate Professor, Department of Computational and Systems Biology, University of Pittsburgh

Zachary Freyberg, M.D., Ph.D., Assistant Professor, Department of Psychiatry, University of Pittsburgh

Ivet Bahar, Ph.D., Distinguished Professor & John K. Vries Chair, Department of Computational and Systems Biology, University of Pittsburgh

Rozita Laghaei, Ph.D., Research Scientist, Pittsburgh Supercomputing Center, Carnegie Mellon University

Dissertation Director: Stephen D. Meriney, Ph.D., Professor, Department of Neuroscience, University of Pittsburgh

Short duration presynaptic action potentials shape calcium dynamics and transmitter release at the neuromuscular junction in healthy and diseased states

Scott Patrick Ginebaugh, PhD

University of Pittsburgh, 2021

The action potential (AP) waveform controls the opening of voltage-gated calcium channels (VGCCs) at presynaptic nerve terminals. The calcium ion flux through these VGCCs acts as a second messenger, triggering the release of neurotransmitter. The frog and mouse neuromuscular junctions (NMJs) have long been model synapses for the study of neurotransmission, but the presynaptic AP waveforms from these NMJs have never been recorded because the nerve terminals are too small impale with an electrode for electrophysiological recordings. Neurotransmission from nerve terminals occurs at highly organized structures called active zones (AZs), and the relationships between the AP, VGCCs, and neurotransmission at AZs are poorly understood. Understanding these relationships is important for the study of Lambert-Eaton myasthenic syndrome (LEMS), an autoimmune disorder in which neurotransmitter release from the NMJ is decreased, leading to severe muscle weakness. This reduced neurotransmission is thought to be caused by an antibody-mediated removal of presynaptic VGCCs and disruption of AZ structure. Furthermore, 3,4-diaminopyridine (3,4-DAP; the FDA-approved treatment for LEMS) was thought to indirectly increase calcium flux into the AZs by broadening the presynaptic AP, but this mechanism has come under scrutiny. Here, we use voltage imaging to optically record AP waveforms from frog and mouse motoneuron terminals. We find that the AP waveforms from these terminals are very brief in duration. We hypothesize the brief duration of these APs helps prevent a depletion of docked synaptic vesicles in AZs by limiting calcium flux during APs, and is thus an important mechanism by which healthy NMJs maintain reliable neurotransmission during repeated stimulation. We also show that clinically relevant concentrations of 3,4-DAP increase calcium flux by broadening the AP. Next, we use our recorded AP waveforms to constrain computational models of mammalian AZs, and utilize these models to investigate the effects of LEMS on the AZ. We demonstrate that the disruption of AZ structure plays an essential role in LEMS pathology. Finally, we show that disrupting the calcium-sensing proteins in the AZ could result in LEMS pathology and hypothesize that anti-VGCC antibodies may not be solely responsible for LEMS in many LEMS patients.

Table of Contents

List of Tables

List of Figures

Preface

I would first and foremost like to thank Dr. Meriney for his knowledge, patience, and enthusiasm about research that helped me become a better scientist. I would also like to thank Dr. Laghaei for advising me on computational methods and teaching me how to use MCell, Dr. Hukriede for creating and directing the Integrative Systems Biology program, Shari Murphy for keeping the ISB program running, all the members of the Meriney Lab for their friendship and understanding, my undergraduate minions for keeping me company during voltage-imaging experiments, and my family for their continual support.

1.0 Introduction

Neurons are the primary cell type of the nervous system. They communicate with other cells via an electrochemical signal, where a wave of electrical energy, referred to as the action potential (AP), is sent from the cell body to the presynaptic terminal of the axon. Upon reaching the axon terminal, the AP causes voltage-gated calcium channels (VGCCs) to open, and a subsequent influx in calcium ions. These calcium ions act as a second-messenger, binding to calcium-sensing proteins. The activation of these proteins then causes neurotransmitter-containing docked synaptic vesicles to release their contents into the synaptic cleft, which causes a chemical signal to be transmitted to the cell on the postsynaptic side of the synaptic cleft.

Neurons in the central nervous systems can contain thousands of connections to other neurons, which can result in complex modulation of the mechanisms responsible for neurotransmission. In contrast, the motoneurons of the spinal cord, which allow the nervous system to control muscle contraction, have a one-to-one connection between presynaptic nerve terminals and postsynaptic muscle cells. For this reason, in addition to their large size, motoneuron synapses onto muscle fibers, called neuromuscular junctions (NMJs), have been a model for the study of synaptic transmission.

Release of neurotransmitter from the presynaptic terminals of neurons occurs at specialized regions of the presynaptic membrane called active zones (AZs), which contain docked synaptic vesicles, VGCCs, and a variety of structural, membrane fusion facilitating, and calcium-sensing proteins. The function of the AZ is essential to the ability of the neuron to release neurotransmitter, and several diseases and toxins impact the ability of the AZ to function properly. One such disease that targets the NMJ is Lambert-Eaton Myasthenic syndrome (LEMS).

LEMS is a rare autoimmune-mediated neuromuscular disease in which the immune system attacks the VGCCs in the AZ (as well as other AZ proteins). The decrease in the number of VGCCs leads to a reduced calcium influx during an AP, and a subsequent reduction in the amount of neurotransmitter that is released. This reduction in transmitter release results in severe muscle weakness. Recently, the FDA has approved 3,4-diaminopyridine (3,4-DAP) for the treatment of LEMS, which indirectly augments calcium ion flux into the terminal, thereby increasing transmitter release. However, treatment with 3,4-DAP only results in a modest improvement in symptoms for LEMS patients.

In this chapter, many topics will give a brief overview in terms of the nervous system as a whole and then will focus on the neuromuscular junction. The mouse and frog neuromuscular junctions will be a particular focus, as these are the model organisms used for research in this dissertation. Chapter 2 has been published in the Journal of Neuroscience (Ginebaugh et al., 2020), chapter 3 has been published in the Journal of Biological Chemistry (Ojala et al., 2021), and chapter 4 is expected to be submitted for publication in the near future.

1.1 Action potential propagation in neurons

All cells are surrounded by a lipid membrane. The difference in ion concentrations inside and outside of this membrane causes it to act as a capacitor, resulting in a voltage across the membrane. Multiple cell types, including muscle cells, neurons, and some endocrine cells, utilize this transmembrane voltage as a means to communicate information throughout the cell. In general, the voltage is communicated along the length of the cell membrane primarily through voltage-gated sodium channels and voltage-gated potassium channels (and, to a lesser extent, VGCCs), which control the flux of charged ions into and out of the cell. The electrical signal mediated via the voltage-gated sodium and potassium channels is a wave of depolarizing membrane voltage that triggers an all-or-none voltage spike, known as the action potential (AP).

The AP is often considered as a binary signal broadcasting throughout the nerve, causing a release of neurotransmitter into the synapse upon reaching the axon terminal (Burkitt, 2006; Lapicque, 2007; Rowan et al., 2016). However, since the analysis of the squid giant axon action potential by Hodgkin and Huxley (Hodgkin & Huxley, 1939, 1945, 1952a, 1952b, 1952c, 1952d, 1952e; Hodgkin, Huxley, & Katz, 1952), it has become clear that the AP waveform itself is an important part of the computation of the neuron. The size, shape, and conduction velocity of the AP play an important role in determining the function of the neuron. The AP is not a binary pulse, but in fact its properties (amplitude, shape, and conduction velocity) can vary greatly between different types of neurons and between different parts of a neuron as it propagates. Neurons regulate the propagation and shape of the AP with a heterogeneous distribution of ion channels and a variety of feedback mechanisms.

Despite the importance of the AP waveform shape and propagation to the function of nerves and synapses, the shape of the AP waveform and how changes in this waveform impact the behavior of neurons are relatively understudied. This is primarily due to the fact that the axons and dendrites of most neurons are too small to probe with an electrode (with a few notable exceptions such as the squid giant axon). Therefore, standard electrophysiology techniques can generally only be used in the soma of neurons, and cannot be used to record propagation of the AP throughout the cell.

1.2 The active zone

Active zones (AZs) are specialized structures on the presynaptic plasma membrane of synapses where neurotransmitter release occurs (Couteaux & Pecot-Dechavassine, 1970; Sudhof, 2012). Early imaging studies showed that AZs contain docked synaptic vesicles and numerous intramembranous particles (Heuser, Reese, & Landis, 1974; Peper et al., 1974; Pfenninger et al., 1972). These intramembranous proteins are comprised of the structural and functional proteins necessary for synaptic vesicle exocytosis, as well as ion channels such as VGCCs.

When an AP invades the presynaptic terminal, the VGCCs convert the electrical signal to a calcium-ion second messenger signal. These calcium ions then bind to calcium-sensing proteins, which trigger transmitter-containing vesicle fusion with the plasma membrane. Although many of the core components of the AZ are evolutionarily conserved, the specific types of particular proteins (e.g. voltage-gated calcium channels, calcium-sensing protein subtypes), as well as the structure of the AZ can vary significantly between (and even within) different species and neuronal subtypes (Sudhof, 2012). These differences in AZ structure can greatly affect the function of the neuron, including the latency and amount of neurotransmitter released during an AP as well as the plasticity of the synapse during repeated stimulation (Baydyuk, Xu, & Wu, 2016; Laghaei et al., 2018; Slater, 2015). Thus, these differences in AZ structure result in differences in the information-transmitting properties of the neurons.

1.2.1 Voltage-gated calcium channels

Among the intramembranous proteins in the AZ, one of the most important types for the synchronous (AP-triggered) release of neurotransmitter are the VGCCs. These channels play an important role in converting the electrical AP waveform to a chemical signal of calcium ions which act as a messenger to trigger vesicle fusion. Although VGCCs exist both within and outside the AZ, the presence of VGCCs inside the AZ is essential for a rapid release of neurotransmitter following an AP (Eggermann et al., 2011; Kaeser & Regehr, 2014).

VGCCs are comprised of a pore-forming α1 subunit, as well as α2, β, γ, and δ auxiliary subunits (differentially present depending on the sub-type of calcium channel). Although variation in the auxiliary subunits can cause physiological changes in the channel, the variation in the α1 subunit is the primary determinant of the channel behavior. The α1 subunit is a 190 kDa protein comprised of ~2000 amino acid residues, which form four repeated domains (I-IV) each containing six transmembrane segments (S1-S6) (Takahashi et al., 1987; Tanabe et al., 1987). During a depolarization of the membrane, the S4 segment acts as the voltage sensor responsible for voltage-mediated activation of the channel (Bezanilla, 2000; Catterall, 2010, 2011).

There are 10 different α1 subunits, which are classified into three families (Ca_v1, Ca_v2, Ca_v3) based on structural and functional characteristics (Ertel et al., 2000; Snutch & Reiner, 1992). The α1 subunits in each family are subdivided into different calcium current types according to the electrophysiological and pharmacological properties of the currents and the channels that cause them. These calcium current subtypes are referred to as L-type ($Ca_v1.1$, 1.2, 1.3, and 1.4), P/Q-type ($Ca_v2.1$), N-type ($Ca_v2.2$), R-type ($Ca_v2.3$), and T-type ($Ca_v3.1$, 3.2, and 3.3) (Catterall, 2011). L-type currents were the first to be discovered, and are characterized in part by large conductance, slow voltage-dependent inactivation, high voltage of activation, and sensitivity to dihydropyridines (Reuter, 1979; Tsien, 1983). They also display calcium-dependent inactivation (Hofer et al., 1997; Imredy & Yue, 1994). T-type channels have small channel conductance, rapid activation, and low voltage of activation, and are particularly utilized by neurons for repetitive firing and peacemaking purposes (Catterall, 2011). P/Q-, N-, and R-type channels are more rapid than L- and T-type and are often used in neurons for coupling of excitation to rapid neurotransmitter release. P/Q-type channels are sensitive to the spider toxin ω-agatoxin IVA (Mintz et al., 1992). Furthermore, some subtypes of P/Q-type channels demonstrate calcium-dependent modulation of channel properties (Forsythe et al., 1998; Lee et al., 1999). N-type are selectively blocked by the cone snail toxin ω-conotoxin GVIA (Olivera et al., 1994; Tsien et al., 1988). R-type channels are sensitive to the peptide SNX-482 (Newcomb et al., 1998).

A majority of synapses utilize P/Q-type or N-type channels to trigger release of neurotransmitter. Among these are the mouse NMJ, which utilizes mainly P/Q-type VGCCs (Katz et al., 1997) for fast exostosis, and the frog NMJ which utilizes mainly N-type VGCCs (Katz et al., 1995). However, when the AP waveform is altered in the mouse NMJ with drug treatments, other types of VGCCs such as N-type (Giovannini et al., 2002) or L-type (Flink & Atchison, 2003) may also contribute to transmitter release. Furthermore, experiments on knockout mice without the ability to produce P/Q-type VGCCs have shown that compensatory mechanisms exist to replace missing VGCC types with other VGCC types (Urbano et al., 2003). This is also evident of these compensatory mechanisms in some diseases that result in removal of a VGCC subtype (see section 1.3).

1.2.2 Calcium-activated potassium channels

Another type of ion channel that is found in some active zones is the calcium-activated potassium channel. Calcium-activated potassium channels are generally separated into three different subtypes: “big-conductance” (BK), “small-conductance” (SK), and “intermediate-conductance” (IK). These channels are found throughout the nervous system and have a variety of functions. SK and IK channels differ from BK channels because SK and IK channels are activated by intracellular calcium independently of membrane voltage, whereas BK channels are activated by a combination of membrane voltage and intracellular calcium (Kshatri, Gonzalez-Hernandez, & Giraldez, 2018; Yang, Zhang, & Cui, 2015). Here, we will focus primarily on BK channels because they localize within AZs at NMJs (Robitaille et al., 1993b).

BK channels activate rapidly enough to have an effect on the repolarization phase of APs (Pattillo et al., 2001; Sun, Yazejian, & Grinnell, 2004). This, along with evidence from calcium buffer experiments, shows that BK channels are located within nanometers of VGCCs (Fakler & Adelman, 2008). Recent research has proposed a mechanism for this colocalization: RIM-binding proteins (evolutionarily conserved AZ proteins) bind to both VGCCs and BK channels and localize them to the AZ (Sclip et al., 2018). The ability of BK channels to affect the AP waveform and to colocalize with VGCCs in the AZ suggests that BK channels are part of an important feedback mechanisms by which VGCCs, which open in response to an AP, can modify the AP waveform (Fakler & Adelman, 2008; Lee & Cui, 2010).

Blocking BK channels has been shown to increase transmitter release at both mature frog (Anderson et al., 1988; Flink & Atchison, 2003; Robitaille & Charlton, 1992; Robitaille et al., 1993b) and mouse NMJs (Anderson et al., 1988; Vatanpour & Harvey, 1995). However, BK channels are present, but decrease transmitter release when blocked, at *Xenopus* nerve-muscle co-cultures (Pattillo et al., 2001) and do not affect transmitter release during single APs at *Drosophila* NMJs (Ford & Davis, 2014), suggesting that BK channels can have a variable and complex relationship with VGCCs, APs, and transmitter release that is not fully understood. Because there is a large amount of variability in BK channel effects between synapses, this suggests that BK organization in the AZ may be variable between synapses (Ford & Davis, 2014; Pattillo et al., 2001; Robitaille et al., 1993b; Vatanpour & Harvey, 1995).

1.2.3 Active zone proteins contributing to calcium sensing and vesicle release

The minimal machinery necessary for vesicle exocytosis is the SNARE (soluble N-ethylmaleimide-sensitive factor attachment proteins receptor) complex. This complex contains target-membrane associated SNARE proteins and a vesicle associated SNARE protein. The target-membrane associated SNARE proteins are synatxin-1 and synaptosomal-associated protein of 25 kDa (SNAP-25), and the vesicle associated SNARE protein is vesicle-associated protein synaptobrevin (VAMP) (Sollner et al., 1993; Sudhof, 2012). However, the SNARE complex by itself cannot create the rapid and tightly regulated vesicle release seen at the AZ. For this to occur, several other proteins must interact with the SNARE complex (Hayashi et al., 1994; Sudhof, 2012, 2013). Among these other proteins, the calcium sensing proteins necessary to help accelerate the vesicle fusion process are the most relevant to this work.

There are multiple types of calcium sensing proteins that can contribute to vesicular release, the most important group of which are the proteins of the synaptotagmin family. Mammals express 17 isoforms of synaptotagmin (Dean et al., 2012; MacDougall et al., 2018), 8 of which bind calcium (Gustavsson & Han, 2009). Of these, synaptotagmin-1 is known to be the main calcium sensor for fast calcium-dependent vesicle release at a variety of synapses, and is the most well-studied of the synaptotagmin family (Martens, Kozlov, & McMahon, 2007). In brief, upon being activated by bound calcium, the synaptotagmin-1 interacts with the SNARE complex to significantly accelerate the vesicle fusion process. This allows for the rapid release of transmitter following and AP-mediated influx of calcium. Synaptotagmin-2 is less well studied than synaptotagmin-1, but is thought to act similarly (Pang et al., 2006b). There is evidence that both synaptotagmin-1 and synaptotagmin-2 are present in the AZs of mouse NMJs (Pang et al., 2006a).

For some time, it has been hypothesized that the existence of a second calcium sensor could be responsible for facilitation seen at a variety of synapses (Yamada & Zucker, 1992). Recently, a series of knock-out experiments showed that eliminating synaptotagmin-7 resulted in a loss in synaptic facilitation, and thus this second sensor was identified to be synaptotagmin-7 (Jackman et al., 2016). Compared to synaptotagmin-1, synaptotagmin-7 is vastly understudied, but it has gained a considerable amount of attention since its discovery as the second calcium sensor. It is now understood that synaptotagmin-7 is responsible for short-term facilitation at a variety of synapses. Synaptic facilitation (an increase in the probability of transmitter release after prior activity) is hypothesized to be controlled by a calcium sensor with very slow kinetics for binding and unbinding calcium (Yamada & Zucker, 1992). Synaptotagmin-7 is an attractive candidate because it appears to have a calcium binding off rate of approximately 6 times slower than synaptotagmin-1 (Hui et al., 2005; Jackman & Regehr, 2017). As a result, synaptotagmin-7 can remain activated and contribute to vesicle release over the course of several APs. However, the mechanism by which synaptotagmin-7 contributes to vesicular release is not yet fully understood, and synaptotagmin-7 also appears to have a variety of other functions (Chen et al., 2017; Luo & Sudhof, 2017). To contribute to synaptic facilitation, it is possible that synaptotagmin-7 interacts with the SNARE complex in a manner similar to that proposed for synaptotagmin-1, but it has also been hypothesized to act through different mechanisms such as altering the interaction between synaptotagmin-1 and the SNARE complex (Jackman et al., 2016).

1.2.4 Coupling of active zone components

For synaptic vesicle fusion to occur following the invasion of the AP into the presynaptic terminal, the VGCCs must open, calcium must flow in and diffuse from the VGCC to the calcium sensor, and the calcium sensor must then trigger the fusion of the vesicle with the plasma membrane. At fast synapses such as the NMJ, this process occurs in less than a millisecond (Eggermann et al., 2011; Katz & Miledi, 1965a; Llinas, Steinberg, & Walton, 1981; Sabatini & Regehr, 1996).

It is a known physical law that diffusion time is proportional to the square of the distance. Based on the low latency between influx of calcium and the subsequent release of transmitter at fast synapses, the VGCCs must be within 100 nm of the calcium sensing proteins (Stanley, 2016). The intraterminal cytoplasmic volume immediately surrounding the opening of a single VGCC is often referred to as the calcium nanodomain. Following an AP, a high density of calcium ions will rapidly fill the nanodomain region. This density can be high enough such that a single VGCC can cause calcium-mediated fusion of synaptic vesicles in its nanodomain (although this is a low probability event (Luo et al., 2015)). In contrast, multiple VGCCs located near each other (but not necessarily within nanodomain distance) can create a high-density cloud of calcium in the volume around the VGCC cluster. This region is known as the microdomain, and can extend from 100 nm to 1 μm (Eggermann et al., 2011; Neher & Sakaba, 2008). For transmitter release to be triggered by a calcium microdomain, multiple VGCCs must open to create a sufficiently high concentration of calcium.

In the nanodomain, the fast calcium buffer BAPTA is able to bind calcium ions before they trigger vesicle release by activating calcium sensing proteins, whereas the slow calcium buffer EGTA is not. In the microdomain however, both EGTA and BAPTA can prevent calcium from causing vesicle release. Thus, buffer experiments using BAPTA and EGTA can reveal if vesicular fusion is triggered by nanodomain or microdomain coupling with VGCCs (Adler et al., 1991; Stanley, 2016).

Both nanodomains and microdomain coupling can be effective for inducing transmitter release, and the primary coupling type differs between different types of neurons (Stanley, 2016). Interestingly, at the rodent Calyx of Held the preference appears to shift from microdomain coupling in neonates towards tighter nanodomain coupling in adults (Fedchyshyn & Wang, 2005). However, at the healthy frog NMJ, where speed is a priority, experimental results have consistently shown nanodomain coupling of VGCCs located close to vesicles as the cause of transmitter release (Heuser & Reese, 1981; Luo et al., 2015; Wachman et al., 2004)

1.3 Properties of the neuromuscular junction

Neuromuscular junctions (NMJs) are essential for movement, and thus are essential for most animal life. Because of the this, NMJs have evolved a variety of properties allowing them to function under a wide range of conditions. Two important such properties are the strength and reliability of NMJs. Here, strength refers to the fact that a typical presynaptic AP will cause a release of transmitter in excess of what is necessary to lead to the contraction of the postsynaptic muscle fibers, ensuring muscle activation. Reliability refers to the fact that the NMJ can repeatedly stimulate, or cause sustained contraction of, the postsynaptic muscle fibers (Meriney & Dittrich, 2013; Wood & Slater, 2001).

1.3.1 The frog neuromuscular junction

The frog NMJ has been used for decades as a model synapse for NMJs as well as for the study of neurotransmission as a whole. Notably, the Nobel Prize winning work elucidating the nature of neurotransmission by Katz and colleagues was performed in the frog NMJ (Del Castillo & Katz, 1957a, 1957b, 1957c; Del Castillo & Katz, 1957d; Katz & Thesleff, 1957a, 1957b). The frog NMJ is used as a model synapse for several reasons: its size and accessible location (often on top of the muscle fibers) make it easy to study, and its one-to-one presynaptic terminal to postsynaptic muscle fiber ratio make it so deconvolution of multiple inputs is not necessary to interpret experimental results from muscle fibers.

A single frog NMJ contains approximately 600 AZs (Figure 1A) (Laghaei et al., 2018). Each AZ is a highly organized structure comprised of two rows with a total of 20-40 docked synaptic vesicles. The gap between the vesicles contains two double rows of intramembranous particles, with each double row placed close to a row of vesicles, containing a total of approximately 200-250 intramembranous particles per AZ (Figure 1B) (Heuser et al., 1979; Heuser et al., 1974; Pawson, Grinnell, & Wolowske, 1998a). Despite the presence of 12,000-24,000 docked vesicles in the approximately 600 AZs, an average AP causes a release of neurotransmitter from only 415 vesicles (Laghaei et al., 2018). This means that during an AP, each AZ has a 0.67 probability of releasing transmitter from a synaptic vesicle. Assuming an average of 30 docked synaptic vesicles per AZ, then the probability of any given vesicle released its neurotransmitter during an AP is only 0.022. However, this low number of vesicles released during an AP, as compared with how many vesicles are ready to be released, is still significantly more than what is required to elicit a muscle contraction (Wood & Slater, 2001).

More recent research using single pixel optical fluctuation analysis on calcium imaging suggests that of the 200-250 intramembranous particles in the frog AZ, only 30-40 of them are VGCCs. This suggests a one-to-one relationship between docked synaptic vesicles and VGCCs. Furthermore, calcium imaging found that calcium channels in the frog AZ have only a 0.2 probability of opening during an AP (Luo et al., 2015; Luo et al., 2011). Thus, only approximately 7 VGCCs would be expected to open in each AZ of the frog NMJ during an AP. This paucity of VGCCs combined with the low probability of VGCCs opening during an AP provides a mechanism which can explain the low probability of release for synaptic vesicles. The resulting unreliable vesicle release per AZ is thought to contribute to the reliability of the synapse as a whole by ensuring that, even during repeated stimulation, the synapse will not become depleted of docked synaptic vesicles.

1.3.2 The murine neuromuscular junction

The mouse (and sometimes rat) NMJ is also often use as a model synapse, particularly because mice are much closer in physiology to the human NMJ than the frog or other model organisms like crayfish or *Drosophila*. Whereas the frog NMJ has a long, linear shape with long, linear AZs, the mouse NMJ has a “pretzel” shape with much smaller AZs (Figure 1C). Each AZ generally contains a row of 2 docked synaptic vesicles surrounded on both sides by double rows of intramembranous particles, containing approximately 20 particles total (Figure 1D) (Fukuoka et al., 1987; Nagwaney et al., 2009). The average mouse NMJ contains approximately 700 of these smaller AZs (Laghaei et al., 2018), each placed approximately 500 nm apart (Ruiz et al., 2011). During a single AP, the mouse NMJ releases approximately 160 vesicles of neurotransmitter. This corresponds to a 0.22 probability of release from any given AZ during an AP, and a 0.11 probability of release per synaptic vesicle (Laghaei et al., 2018).

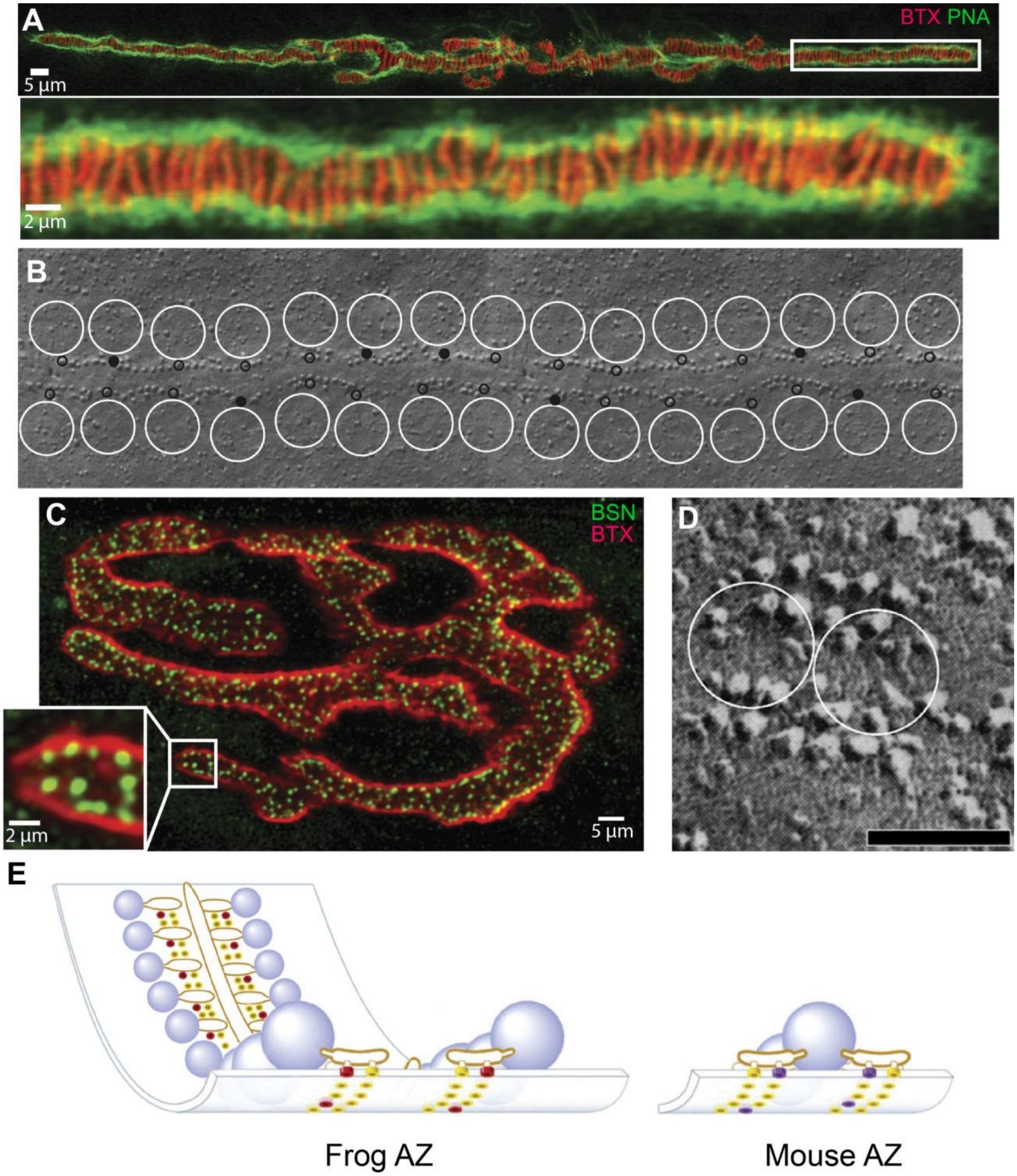

Figure 1 The stucture of the frog and mouse NMJs and their AZs.

A, A frog NMJ stained with Alexa-594 α-bungarotoxin (BTX; red) to show the approximate location of AZs by staining postsynaptic acetylcholine receptors and Alexa-488 peanut lectin (PNA; green) to outline the synapse. Image from (Laghaei et al., 2018). **B**, A freeze-fracture replica of an AZ from a frog NMJ. The hypothesized locations of synaptic vesicles are superimposed as white circles, and the hypothesized location of VGCCs are superimposed as black circles. The filled black circles represent the number of VGCCs predicted to open after a single AP. Original freeze-fracture image from (Heuser & Reese, 1981), and the adapted image from (Luo et al., 2011). **C**, A mouse NMJ stained with Alexa-594 α-bungarotoxin (BTX; red) to show the shape of the NMJ and an Alexa-488 conjugated antibody to identify the bassoon protein the AZs (BSN; green). Image from (Laghaei et al., 2018). **D**, A freeze-fracture replica of an AZ from a mouse NMJ. The hypothesized locations of synaptic vesicles are superimposed as white circles. Scale bar = 50 nm. Adapted from (Nagwaney et al., 2009) and (Fukuoka et al., 1987). **E**, Diagrams of a single AZ from a frog NMJ (left) and mouse NMJ (right). Diagram shows docked synaptic vesicles (blue spheres), N-type VGCCs in the frog AZ (red disks), P/Q-type VGCCs in the mouse AZ (purple disks), and other intramembranous AZ particles (yellow disks). Adapted from (Laghaei et al., 2018) and originally from (Urbano et al., 2003), copyright (2003) National Academy of Sciences.

1.4 Lambert-Eaton Myasthenic Syndrome

1.4.1 Clinical properties

Lambert-Eaton myasthenic syndrome (LEMS) is an autoimmune-mediated neuromuscular disease which results from the immune system targeting AZs proteins at the NMJ, mainly by producing antibodies targeting P/Q-type VGCCs. LEMS is a rare disease with a prevalence of 3.4 cases per million people (Titulaer, Lang, & Verschuuren, 2011a). LEMS is often considered a paraneoplastic syndrome because 50-60% of cases are associated with small-cell lung carcinoma (Titulaer et al., 2011b), and in rare cases has been associated with other malignancies such as non-small cell lung carcinoma (Wirtz et al., 2002) and prostate carcinoma (Titulaer & Verschuuren, 2008). Paraneoplastic instances of LEMS tend to be associated with older, male patients with a long-term history of smoking, whereas idiopathic LEMS patients tend to be younger and are more likely to be female. In almost all paraneoplastic LEMS cases, LEMS symptoms precede the diagnosis of small-cell lung carcinoma, and LEMS patients are routinely screened for lung cancer after their LEMS diagnosis (Titulaer et al., 2011a). The paraneoplastic relationship of LEMS with small-cell lung carcinoma is due to the fact that small-cell lung carcinomas are neuroendocrine in origin (Kalemkerian et al., 2013) and tend to overexpress VGCCs as well as other AZ proteins (David et al., 1993). Thus, paraneoplastic LEMS is a result of the immune system response to the tumor (Roberts et al., 1985).

LEMS is diagnosed based on clinical symptoms, electrophysiological measurements, and tests for the presence of antibodies (Kesner et al., 2018; Titulaer et al., 2011a). The primary symptom of LEMS is severe muscle weakness. It tends to start in the proximal legs and then spreads to the proximal arms, followed by the distal limbs and cranial muscles (Schoser et al., 2017). LEMS is often associated with decreased tendon reflexes, and is frequently associated with autonomic dysfunction including dry mouth, constipation, and erectile dysfunction. Symptoms tend to progress faster in paraneoplastic LEMS than in idiopathic LEMS (Titulaer et al., 2011a).

Repeated nerve stimulation tests using electromyography are often utilized for the diagnosis of LEMS. EMG tests of LEMS patients often display three primary findings: a reduced compound muscle AP amplitude at rest, a decrease in response over time during low-frequency repetitive nerve stimulation, and an increase in response over time during high-frequency repetitive nerve stimulation (Eaton & Lambert, 1957). However, these typical electrophysiological properties are not seen in all LEMS patients, and other tests such as examining post-exercise facilitation are also used (Oh, 2016; Oh et al., 2007).

The presence of antibodies targeting P/Q-type VGCCs is thought to support a LEMS diagnosis (Vincent, Lang, & Newsom-Davis, 1989), but is not a complete explanation of the immune nature of LEMS. Although anti-P/Q-type VGCCs are the most common antibody type, they are only present in 80-95% of LEMS patients (Kesner et al., 2018; Lennon et al., 1995; Motomura et al., 1997; Takamori et al., 1995). However, injection of serum from LEMS patients without P/Q-type antibodies into mice was able to passively transfer LEMS symptoms to mice, indicating that seronegative LEMS is still antibody mediated (Nakao et al., 2002). Furthermore, some small-cell lung carcinoma patients without LEMS have been found to produce P/Q-type antibodies (Titulaer et al., 2009), and anti-VGCC antibody titers were not found to be predictive of long term disease outcome (Maddison et al., 2001). This suggests that the immune nature of LEMS is more complicated than simply the presence or absence of P/Q-type VGCC antibodies. There are multiple types of antibodies that target different parts of the P/Q-type VGCC protein (Parsons & Kwok, 2002). Furthermore, LEMS patients have been found to produce many types of antibodies other than anti-P/Q-type, and the titer and types of antibodies can vary greatly between patients. 25-40% of LEMS patients produce N- and/or L-type VGCC antibodies, but most of these patients also produced P/Q-type antibodies (Johnston et al., 1994; Martin-Moutot, De Haro, & Seagar, 2008; Motomura et al., 1997). Antibodies have also been found for both synaptotagmin-1 (Takamori et al., 1995) and M1-type presynaptic muscarinic acetylcholine receptors (Takamori, 2008) in LEMS patient serum.

1.4.2 LEMS neuromuscular physiology

Because LEMS is an antibody-mediated disease, and because many of the proteins targeted by LEMS are well-conserved between species, LEMS can be passively transferred to mice by repeatedly injecting them with serum from human LEMS patients (Fukunaga et al., 1983; Lang et al., 1984). The creation of these LEMS mice has allowed for a wide variety of investigations into the neuromuscular physiology of LEMS.

Early freeze fracture electron microscopy studies of biopsied muscle tissue from human LEMS patients showed a decrease in the number of presynaptic AZs and a disorganization of particles in remaining AZs (Fukunaga et al., 1982). Similar results were found by freeze fracture electron microscopy in presynaptic terminals of LEMS-model mouse NMJs (Fukunaga et al., 1983; Fukuoka et al., 1987). This disruption of the AZ structure is generally thought to be due to the antibody-mediated loss of P/Q-type VGCCs, and explains the muscle weakness seen in LEMS patients: the reduction in P/Q-type VGCCs leads to a reduced influx of calcium ions during an AP, which results in a reduction of neurotransmitter release and a subsequent reduction in muscle activation. This hypothesis is further supported by evidence that P/Q-type calcium current in LEMS mice is 30-40% less than in controls (Smith et al., 1995; Xu, Hewett, & Atchison, 1998). Furthermore, the lateral displacement of remaining P/Q-type calcium channels may cause a further reduction in transmitter release, as movement of the VGCCs away from the calcium-sensing protein will reduce their effectiveness.

Blocking the P/Q-type VGCCs in a healthy mouse NMJ will normally completely block neurotransmitter release, suggesting that under healthy conditions P/Q-type VGCCs are the only type of AZ close enough to the vesicles in the AZ to induce transmitter release. However, in LEMS mice, other VGCC types (primarily L-type) have been found to contribute to transmitter release (Flink & Atchison, 2002; Smith et al., 1995; Xu et al., 1998). This is generally thought to be a compensatory attempt by the NMJ to increase transmitter release by overexpressing VGCC types. Despite this compensation, LEMS mouse NMJs release 60-75% less neurotransmitter than healthy controls (Flink & Atchison, 2002; Fukunaga et al., 1983; Lang et al., 1983; Tarr et al., 2014; Tarr et al., 2013b). Since L-type VCGGs do not contain the synaptic protein interaction (synprint) site that is necessary to associate with AZs, they are likely place outside of the AZ (Catterall, 1999; Mochida et al., 2003; Sheng, Westenbroek, & Catterall, 1998). Indeed, preliminary experiments on LEMS passive-transfer mice found that L-type channel contribution to transmitter release is blocked by the addition of low concentrations of DM-BAPTA buffer, suggesting that the L-type channels are not within close proximity to the calcium sensing proteins in the AZs (Flink, 2003).

1.5 Treatment of Lambert-Eaton Myasthenic Syndrome

In patients with paraneoplastic LEMS, the treatment of cancer is the main priority, and successful treatment of the cancer often also results in the treatment of LEMS. For idiopathic LEMS patients, there is no cure. However, the FDA has recently approved 3,4-Diaminopyridine for the treatment of LEMS under the brand name Firdapse. There are also several immunomodulatory therapies available.

1.5.1 Symptomatic treatment with 3,4-Diaminopyridine

3,4-Diaminopyridine (3,4-DAP) is currently the only FDA approved treatment option for LEMS. Although it was only recently approved, it has been used off-label under a compassionate care provision as a LEMS treatment for several decades. 3,4-DAP is a voltage-gated potassium channel blocker. By blocking potassium channels, it broadens the AP, which increases the probability that the remaining VGCCs in the AZ will open during a given AP. This then results in an increase in calcium ion flux during an AP, and a subsequent increase in transmitter release.

However, 3,4-DAP dosing is limited by side effects. It is well tolerated in general, usually only causing mild side effects such as a paresthesia and gastrointestinal symptoms (Keogh, Sedehizadeh, & Maddison, 2011; Titulaer et al., 2011a). However, at high doses (> 100 mg per day) it can cause seizures (Lindquist & Stangel, 2011; Sanders et al., 2018; Sanders et al., 2000). Thus, 3,4-DAP dosing is typically limited to 80 mg/day (Kesner et al., 2018). A standard dose of 3,4-DAP has been found to result in a serum concentration of approximately 1-1.5 μM (Haroldsen et al., 2015a; Haroldsen et al., 2015b; Ishida et al., 2015; Thakkar et al., 2017; Wirtz et al., 2009). *Ex vivo* experiments with these concentrations have been shown to approximately double neurotransmission from presynaptic NMJ terminals in LEMS mice. However, in mice with a 75% reduction in transmitter release compared to healthy controls, this only improves the transmitter release to 50% of healthy controls (Tarr et al., 2014). As a result, 3,4-DAP only provides a mild symptomatic improvement in LEMS patients, and normal physical activity is often not possible for LEMS patients even with 3,4-DAP treatment.

1.5.2 Immunotherapies and cholinesterase inhibitors

Although 3,4-DAP is the only FDA approved treatment for LEMS, it often only provides a moderate improvement in symptoms. Several other therapies are also used for the treatment of LEMS including cholinesterase inhibitors, immunosuppressants, intravenous immunoglobulin, and plasma exchange therapy.

Cholinesterase inhibitors are compounds which prevent the degradation of acetylcholine in the synaptic cleft. Pyridostigmine is a cholinesterase inhibitor that is commonly used for the treatment of myasthenia gravis, and is occasionally used for the treatment of LEMS. Clinical studies on pyridostigmine in LEMS have found that pyridostigmine by itself is not effective, but in combination with 3,4-DAP it may have an improvement in symptoms over 3,4-DAP alone (Tim, Massey, & Sanders, 2000; Wirtz et al., 2009).

Other than drugs which target the behavior of the NMJ, such as 3,4-DAP and pyridostigmine, there are also several treatments for LEMS which target the immune system. Since 3,4-DAP alone is often not able to completely alleviate symptoms, immunotherapy is often used (often in addition to 3,4-DAP) in a large portion (up to 70%) of patients (Maddison et al., 2001; Titulaer et al., 2011a). If treatment with 3,4-DAP is not sufficient to alleviate chronic weakness, an immunosuppressive combination of prednisolone and azathioprine is often used as next line of treatment in addition to 3,4-DAP (Maddison et al., 2001; Newsom-Davis, 1998). However, treatment with prednisolone and azathioprine was found to only result in a mild improvement in symptoms, and high doses of prednisolone were still required 3 years after beginning treatment (Maddison, 2012; Maddison et al., 2001). There has been some evidence that Rituximab, which destroys B lymphocytes, may cause a moderate improvement in symptoms of LEMS patients (Boutin et al., 2013; Maddison et al., 2011; Pellkofer, Voltz, & Kuempfel, 2009). However, long term use of immunosuppressants carries an increased risk of infection, and can also result in severe side effects. Side effects for prednisolone include weight gain, diabetes, depression, psychosis, glaucoma, and gastrointestinal hemorrhaging. Side effects for azathioprine include flu-like symptoms, pancreatitis, and hepatitis (Skeie et al., 2010). Furthermore, there is a theoretical concern in patients with paraneoplastic LEMS that immunosuppression drugs may reduce the ability of the immune system to suppresses the growth of the tumor (Kesner et al., 2018; Maddison et al., 1999; Titulaer & Verschuuren, 2008).

For the treatment of LEMS with a rapid onset of symptoms, intravenous immunoglobulin or plasmapheresis are sometimes used in combination with other treatments. Plasmapheresis removes the plasma, which contains the antibodies, from the blood. Plasmapheresis has been shown to create a rapid improvement in LEMS symptoms, but this improvement only lasts for 2 to 4 weeks (Newsom-Davis, 2003; Newsom-Davis & Murray, 1984). Because of this relatively short period of benefit, plasmapheresis is not commonly prescribed, especially in the United States.

1.5.3 Potential for treatment with calcium channel agonists

3,4-DAP indirectly increases calcium ion flux into the presynaptic terminal by broadening the AP. Recently, drugs have been developed which act directly on VGCCs to increase calcium flux during and AP. The drug (*R*)-roscovitine was an early example of a drug with such an effect, and was found to prolong the mean open time of N- and P/Q-type VGCCs (DeStefino et al., 2010). However, (*R*)-roscovitine also inhibits cyclin-dependent kinases, making it unattractive for clinical use due to the lack of drug target specificity. More recently, several analogs have been made based on the chemical structure of (*R*)-roscovitine which retain the effect on VGCCs but no longer inhibit cyclin-dependent kinases at physiological concentrations of ATP (Wu et al., 2018a).

One such drug is GV-58. GV-58 is a direct VGCC positive allosteric gating modifier which prolongs the mean opening time of N- and P/Q-type VGCCs, and does not have any measurable effects on cyclin-dependent kinases. *Ex vivo* experiments with the maximally effective dose of GV-58 have shown that it has a similar effect on transmitter release to clinically relevant concentrations of 3,4-DAP, approximately doubling the transmitter release in LEMS mice (Tarr et al., 2013b). However, when combined with 3,4-DAP it has been shown to have a super-additive effect, where the combination of the two drugs has a greater effect than the sum of the effects of each drug. This super-additive effect occurs because 3,4-DAP increases the likelihood that VGCCs open during a given AP, and the GV-58 holds those open channels open for longer. The combination of these two drugs has been shown in *ex vivo* experiments in LEMS model mice to completely restore transmitter release to the levels of healthy control mice (Tarr et al., 2014). As a result, GV-58 and other calcium channel agonists are a promising potential treatment for LEMS, especially in combination with 3,4-DAP.

1.6 Voltage imaging

The action potential in neurons is typically recorded through the use of microelectrodes or patch-clamp electrophysiology. Although this technology is very sensitive and has high temporal resolution, it is limited by the ability to use these electrodes on small cellular compartments. With a few notable exceptions (such as the squid giant axon), most axons and dendrites are too small to probe with an electrode (Peterka, Takahashi, & Yuste, 2011). As a result, most recordings of the AP are from the soma of neurons. However, due to the geometry as well as the number, type, and distribution of ion channels throughout the cell, the AP can vary greatly between different parts of the neuron (Rowan et al., 2016). Voltage imaging is a developing technology that provides a means to potentially overcome the pitfalls of traditional electrophysiology. In voltage imaging, a voltage sensitive indicator is placed into the membrane of the cell. The fluorescence response of these indicators changes as the voltage across the membrane changes. This allows the recording of the voltage with a camera that can detect these changes in fluorescence.

Voltage indicators generally fall into two different categories: genetically encoded indicators or voltage sensitive dyes (Kulkarni & Miller, 2017). Voltage sensitive dyes were first developed in the 1970s, but early dyes were limited by many issues such as slow response to voltage changes and low sensitivity. Since then, many advances have been made. Recent work has employed photoinduced electron transfer as the voltage sensitive mechanism. These recent photoinduced electron transfer-based dyes are both fast and sensitive enough to monitor subtle changes in membrane potential dynamics (Huang, Walker, & Miller, 2015; Miller, 2016). Genetically encoded voltage indicators were first developed in 1997. They allow for a more targeted approach of specific neuronal subtypes, but have several limitations such as the targeting of the genetic expression (Kulkarni & Miller, 2017).

Voltage imaging essentially has two different uses: 1) simultaneously measuring voltage from multiple neurons, and 2) measuring voltage from small regions of single neurons. Briefly, the first use of simultaneously recording voltages from multiple neurons would allow researchers to understand the communication between neurons in neural circuits with as many neurons as can be imaged. This has been performed *in vitro* for several years now, but technological advances in both the voltage indicators as well as camera technology has made *in vivo* recordings available only recently. When combined with optogenetics, voltage imaging allows for "all optical electrophysiology", which will certainly make many important discoveries in neuroscience in the coming years (Hochbaum et al., 2014).

The second use of voltage imaging is to record the action potential in smaller regions of the neuron, such as the axons or dendrites (Ford & Davis, 2014; Ginebaugh et al., 2020; Hoppa et al., 2014; Popovic et al., 2011; Rowan et al., 2016). Using voltage imaging to record the action potential in smaller regions of the neuron allows us to understand the computation performed by the axons and dendrites and the contributions these regions play to the behavior of the neuron as a whole. When measuring the voltage in multiple neurons simultaneously, it is possible to measure the voltage in the smaller parts of the neurons. However, the large recording window and the camera speed required to record from many neurons at once often makes these smaller sections of the neurons only a few pixels wide, limiting the accuracy of such recordings. Currently, most of the multi-neuron voltage imaging experiments focus mainly on the AP waveforms in the somas. In the future, as camera and voltage indicator technology improve, it may be possible to accurately resolve all sections of each neuron simultaneously.

1.7 Computational modeling of the active zone

1.7.1 The advantages of computational modeling

The small scale of the AZ makes it very difficult to investigate experimentally. This is largely due to the fact that intermembranous particles are spaced as little as 14 nm apart (Fukuoka et al., 1987), well below the Abbe diffraction limit of ~200 nm (Abbe, 1873). Electron microscopy techniques such as freeze-fracture electron microscopy (Fukunaga et al., 1983; Fukuoka et al., 1987; Heuser et al., 1974; Pawson et al., 1998a; Pawson, Grinnell, & Wolowske, 1998b; Peper et al., 1974; Pfenninger et al., 1972) and electron tomography (Nagwaney et al., 2009) can investigate the structure of the AZ, but are limited by their inability to investigate live cells and difficulty in determining the identity of particles found by this form of imaging. Electrophysiology experiments using BAPTA and EGTA buffers can also provide some information about the distance between particles within the AZ, but can only give a general estimate of how close different particle types are spaced and cannot estimate the number of particles. Super-resolution microscopy techniques have also provided information about the active zone structure (Nishimune et al., 2016). However, super-resolution techniques that could resolve the location of particles in the AZ currently have several limitations such as the development of appropriate probes for the particles in the AZ structure (Collot et al., 2019).

Computational modeling provides a means to investigate the AZ on a scale below the limits of microscopy. Computational modeling can also be used to understand complex molecular interactions and predict their effects on cellular physiology, and to ask questions that may never be possible experimentally (e.g., what electrophysiological changes occur by rearranging a frog AZ to the structure of a mouse AZ without altering any biophysical parameters? (Laghaei et al., 2018)).

1.7.2 Selecting a method for computational modeling

A variety of methods and software exist for the computational simulations of biological systems. One important factor in selecting the proper tool is the scale of the system in question. For simulations of multiple neurons, programs such as NEURON (Carnevale & Hines, 2005; Hines & Carnevale, 1997, 2001) or algorithms such as an integrate-and-fire network can be used. NEURON is also useful for modeling of neurons as a whole. However, NERUON is limited in its scale, and cannot model important sub-cellular physiology such as complex sub-cellular geometries or the behavior of ions on a small scale.

For the modeling of sub-cellular physiology, a variety of programs exist as well. Many of these programs, such as STEPS (Hepburn et al., 2012), use a voxel-based approach. In this approach, a sub-cellular region is divided into voxels, and the concentration of particles is estimated in each voxel at each time step.

One of the most important factors determining the rate of transmitter release is the behavior and dynamics of calcium ions as they enter into and diffuse throughout the AZ. At the small scale of the AZ, the 3D structure of the cell often becomes an important factor in determining the behavior of the system, and is essential to include for accurate modeling. The complex and irregular geometry of the AZ, in addition to the fact that the number of particles in a small section of the AZ may be very low, makes models which use voxel-based approaches inaccurate (Stefan et al., 2014). Thus, programs such as STEPS are able to model a region smaller than programs such as NERUON, but are still not able to model at the scale of the AZ. A way to avoid these issues is to use a particle-based spatial stochastic approach. In a particle-based model, each molecule is simulated and stochastically diffused through the cell. As a result, arbitrarily complex 3D cellular ultrastructures and low concentrations of particles can be accurately modeled in the simulation.

The software used in this research to model the AZ is called MCell. MCell uses Monte Carlo methods to create particle-based, stochastic, realistic reaction-diffusion simulations of subcellular systems with arbitrarily complex 3D geometry (Kerr et al., 2008; Stiles et al., 1996). Because it is particle based, the location of each ion diffusing throughout the AZ is simulated at each timestep, allowing for an accurate model of the calcium dynamics at the scale of the AZ.

2.0 The frog motor nerve terminal has very brief action potentials and three electrical regions predicted to differentially control transmitter release

The action potential (AP) waveform controls the opening of voltage-gated calcium channels and contributes to the driving force for calcium ion flux that triggers neurotransmission at presynaptic nerve terminals. Although the frog neuromuscular junction (NMJ) has long been a model synapse for the study of neurotransmission, its presynaptic AP waveform has never been directly studied, and thus the AP waveform shape and propagation through this long presynaptic nerve terminal are unknown. Using a fast voltage-sensitive dye, we have imaged the AP waveform from the presynaptic terminal of male and female frog NMJs and shown that the AP is very brief in duration and actively propagated along the entire length of the terminal. Furthermore, based on measured AP waveforms at different regions along the length of the nerve terminal, we show that the terminal is divided into three distinct electrical regions: A beginning region immediately after the last node of Ranvier where the AP is broadest, a middle region with a relatively consistent AP duration, and an end region near the tip of nerve terminal branches where the AP is briefer. We hypothesize that these measured changes in the AP waveform along the length of the motor nerve terminal may explain the proximal-distal gradient in transmitter release previously reported at the frog NMJ.

2.1 Introduction

Action potential (AP) invasion of the presynaptic nerve terminal activates voltage-gated calcium channels (VGCCs) positioned within active zones (AZs; highly organized site of synaptic transmission that contain an ordered array of synaptic vesicles and VGCCs) of the motor nerve terminal (Cohen, Jones, & Angelides, 1991; Heuser & Reese, 1981; Pumplin, Reese, & Llinas, 1981; Robitaille, Adler, & Charlton, 1990), resulting in an influx of calcium that triggers the exocytosis of neurotransmitter (Dodge & Rahamimoff, 1967; Luo et al., 2015; Meriney & Dittrich, 2013). Although the frog neuromuscular junction (NMJ) has been a model synapse for the study of synaptic transmission, its AP has never been directly studied due to the small diameter of the nerve terminal making traditional electrophysiological recording difficult.

The size and shape of the AP waveform greatly impacts transmitter release by controlling both the activation of VGCCs and the driving force for calcium entry through VGCCs while they are open (Borst & Sakmann, 1999; Pattillo et al., 1999; Sabatini & Regehr, 1997). The AP has been recorded from isolated adult frog spinal neurons (Dambach & Erulkar, 1973; Erulkar & Soller, 1980; Ovsepian & Vesselkin, 2006). However, the shape of the AP waveform at the adult motor nerve terminal is likely different because recordings in other neurons have found large discrepancies between AP waveforms at the soma and axon (Hoppa et al., 2014; Popovic et al., 2011; Rowan et al., 2016). Furthermore, the AP waveform has been shown to vary along the axons of other types of neurons due to several factors including the geometry of the axon and distributions of different types of voltage-gated ion channels (Hoppa et al., 2014; Rowan et al., 2016).

It was originally hypothesized that the AP is actively propagated along the length of the frog motor nerve terminals by voltage-gated sodium channels distributed along the entire length of the terminal (Braun & Schmidt, 1966; Katz & Miledi, 1965b, 1968). However, the possibility that the AP may be passively propagated through these nerve terminal branches has also been proposed (Mallart, 1984; Robitaille & Tremblay, 1987). Furthermore, active propagation of the AP has been called into question by reports of proximal-distal gradients in neurotransmitter release magnitude along the length of frog motor nerve terminals (Bennett, Jones, & Lavidis, 1986a; Bennett, Jones, & Lavidis, 1986b; Bennett, Lavidis, & Lavidis-Armson, 1989; D'Alonzo & Grinnell, 1985; Mallart, 1984; Tremblay, Robitaille, & Grenon, 1984; Zefirov & Khalilov, 1985), and because these changes are not caused by differences in proximal-distal distribution of AZ structure (Pawson et al., 1998b).

Here, we use a fast voltage-sensitive dye (Huang et al., 2015) to record the presynaptic AP waveform at the frog NMJ and investigate the changes to this waveform as it propagates down the motor nerve terminal. We show (1) that the AP waveform is very brief in duration, (2) the presynaptic terminal of the frog NMJ has three distinct electrical regions, and (3) that the changes in the AP waveform as it propagates along the length of the terminal are not caused by changes in nerve terminal geometry. Using imaged AP waveforms and previously validated computer simulations, we predicted effects of our recorded AP waveforms on presynaptic calcium entry and transmitter release, and hypothesize that changes in the shape of the AP may be responsible for proximal-distal differences in neurotransmitter release that were previously reported.

2.2 Materials and Methods

2.2.1 Cutaneous pectoris nerve-muscle preparations

Experiments were performed on cutaneous pectoris nerve-muscle preparations from both male and female adult frogs (*Rana pipiens*). Frogs were anesthetized in a 0.1% tricaine solution, then decapitated and double-pithed in adherence to the procedure approved by the University of Pittsburgh Institutional Animal Care and Use Committee. Preparations were dissected bilaterally and bathed in normal frog Ringer's solution (NFR; 116 mM NaCl, 2 mM KCl, 5mM dextrose, 1 mM $MgCl_2$, 1.8 mM $CaCl_2$, pH 7.3-7.4, and 10 mM BES).

2.2.2 Voltage imaging

The BeRST 1 dye (Huang et al., 2015) was stored in 5 mM aliquots in DMSO at -80°C. On the day of use, 0.5 μL of BeRST 1 dye stock solution was diluted into 4.5 μl of DMSO initially, and then this mixture was diluted into 0.5 ml of NFR (for a final BeRST 1 concentration of 5 μM). This final loading solution also contained 10 μg/ml of Alexa Fluor 488-conjugated α-bungarotoxin (BTX) to counter stain postsynaptic receptors at the NMJ. To load nerve terminals with dye for the voltage-imaging procedure, the neuromuscular preparation was mounted over an elevated Sylgard platform in a 35 mm dish and incubated with the dye mixture described above for 90 minutes. The dye-loaded and BTX-stained preparation was then rinsed with NFR, mounted on the microscope stage, and the nerve was drawn into a suction electrode for supra-threshold stimulation. If the BTX conjugated to Alexa Fluor 488 did not completely block muscle contractions, 10 μM curare was added to the imaging saline to completely block postsynaptic acetylcholine receptors and prevent nerve-evoked muscle contractions.

For voltage imaging, tissue was mounted on an Olympus BX61 microscope equipped with a 60x water immersion objective. Nerve terminals were identified using the BTX staining, and this label was also used to bring the terminals into focus for voltage imaging. Superficial nerve terminals tended to load a higher concentration of BeRST 1 dye and produce noticeable less-noisy data than nerve terminals embedded deeper in the muscle. Thus, all terminals imaged were on the surface of the muscle. After locating a well-stained nerve terminal, we selected an imaging region of interest (ROI) of approximately 80x30 µm that contained a large portion of the nerve terminal branch (Figure 2A, B). All voltage imaging was performed in NFR at room temperature (20-25 °C).

Presynaptic nerve terminals in the frog cutaneous pectoris nerve-muscle preparations were stimulated at 0.2 Hz, and BeRST 1 dye fluorescence was recorded by an EMCCD camera (Pro-EM 512, Princeton Instruments). Image capture was coupled to illumination by a 640 nm laser (89 North laser diode illuminator) that only illuminated the tissue during the brief 100 µs image collection window. The entire AP waveform was sampled through a moving-bin acquisition scheme, where 100 bins were collected sequentially over the time course of an AP waveform that was elicited repeatedly at 0.2 Hz. A custom routine on a Teensy 3.5 USB development board (PJRC) created a delay between the stimulation of the nerve and the triggering of the camera and laser. This delay was increased by 20 µs after each stimulation in the collection time course. After 100 bins were collected, the delay was reset to 0. This process was repeated 5-20 times for each nerve terminal, creating 5-20 recordings of the full AP time course within the imaging ROI.

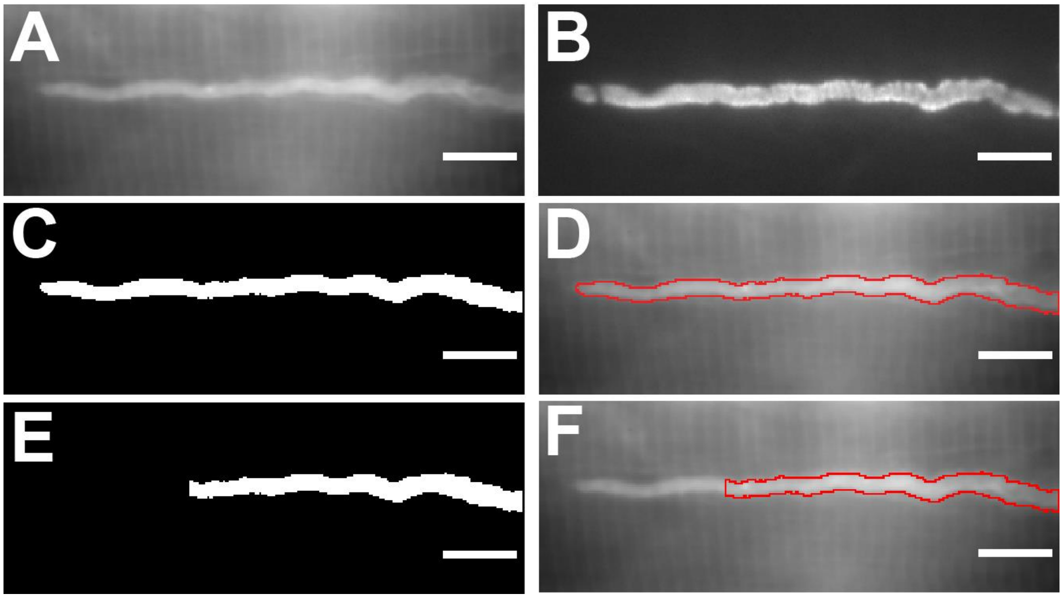

Figure 2 Imaging of the nerve terminal.

A, An image of a presynaptic motor nerve terminal stained with BeRST 1 dye. **B**, The same nerve terminal as in **A** stained with Alexa Fluor 488 α-BTX. **C**, An Otsu local thresholding algorithm applied to the terminal in **A** to create an image mask. **D**, An outline of the Otsu threshold image applied as an ROI for BeRST 1 dye imaging. **E**, The Otsu local thresholding image with the end of the terminal removed for analysis. **F**, The outline of the Otsu thresholding image with the end removed and applied as an ROI for the BeRST 1 dye imaging. All scale bars are 10 µm.

2.2.3 Image and data analysis

Images were analyzed in ImageJ and MATLAB (Mathworks) using custom written scripts. In ImageJ, the image stacks were stabilized for x-y drift using an "align slices in stack" ImageJ plugin (https://sites-google-com.pitt.idm.oclc.org/site/qingzongtseng/template-matching-ij-plugin; see Tseng et al., 2012; Tseng et al., 2011). Then, an Otsu local image threshold (Otsu, 1979) was applied to the average fluorescence z-projection of the stabilized BeRST 1 image stack to create an unbiased ROI selection containing the nerve terminal (Figure 2C, D). The average signal inside a subsection of this ROI (depending on the experiment) was used as the nerve signal. For control experiments, a region at least 20μm from the end and last node of Ranvier (Figure 2E, F) was used as the nerve signal (Figure 3A). The region outside of the Otsu selected ROI (Figure 2C, D) was averaged and used as the background signal (Figure 3*C*). Both the background and nerve signals were then low-pass filtered offline (f_{pass} = 4kHz, Figure 3B, D). We processed our signals both with and without filtering. We divided the unfiltered and filtered background fluorescence (Figure 3C, D) from the unfiltered and filtered nerve fluorescence (Figure 3A, B), respectively, to give us the unfiltered and filtered fluorescence signal (Figure 3E, F). To correct for z-axis drift (during which the live image could drift slightly in a non-linear fashion; see Figure 3E, F), we fit a cubic B-spline to the points in the fluorescence time course during which there was no AP stimulation (the first and last 15 points of the 100 total points in each series). We then divided this spline from each point in the fluorescence signal to give us a ΔF/F fluorescence signal that did not fluctuate as a result of drift of the nerve muscle preparation (Figure 3G, H).

The APs from the ΔF/F fluorescence signal were then averaged to create a single AP waveform (Figure 3I). To prevent discrepancies caused by including excessively noisy data, this analysis was performed both with (Figure 3B, D, F, H) and without (Figure 3A, C, E, G) the lowpass filter. We then calculated the R^2 value between the averaged unfiltered and filtered AP waveforms (Figure 3I). Since we are not using a linear model, R^2 is not an exact measure of fit between the filtered and unfiltered data, and is greatly affected by the ratio of the signal strength to the baseline noise. This provides a benefit in that not only will the R^2 value detect a poor fit between the filtered and unfiltered data, but will also provide a low value if the AP signal is not sufficiently detected in comparison to the noise (see Figure 3S). This is essential because normalizing any small signal on an otherwise flat waveform could appear as an AP. Thus, in this instance the R^2 is analogous to the range-normalized root-mean-square deviation (NRMSD). However, R^2 is less sensitive to outliers than the range-normalized (NRMSD) and provides easier-to-interpret results. Thus, we used the R^2 value only as a heuristic method to determine the quality of our recordings, and not for any statistical purposes.

For some recordings, image artifacts in the background (for example, a free-floating piece of connective tissue stained with BeRST 1 dye) resulted in noisy data due to the improper background use for calculating the nerve signal. If the R-squared was less than 0.95 for the full image (Figure 7) and 20 μm ROI data (Figure 8) or 0.85 for the 10-pixel diameter small-circle ROI data (Figure 9), a subsection of the background near the nerve terminal of approximately 15x30 μm was used rather the complete region outside the Otsu-selected ROI. If neither the full background selection or the smaller background sub-section resulted in an R-squared value higher than the values listed above, the recording was considered too noisy and was not included in the data analysis. If the recording was of high enough quality for analysis, the average AP was normalized to the baseline of the trace (the average value of the first 15 points), then cubic spline interpolation at an oversampled time resolution of 2 μs was fit to the filtered data, and the full width at half maximum (FWHM) of the AP waveform was calculated (Figure 3J).

We performed this procedure on the same nerve terminal both in the presence and absence of 1μM tetrodotoxin, and showed that these optically recorded AP signals were Na+ channel dependent based on their elimination in the presence of tetrodotoxin (TTX; Figure 3K-T).

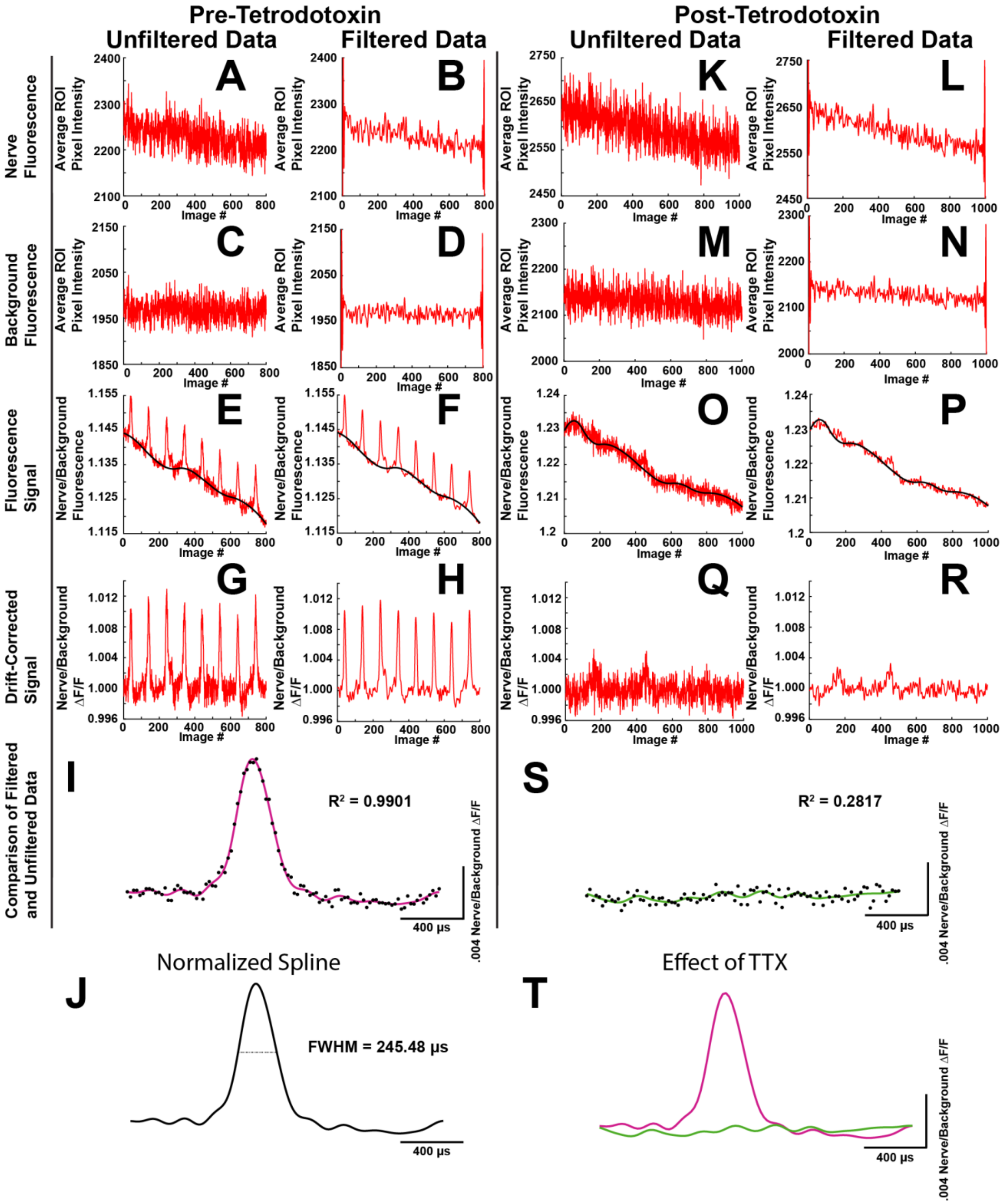

Figure 3 Analysis of the AP waveform and the impact of TTX.

Analysis of the AP waveform and the impact of TTX. **A, C,** The unfiltered fluorescence signals from the nerve and background selection of 800 sequential images collected from a motor nerve terminal ROI. **B, D,** The nerve and background signals from **A** and **C** low-pass filtered at 4 kHz, including the ringing artifact on the edges of the recording (truncated in the vertical axis). **E, F,** The unfiltered and filtered fluorescence signals, created by dividing the fluorescence values in **C** from **A**, or **D** from **B**, respectively, showing eight AP waveforms (red) with a cubic spline fit (black) thorough the unstimulated (baseline) points. **G, H,** The unfiltered and filtered fluorescence signal after correcting for the baseline by dividing the cubic spline from the fluorescence signal in **E** and **F**. **I,** The average of the 8 unfiltered AP waveforms from **G** (black dots) compared with the average of the eight filtered AP waveforms from **H** (magenta line). Comparing the two provides an R^2 value, which represents a measure of the fit weighted by the signal strength compared with the baseline noise. **J,** The average filtered AP waveform from **I,** fit with an interpolating cubic spline and then normalized to the baseline of the trace (based on the average value of the first 15 points of the average filtered AP waveform). **K–N,** The unfiltered and filtered fluorescence signals from the nerve and background selection of 1000 images of the same nerve terminal as in **A–D** but in the presence of 1 μM TTX. **O, P,** The unfiltered and filtered fluorescence signals, created by dividing the fluorescence values in **M** from **K** or **N** from **L**, respectively, showing the signal (red) with a cubic spline fit (black) thorough the unstimulated (baseline) points. **Q, R,** The unfiltered and filtered fluorescence signal after correcting for the baseline by dividing the cubic spline from the fluorescence signal in **O** and **P**. **S,** The average of the 10 stimulation cycles of the unfiltered signal from **Q** (black dots) compared with the average of the 10 stimulation cycles of the filtered signal filtered from **R** (green line). The low R2 value shows that the TTX eliminates the presence of the sodium-dependent AP waveform. **T,** A comparison of the average filtered fluorescent signal before (magenta) and after (green) the application of TTX.

Because the BeRST 1 dye stains all lipid membranes and connective tissues after bath application, the background was proportional to the total fluorescence, rather than being limited to standard camera shot noise. Thus, the background was divided, rather than subtracted, from the nerve signal to give us the fluorescence value used for analysis. Dividing the background also provided an additional advantage of eliminating the ringing artifacts caused by the lowpass filter overshooting the time domain. Furthermore, even when the ringing artifacts were removed, dividing the background still resulted in a less noisy signal (determined by higher R-squared values) than subtraction (Figure 4).

Based on previous research, we expected only a minor distortion caused by our use of 100 µs collection windows (Popovic et al., 2011). To confirm this prediction, we first created a theoretical AP waveform in MATLAB using a normalized gaussian with a standard deviation of 100 µs that consisted of 20000 points over 2000 time units, creating a waveform with a FWHM of 235 µs (10 points per µs across a 2000 µs window created a smooth curve). We sampled this waveform every 20 µs with a 100 µs recording window (averaging all points within the window), mimicking our imaging procedure, or every 20 µs with a 50 µs recording windows, and compared the results to the true waveform we created. We found that using a moving-bin sampling approach with a 50 µs or 100 µs recording window created only a small increase in the FWHM of the theoretical AP waveform (1.5% or 4.2%, respectively; Figure 5A). We then confirmed that our sampling scheme had little effect on our experimental data by recording from a single motor nerve terminal with our 20 µs moving-bin acquisition scheme using 20, 50, and 100 µs recording windows, and found little difference in the predicted waveforms (Figure 5B). However, the data collected with the 100 µs recording window was much less noisy (and had much better R-squared values) than the data recorded with the 50 µs and 20 µs recording windows for the same number of images (Figure 5B). Thus, we chose to use 100 µs recording windows and we chose not to correct for the small distortion in the AP waveform.

We made several attempts to calibrate the voltage by zeroing membrane potential using gramicidin (Hoppa et al., 2014; Maric et al., 1998; Meunier, 1984; Podleski & Changeux, 1969). However, we found that we were unable to block tissue movement caused by gramicidin even in the presence of a myosin chain blocker (BHC; Heredia et al., 2016). Thus, we chose to only report changes in the width of the voltage-imaging-measured AP waveforms, as is common in other papers with voltage imaging (Ford & Davis, 2014; Popovic et al., 2011; Rowan et al., 2016; Rowan, Tranquil, & Christie, 2014; Rowan & Christie, 2017). As such, the focus of this report is on the duration of presynaptic AP waveforms.

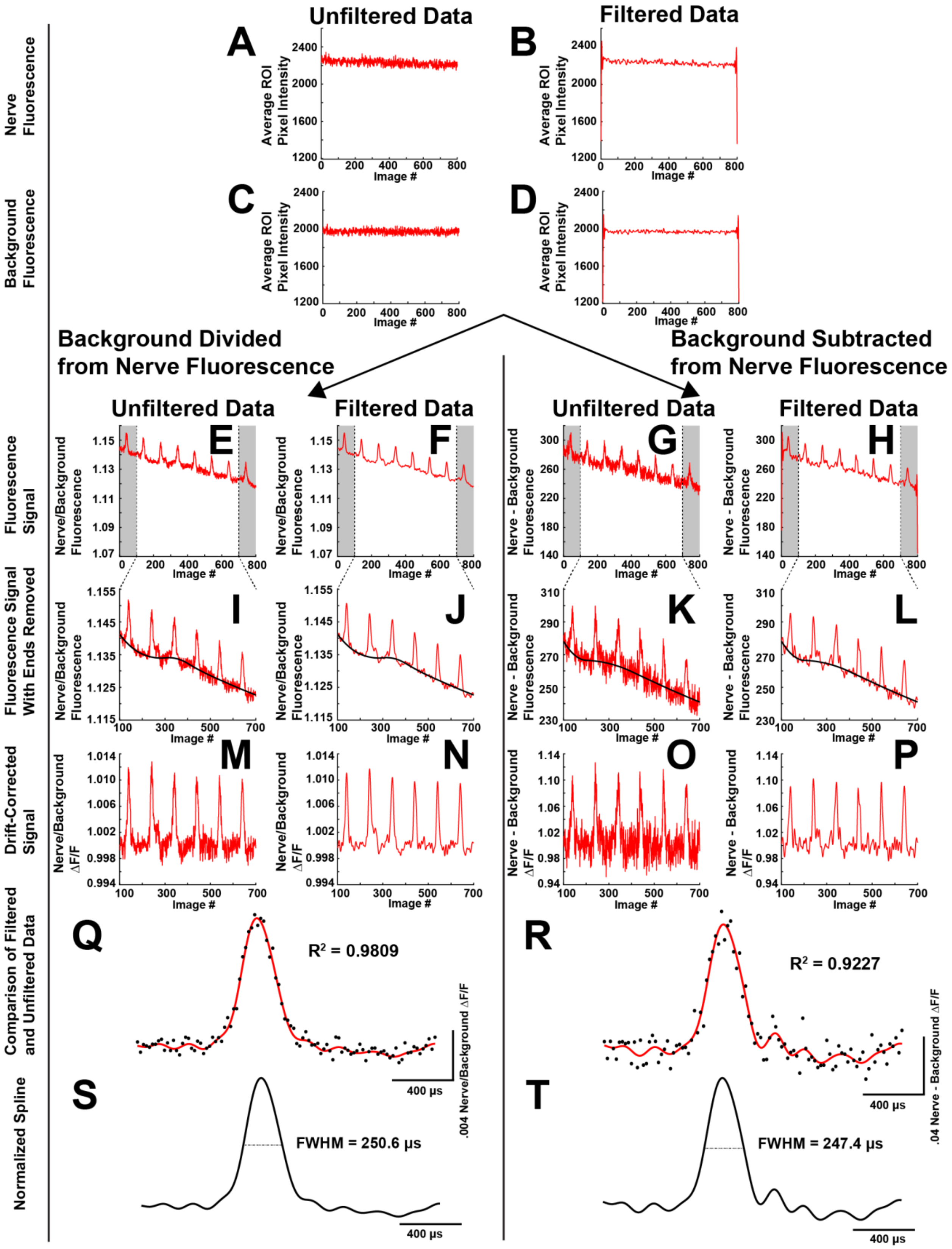
Unfiltered Data
Filtered Data
Nerve Fluorescence
Background Fluorescence
A
B
C
D
Average ROI Pixel Intensity
Image #
Background Divided from Nerve Fluorescence
Background Subtracted from Nerve Fluorescence
Unfiltered Data
Filtered Data
Unfiltered Data
Filtered Data
Fluorescence Signal
E
F
G
H
Nerve/Background Fluorescence
Nerve - Background Fluorescence
Fluorescence Signal With Ends Removed
I
J
K
L
Drift-Corrected Signal
M
N
O
P
Nerve/Background ΔF/F
Nerve - Background ΔF/F
Comparison of Filtered and Unfiltered Data
Q
R
R² = 0.9809
R² = 0.9227
400 µs
.004 Nerve/Background ΔF/F
.04 Nerve - Background ΔF/F
Normalized Spline
S
T
FWHM = 250.6 µs
FWHM = 247.4 µs
400 µs

Figure 4 Dividing the background signal from the nerve signal produces a better signal-to-noise waveform than subtracting the background signal.

A–D, The unfiltered and filtered data from the same 800 images of a nerve terminal shown in Figure 3A–D. Here, the y-axis is expanded to show the full ringing artifact in the filtered data. **E, F,** The unfiltered and filtered fluorescence signals created by dividing the background fluorescence from the nerve fluorescence. **G, H,** The unfiltered and filtered fluorescence signals created by subtracting the background fluorescence from the nerve fluorescence. Notice how subtraction does not remove the ringing artifact in the filtered data. **I–L,** The fluorescence signals (red lines) with the outer 100 data points on each side (**E–H,** gray bars) removed to exclude the ringing artifact remaining in the filtered fluorescence data created by subtraction (**H**), fit with a cubic spline through the unstimulated points (black line). **M–P,** The unfiltered and filtered fluorescence signal after correcting for the baseline by dividing the cubic spline from the fluorescence signals. **Q, R,** The average of 6 unfiltered AP waveforms (black dots) compared with the average of six filtered AP waveforms (red line). Notice how subtracting the background created a noisier signal and weaker signal-to-noise ratio, and therefore a lower R^2 value, even with the removal of the ringing artifact. **S, T,** The average filtered AP waveforms, fit with interpolating cubic splines and then normalized to the baseline of the traces (based on the average value of the first 15 points of the average filtered AP waveforms).

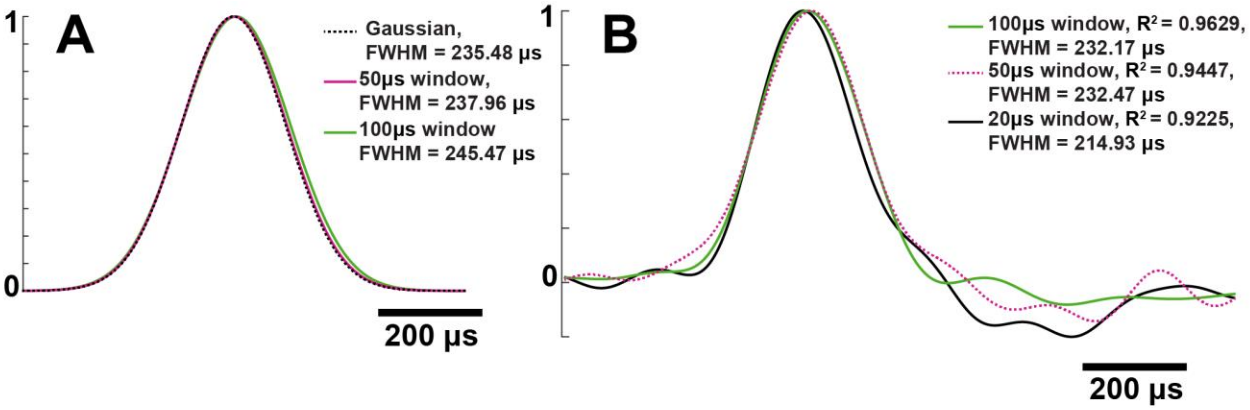

Figure 5 A 100µs recording window only causes a small distortion of the AP waveform, but improves the recording quality (as judged by the R^2 values).

A, A theoretical waveform created from a normalized Gaussian curve (black dots), compared with a waveform created by sampling the Gaussian with a 50 µs recording windows every 20 µs (magenta) and a waveform created by sampling the Gaussian with a 100 µs recording windows every 20 µs, mimicking our imaging procedure (green). This creates a theoretical 1.5 and 4.2% increase in the AP FWHM for the 50 and 100 µs recording windows, respectively. B, Normalized AP waveforms created from 1000 images each, with 20 µs (black), 50 µs (magenta), or 100 µs (green) moving bin recording windows. The AP FWHM from the 100 µs recording window is slightly larger than from the 20 µs recording window, but has a better R^2 value for the same number of images.

2.2.4 MCell simulations

MCell (www.mcell.org) was used to computationally study the impact of the experimentally recorded AP waveforms on AP-triggered calcium entry, and the impact of these waveforms on vesicle release from a modeled presynaptic nerve terminal AZ based on the frog NMJ. In brief, MCell is a particle-based, stochastic diffusion-reaction simulator that tracks the diffusion of particles through arbitrarily complex 3D structures (Kerr et al., 2008).

Here, we utilized two different models. First, to measure the impact of the AP waveforms on VGCCs, a model which consisted of a box containing 10000 VGCCs was created. This box model simply allowed for faster simulations and easier analysis of these VGCC characteristics because these simulations did not need to keep track of numerous other parameters. During a MCell run, an AP waveform triggered VGCCs to open stochastically according to an AP driven Markov-model ion channel gating scheme (Figure 6). When open, calcium ions entered the simulation environment from VGCCs at a rate determined by the instantaneous driving force. The total calcium inside the box and the probability of VGCCs opening were recorded during the AP waveform input.

Second, we used a previously-described frog computational model of a frog motor nerve terminal active zone to measure the impact of the experimental AP waveforms on transmitter release, as has been described previously (Dittrich et al., 2013; Homan et al., 2018; Laghaei et al., 2018; Ma et al., 2014). This single AZ model contained 26 synaptic vesicles and 26 VGCCs (driven by the same voltage-dependent gating scheme (see below and Figure 6) as in the box model) arranged in a double row at a 1:1 VGCC to synaptic vesicle stoichiometry (Luo et al., 2011). The bottom of each vesicle contained synaptotagmin-1 and second sensor binding sites (similar to synaptotagmin-7) responsible for triggering vesicle release (Ma et al., 2014). During an AP waveform, calcium diffused into the AZ model and bound to either calcium buffer (which was distributed evenly throughout the terminal) or to the calcium sensor sites (synaptotagmin-1 or second sensor sites) on the synaptic vesicles. When a sufficient amount of calcium was bound to the sensor sites (see Dittrich et al., 2013; Ma et al., 2014), the vesicle was considered to be "released". Since these simulations are stochastic, 4800 simulations were run for each waveform input.

The only differences between the previous reported frog AZ model and the AZ model used in this work were different AP waveform inputs to the model (see Figure 8F and Figure 13A), and new rate constants for the AP driven Markov chain ion channel gating scheme which drives the behavior of VGCCs in our model (Figure 6) (Dittrich et al., 2013). This gating scheme, like the scheme used in previous models, is a linear four-state model with three closed states and one open state. When in the open state, calcium ions enter the simulations environment from VGCCs with Poisson probability based on the parameter $\mathrm{k} = (-\gamma \mathrm{G}/2\mathrm{e}) * (\mathrm{V_m} - \mathrm{E}_{Ca})$, where V_m is the membrane voltage (determined by the AP waveform input), G = 2.4 is the channel conductance, E_{Ca} = +50mV is the equilibrium potential, e is the elementary charge, and γ = 0.9 is a scaling constant to account for the fact that the channel conductance was originally determined in 2 mM extracellular calcium. The rates for forward transitions between the states were determined by rate constants multiplied by the voltage-dependent parameter α, and reversal rates were determined by rate constants multiplied by the voltage-dependent parameter β, where $\alpha = 0.06\,\exp((\mathrm{V_m} + 24)\,/\,14.5)$ and $\beta = 1.7/(\exp\,((V_m + 34)/16.9) +\ 1)$. These rate constants were parametrized based on an experimentally measured whole-cell calcium current (see Dittrich et al., 2013; Pattillo et al., 2001). α and β were the same as used in previous models, but the forward and reversal rate constants were reparametrized to fit the predicted calcium current activated by our newly recorded AP waveform.

To modify our experimentally imaged APs for input into MCell (importantly, to set the AP waveform to a membrane voltage, and to put the waveform in a MCell-friendly format), we normalized the waveforms to a resting potential of -60 mV and a peak voltage of 30 mV. To remove fluctuations near the onset of the rising phase of the APs caused by noise in the experimental data, we standardized the beginning of the rising edge of each AP by replacing the first 10% of the rising edge with a line that had the same slope as the next 10% of the rising edge. To reduce fluctuations caused by noise after repolarization of the APs, we smoothed the afterhyperpolarization phase of each AP with a cubic polynomial (compare Figure 8F and Figure 13A).

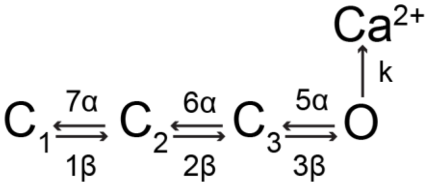

Figure 6 The four-state Markov chain VGCC gating scheme.

The gating scheme that determines the opening behavior of VGCCs in both the frog AZ MCell model and the 10,000 VGCC MCell box simulation.

2.2.5 NEURON simulations

A passive model of a frog motoneuron nerve terminal was simulated in NEURON, version 7.7 (https://www.neuron.yale.edu/neuron/; Hines & Carnevale, 1997, 2001). This model was a single tube with a length of 200 μm (approximately the average length of our recorded nerve terminals) and a diameter of 3.14 μm (the average diameter of our recorded nerve terminals). The axial resistance was set to 110 **Ω** cm (Miralles & Solsona, 1996), the leak conductance was set to 1e-5 S/cm^2 (Lindgren & Moore, 1989), the membrane capacitance was set to 1 μF/cm^2, and the temperature was set to 20°C. A recorded AP waveform was input into one end of the passive tube with a single electrode voltage clamp, and the shape and FWHM of the AP waveform as it passively propagated were recorded.

2.3 Results

2.3.1 Action potentials at the adult frog neuromuscular junction are brief in duration

To date, there have been several studies of the action potential waveforms at small nerve terminal boutons using voltage-sensitive dyes (Popovic et al., 2011; Rowan et al., 2016; Rowan et al., 2014). However, there have been no AP waveform measurements at the long, linear, adult motor nerve terminals present at the frog NMJ. Using a live-cell imaging approach, we measured the response of a fast voltage-sensitive dye (BeRST 1) to AP waveforms propagating along the frog motor nerve terminal (although the temporal resolution of BeRST 1 has not been recorded, dyes with a similar chemical structure respond to changes in membrane potential in approximately 25 ns; Beier et al., 2019). For all experiments, we measured the full width at half maximum amplitude (FWHM) to characterize effects on the duration of the AP.

We found the AP in the adult frog motor nerve terminal to be very brief (the average FWHM of all control recordings ($n = 32$) was 273.9 ± 10.7 μs; Figure 7). This is much briefer than might have been expected based on AP waveforms previously recorded from isolated adult frog spinal neurons (Dambach & Erulkar, 1973; Erulkar & Soller, 1980; Ovsepian & Vesselkin, 2006) and cultured embryonic frog motoneuron varicosities (Pattillo et al., 2001; Yazejian et al., 1997), where AP FWHM values range between 800-1200 μs. Interestingly, we also found a relatively large variability in the measured AP FWHM values across different NMJs (ranging from ~200 μs to ~400 μs FWHM). This is consistent with the large range in quantal content observed across individual NMJs (Laghaei et al., 2018), even when corrected for nerve terminal length (Grinnell & Herrera, 1980). Therefore, the AP duration could be one factor that contributes to this variability.

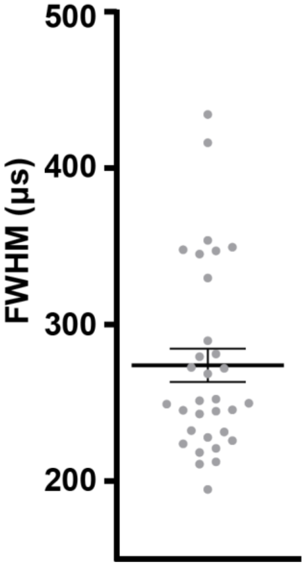

Figure 7 AP durations from all control images.

A scatter plot showing the range of AP durations (FWHM) from all control images (line = mean 6 SEM), where the nerve ROI selection was at least 20mm from both the end of the terminal and the last node of Ranvier. The AP waveform in the frog motor nerve terminal is very brief and can vary between terminals.

2.3.2 Differences in action potential duration along the length of motor nerve terminal branches reveal three distinct electrical regions.

Previous studies have shown that transmitter release varies along the length of the frog NMJ (Bennett et al., 1986a; Bennett et al., 1986b; Bennett et al., 1989; D'Alonzo & Grinnell, 1985; Mallart, 1984; Tremblay et al., 1984; Zefirov & Khalilov, 1985). There is some debate as to the average magnitude and distribution of these proximal-distal changes: some studies suggest a continuous proximal-distal decrease in transmitter release (Bennett et al., 1986a; Bennett et al., 1986b; Bennett et al., 1989), while others suggest that the transmitter release is greatest near the point at which the axon enters the presynaptic nerve terminal near the last node of Ranvier, reduces slightly but maintains a consistent level throughout the middle 60-90% of the nerve terminal, and then is reduced near the ends of the nerve terminal (D'Alonzo & Grinnell, 1985). Initially, this behavior was hypothesized to have been caused by proximal-distal changes in the structure of the AZs. However, freeze-fracture electron microscopy studies subsequently showed that there are no proximal-distal changes in AZ structure (Pawson et al., 1998b). Thus, we tested the hypothesis that these proximal-distal changes in transmitter release could be caused by changes in the AP waveform as it propagates through the nerve terminal.

To study the AP waveform along the length of frog motor nerve terminal branches, we performed our voltage-imaging procedure near the entry of the axon into the presynaptic nerve terminal just after the last node of Ranvier and again at the end of a nerve terminal branch (Figure 8A, B). In addition to the BeRST 1 images, we also documented the full length of NMJ nerve terminal branches we were studying using Alexa Fluor 488 α-bungarotoxin (BTX) images, which were combined using image stitching (Preibisch, Saalfeld, & Tomancak, 2009) to create images of the full length of the nerve terminal branches under study. We then measured the length of the recorded nerve terminal branches using a skeletonizing method (Figure 8) (Arganda-Carreras et al., 2010). Since the average nerve terminal branch length was approximately 200 μm (194.6 ± 7.8 μm), we analyzed the voltage-imaging data using multiple equally-distributed ROIs, each 20 μm in length, each corresponding to approximately 10% of the nerve terminal branch length. In particular, we focused on the first, second, and third 20μm ROIs starting from the last node of Ranvier as compared to the first, second, and third 20μm ROIs starting from the end of the nerve terminal (Figure 8A, B). This analysis revealed significant differences in the AP waveform duration near the last node of Ranvier and near the end of the nerve terminal, but no significant differences along the long middle portion of these long nerve terminal branches (Figure 8D-F).

These data do not suggest that the AP waveform duration decreases linearly with distance along the presynaptic nerve terminal branch, but only changes immediately after the axonal entry into the nerve terminal and near the tip of the nerve terminal branch. Based on these data, we propose that there are three distinct regions in the presynaptic nerve terminal of the frog NMJ where electrical signals are different: A beginning region immediately after the last node of Ranvier, a middle region consisting of 60-80% of the nerve terminal with a relatively consistent AP duration, and an end region near the tip of nerve terminal branches.

To further examine this hypothesis and to ensure that our results were not an artifact of our method of ROI selection for the data analysis, we reanalyzed the images by placing 5 ROIs, each consisting of 10-pixel diameter (2.667 μm) circles spaced 15 μm apart from their center along the nerve terminal just after each last node of Ranvier and near the end of the nerve terminal (Figure 9A, B). Because these data are created with a different method of analysis than the 20μm ROIs, multiple comparison corrections were performed separately for the 20 μm ROI and small-circle ROI data. Consistent with our analysis of 20 μm ROIs, these small-circle ROIs revealed significant differences near the last node of Ranvier where the axon enters the nerve terminal and near the end of the nerve terminal, but no significant differences along the long middle portion of the nerve terminal (Figure 9C, D).

To test if these changes in the AP waveform could be caused by passive propagation along the terminal, we created a passive model of the frog NMJ nerve terminal in NEURON and stimulated it with a recorded AP waveform from near the last node of Ranvier (Figure 8F, Figure 10A, and Figure 13A). Our model predicted that passive propagation would result in a broadening of the AP waveform as it decays (Figure 10). Furthermore, our model predicted that passive propagation would also cause broadening under a wide variety of different values for axon diameter, leak conductance, axial resistance, and membrane capacitance (data not shown).

These data confirm the existence of three distinct electrical regions within the presynaptic nerve terminal. Furthermore, the lack of broadening due to decay in the AP waveform as it propagates approximately 200 μm from near the last node of Ranvier to near the end of the nerve terminal suggests that the AP is actively propagated throughout the presynaptic motor nerve terminal in frogs (consistent with predictions from early studies; Braun & Schmidt, 1966; Katz & Miledi, 1965b, 1968).

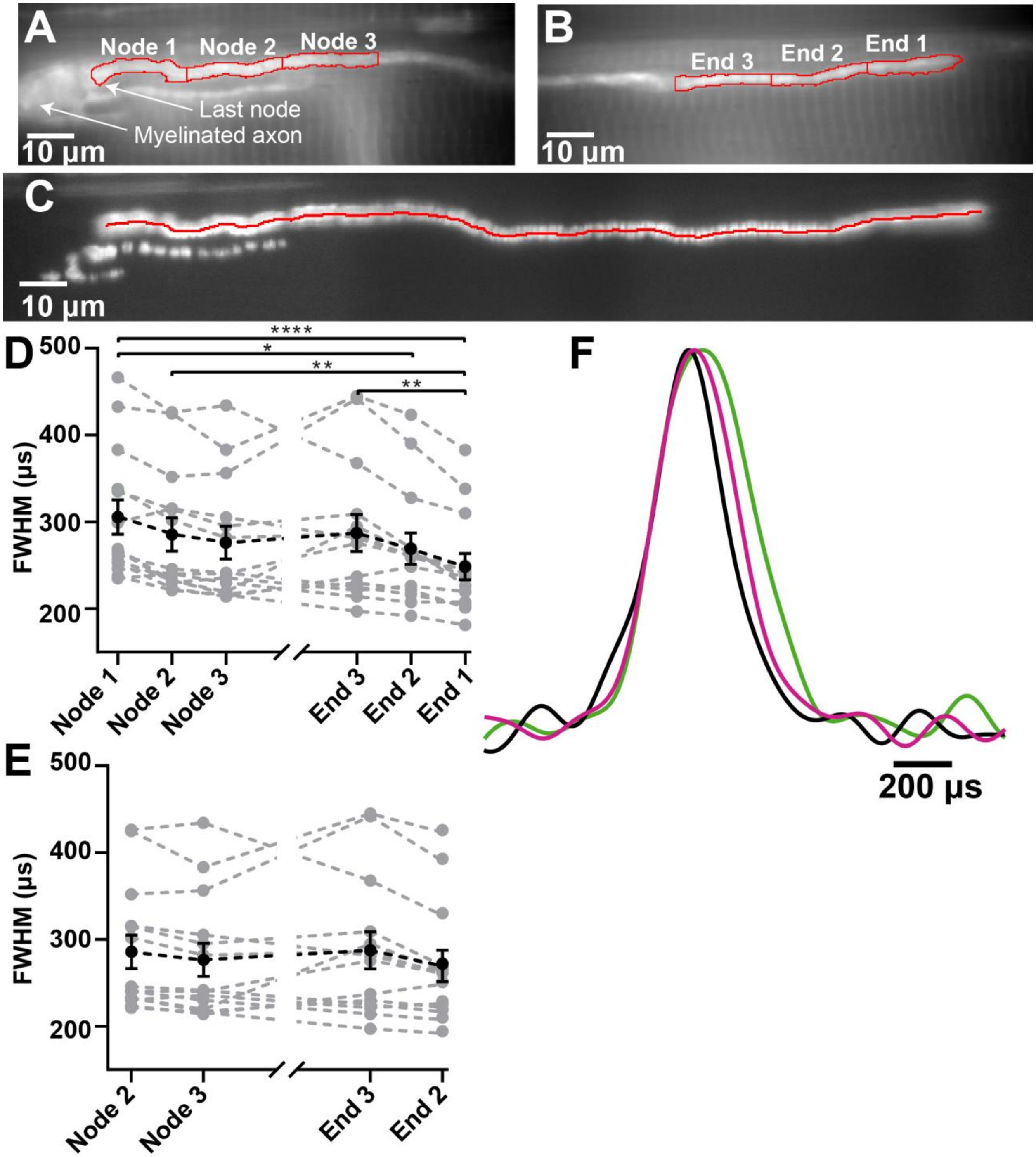

Figure 8 There are three distinct electrical regions along the frog motoneuron terminal.

A, A BeRST 1 dye image of nerve terminal near the last node of Ranvier. The myelinated axon and the last node of Ranvier are labeled in this image, along with the first, second, and third 20-µm-long ROIs identified by red outlines (labeled Node 1, Node 2, Node 3) starting from the last node of Ranvier and moving into a long nerve terminal branch. **B,** A BeRST 1 dye image of nerve terminal near the end of a long nerve terminal branch with the first, second, and third 20 µm long ROIs identified by red outlines (labeled End 1, End 2, and End 3), starting from the end of the nerve terminal. **C,** A BTX-labeled image of the full length of the long nerve terminal branch shown in **A** and **B**, overlaid with the skeletonized version of this nerve terminal branch (red). **D,** Plot of imaged AP FWHM data derived from 14 long motor nerve terminal branches (gray symbols, one set of which was taken from **A** and **B**) for each of 6 ROIs; 3 near the last node of Ranvier and 3 near the end of the nerve terminal branch (as shown in **A** and **B**). The mean data (±SEM) are shown using black symbols. Statistical significance between ROIs along the terminal is determined by Friedman test with Dunn's multiple post hoc comparisons test. $^{*}p < 0.05$, $^{**}p < 0.01$, $^{****}p < 0.0001$. **E,** Plot of FWHM data from the four ROIs in the middle region of long nerve terminal branches (gray symbols). Summary data are shown in black symbols. Within these middle regions (Node 2–End 2), there is no significant difference between any of these ROIs. $p = 0.0633$, Friedman test. **F,** AP waveforms from Node 1 (green), End 3 (magenta), and End 1 (black) taken from a representative motor nerve terminal branch.

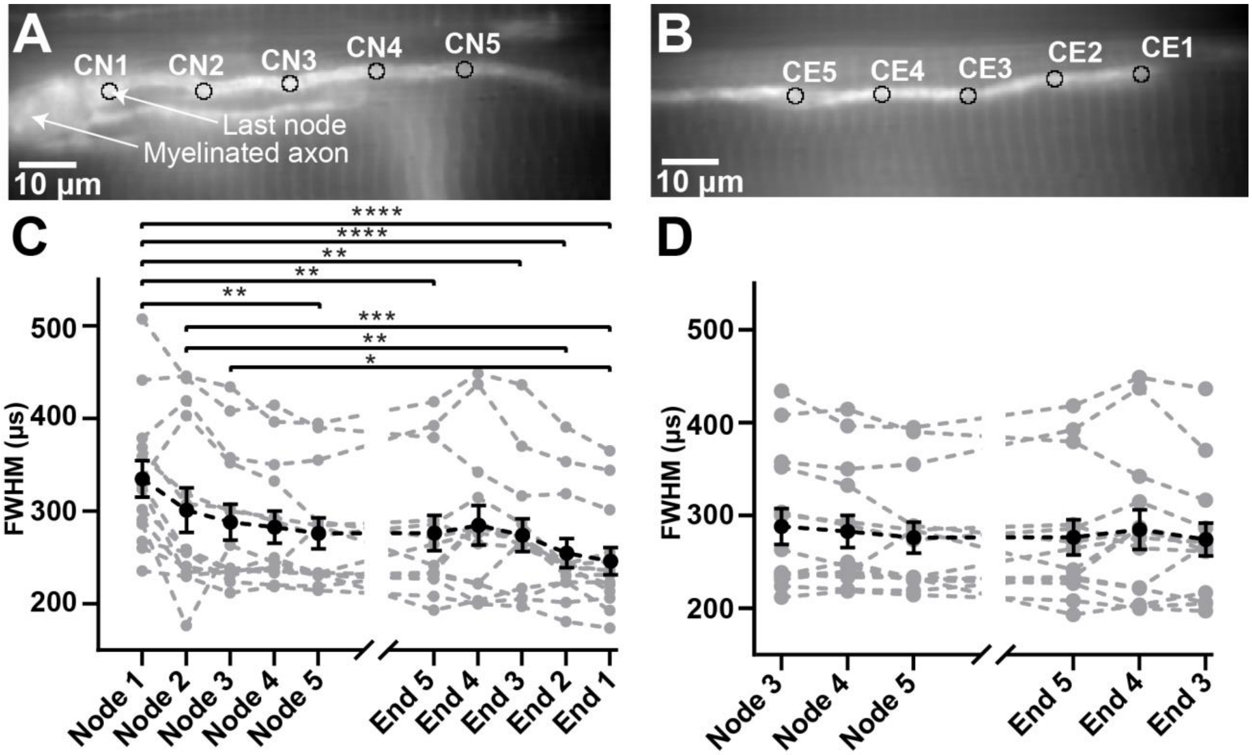

Figure 9 The use of small-circle ROIs for image analysis confirms the presence of three distinct electrical regions within motor nerve terminal branches.

A, A BeRST 1 dye image of a representative nerve terminal branch near the last node of Ranvier. The region of the motor nerve terminal near the last node of Ranvier is sampled with five circle ROIs placed 15μm apart, labeled Circle Node 1 (CN1) through CN5. Each circle is 10 pixels (2.667 μm) in diameter. **B,** A BeRST 1 dye image of a representative nerve terminal branch near the end of the nerve terminal with five circle ROIs place 15 μm apart, labeled Circle End 1 (CE1) through CE5. **C,** Plot of imaged AP FWHM data derived from 14 long motor nerve terminal branches (gray symbols, one of which was taken from **A** and **B**) for each of the 10 ROIs identified in **A** and **B**. The mean data (±SEM) are shown using black symbols. Statistical significance between ROIs along the terminal is determined by Friedman test with Dunn's multiple post hoc comparisons test. $*p < 0.05$, $**p < 0.01$, $***p < 0.001$, $****p < 0.0001$. **D,** Plot of data from six ROIs in the middle region of long nerve terminal branches (gray symbols), with summary data (black symbols). Within this middle region (CN3– CE3), there is no significant difference between any of these ROIs. $p = 0.2161$, Friedman test.

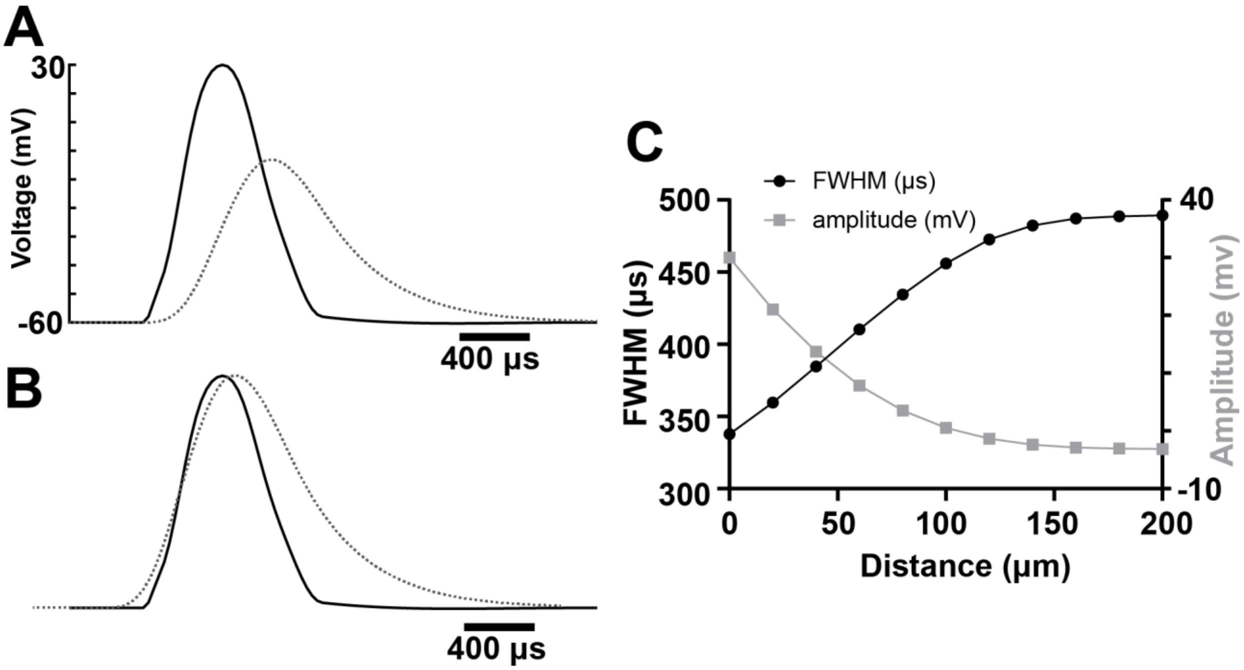

Figure 10 NEURON simulation predictions for changes to the AP waveform caused by passive propagation over a 200 µm long nerve terminal.

A, Waveform input based on recorded AP waveforms from near the last node of Ranvier (black), and the predicted change to the AP waveform caused by passive decay to the end of the long nerve terminal branch (gray dotted line). **B,** The two waveforms from A normalized and aligned to the half-maximum of their rising edge, showing a predicted 44% increase in the FWHM between the AP near the last node of Ranvier and near the end of the terminal. **C,** The predicted FWHM (black) and amplitude (gray) of the AP waveform (measured every 20 µm) as it passively propagates along a 200 µm long nerve terminal.

2.3.3 The propagation speed of the AP waveform does not change along the length of the terminal

The propagation speed of the AP waveform along the length of the presynaptic motor nerve terminal of the frog NMJ has previously been experimentally estimated using extracellular recording techniques (Braun & Schmidt, 1966; Katz & Miledi, 1965b; Nikol'kii et al., 2002).

Furthermore, it had been suggested that the AP propagates slower near the last node of Ranvier and faster near the end of the nerve terminal (Braun & Schmidt, 1966; Nikol'kii et al., 2002). However, these prior studies relied on reconstructing the electrical activity within the nerve terminal based on recordings from extracellular currents, which are prone to significant variation due to variances in the extracellular tissue surrounding the nerve terminal and the placement of the electrode with respect to the nerve terminal. To directly examine the propagation speed of the AP in the adult frog NMJ nerve terminal, we compared the time between the half maximums of the rising edge of the AP waveforms from the small-circle-ROI voltage imaging data from near the last node of Ranvier and at the tip of the nerve terminal branch (e.g., CN1 and CE1 from Figure 9). By combining these data with the distances recorded from the stitched BTX images of the total nerve terminal branch length, we were able to measure the propagation speed of APs (0.6586 ± 0.0700 m/s). We also compared the propagation speed between the first (CN1) and last (CN5) ROIs near the last node of Ranvier (0.6006 ± 0.0588 m/s) and the first (CE5) and last (CE1) ROIs near the end of the nerve terminal (0.6584 ± 0.0828 m/s) to determine if the AP was propagating at different speeds near the last node of Ranvier vs. the end of the nerve terminal branches. There was no significant difference in AP propagation speed found between any of these three measurements, and the average between the three groups was 0.6392 ± 0.0403 m/s. We repeated this analysis using our larger 20μm ROI data by assuming that the AP represents the center of the ROI (so the distance between the first and last ROIs from each image was assumed to be only 40 μm) and found almost identical results (Figure 11). These results are consistent with the average speeds determined by extracellular recordings (Braun & Schmidt, 1966; Katz & Miledi, 1965b; Nikol'kii et al., 2002), but do not agree with the extracellular data that had suggested that the AP propagates slower near the end of the motor nerve terminal (Braun & Schmidt, 1966; Nikol'kii et al., 2002). Furthermore, this propagation speed is similar to the AP propagation speed determined in *Drosophila* NMJs when imaging a genetically encoded voltage sensor (Ford & Davis, 2014), although the AP of the *Drosophila* NMJ is approximately 6 times broader than the AP waveforms recorded at the frog NMJ.

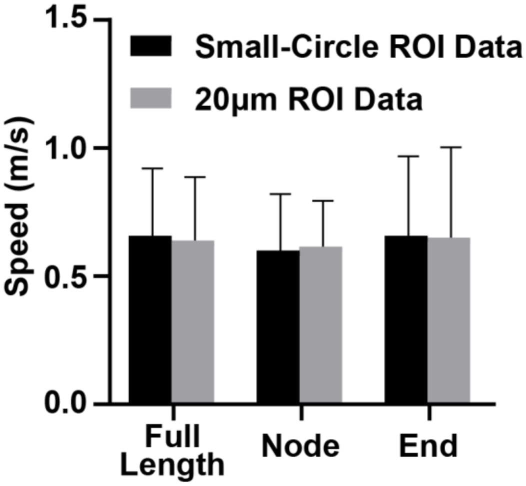

Figure 11 Comparison of the AP propagation speeds near the last node of Ranvier, near the end of the terminal, and along the length of the entire terminal using both 20mm ROI and small-circle ROI data.

There is no significant difference in AP propagation speed in different regions of the terminal (*n* = 14; *p* = 0.7515 for 20 µm ROIs, *p* = 0.3189 for small-circle ROIs; Friedman test), and there is no significant difference between the 20 µm and small-circle ROI measurements in any region (full length: *p* = 0.5416, node: *p* = 0.2166, end: *p* = 0.5830; Wilcoxon matched-pairs signed rank test). Data shown as mean + S.D.

2.3.4 Motor nerve terminal width does not correlate with AP duration or propagation speed within the motor nerve terminal

Although nerve terminal diameter would be predicted to play a role in determining the shape and propagation speed of the AP waveform, research in other neurons types has reported that the diameter of the presynaptic nerve terminal has a negligible effect on the shape and propagation of AP waveforms, as compared to the effect of ion channel expression (Rowan et al., 2016). To investigate the impact of nerve terminal geometry on the AP waveform and to test if changes in nerve terminal geometry could be responsible for the observed changes in the frog NMJ AP waveform, we measured the area of the imaged nerve terminal region contained in all three of the 20μm ROIs near the last node of Ranvier, as well as near the end of the nerve terminal. By dividing this area by the length between the two first and last ROIs, we calculated the average width of the axon near the last node of Ranvier and at the end of the nerve terminal. We then calculated the correlation between axon width, the 20μm ROI AP FWHM, and the 20μm ROI propagation speeds in a combined dataset of the values near the end of the terminal and near the last node of Ranvier (where the AP FWHMs of the three 20μm ROIs near the last node of Ranvier are averaged together for each terminal, and the same is done for the three 20 μm ROIs near the end of each terminal). We note that our imaging procedure was limited to measuring the width of the nerve terminal, so our analysis of the terminal geometry was based on a two-dimensional image assuming a symmetrical three-dimensional geometry. Using this approach, we found no correlation between terminal width and either AP FWHM or AP propagation speed but did find a correlation between AP FWHM and AP propagation speed (Figure 12A, C, E). We then repeated this analysis using propagation speed and AP FWHM values from our small-circle ROIs and found similar results (Figure 12B, D, F).

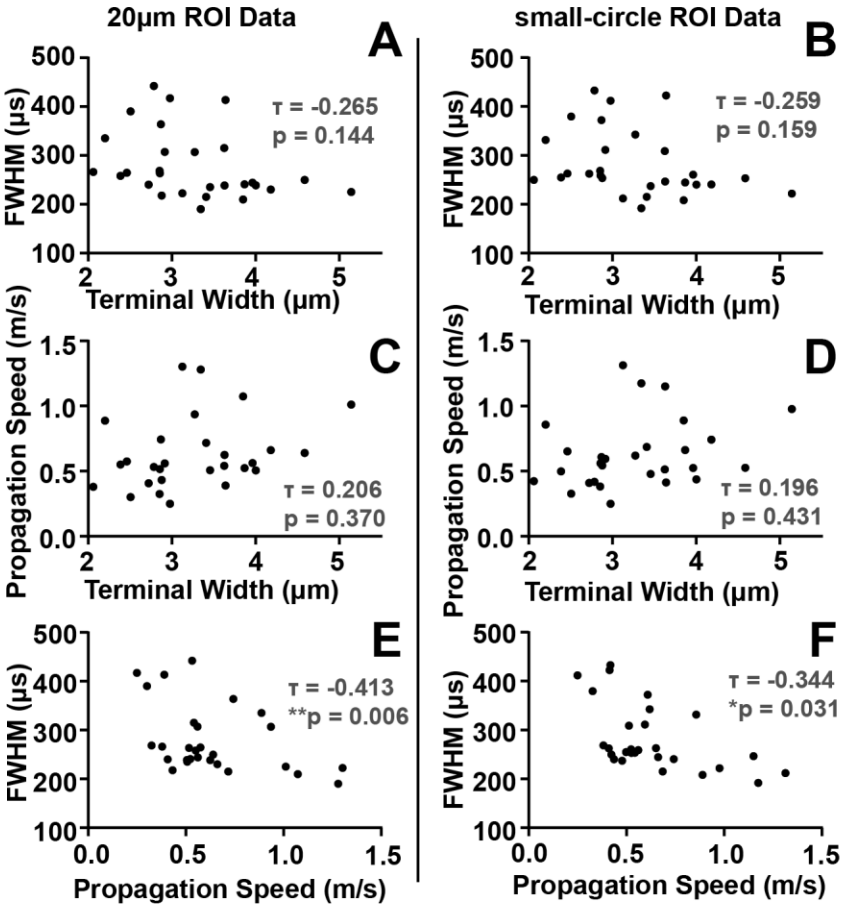

Figure 12 Measured motor nerve terminal width does not correlate with either AP duration (FWHM) or propagation speed, but propagation speed correlates with AP FWHM.

Combined data from near the end of the terminal and near the last node of Ranvier (*n* = 28), using both the 20 µm ROIs (left) and small circle ROIs (right), showing that measured motor nerve terminal width does not correlate with either AP duration (FWHM) or propagation speed, but propagation speed correlates with AP FWHM. **A, B,** Lack of correlation between the measured motor nerve terminal widths and AP durations (FWHM). **C, D,** Lack of correlation between the measured motor nerve terminal widths and the propagation speeds of the APs. **E, F,** Significant correlation between the AP duration (FWHM) and the AP propagation speed. All correlations are calculated with Kendall's τ coefficient, and *p* values were adjusted using Bonferroni's correction.

2.4 Discussion

The shape of the AP waveform at the motor nerve terminal impacts the behavior of presynaptic VGCCs, and thus is an important modulator of neurotransmitter release at the presynaptic nerve terminal. Although the adult frog NMJ has long been a model synapse for the study of synaptic transmission, its AP waveform has never been directly recorded. The lack of information regarding this AP waveform has hindered the ability to investigate the voltage-driven control of synaptic transmission, and also impacts computational simulations which depend on AP waveform-driven ion channel gating and ion flux (Dittrich et al., 2013; Homan et al., 2018; Laghaei et al., 2018; Ma et al., 2014). Furthermore, there has been debate as to whether APs within the long linear presynaptic terminals of the adult frog NMJ are actively or passively propagated. Therefore, to examine the duration and propagation of the presynaptic AP at the frog NMJ, we used the voltage-sensitive dye (BeRST 1) and showed that the AP waveform is extremely brief and is actively propagated throughout the nerve terminal.

For the data reported here, we selected nerve terminals for our imaging procedure that contained long (> 120 μm), linear nerve terminal branches. Thus, it is possible that short nerve terminals or terminals with significant branching may display different changes in their AP waveform duration along the length of these smaller branched segments.

2.4.1 Very brief AP waveforms may aid in maintaining strength and reliability at the NMJ

Voltage imaging of the presynaptic terminal of the frog NMJ revealed that the average AP waveform had a FWHM of only 273.9 ± 10.7 μs. This is much briefer than expected based on electrophysiological recordings from both adult frog motoneuron cell bodies in the spinal cord

(Dambach & Erulkar, 1973; Erulkar & Soller, 1980; Ovsepian & Vesselkin, 2006), and cultured frog embryonic motoneuron synaptic varicosities onto muscle cells (Pattillo et al., 2001; Yazejian et al., 1997). This leads us to wonder what advantages for adult NMJ function might be provided by a very narrow AP at these motor nerve terminals?

This question has been addressed in detail within the central nervous system at the Calyx of Held synapse; a very large synapse in the mammalian auditory brainstem that functions to differentiate between temporal activation of cochlear hair cells in each ear to aid in sound localization (Tsuchitani, 1997). The AP at the mammalian calyx of Held has been shown to become briefer in duration over development (560 µs FWHM before hearing onset and 190 µs after hearing onset), but has been shown not to change in amplitude over this same time period (Taschenberger & von Gersdorff, 2000). This AP duration change is thought to be caused by changes in presynaptic voltage-gated sodium channels (faster inactivation and recovery) and potassium channels (higher density and faster activation kinetics) (Elezgarai et al., 2003; Leao et al., 2005; Nakamura & Takahashi, 2007). The very short duration of mature APs at the calyx of Held reduces the activation of presynaptic VGCCs, decreasing the probability of release from each of the roughly 700 AZs (Borst & Sakmann, 1998; Taschenberger et al., 2002; Yang & Wang, 2006). These and other developmental refinements at the calyx of Held lead to fast and dependable communication at this relay synapse. The NMJ is also a strong and reliable relay synapse that is expected to release enough transmitter with each AP to trigger postsynaptic muscle contraction (Wood & Slater, 2001). The NMJ accomplishes this strength and reliability by assembling hundreds of presynaptic AZs that each contain 20-40 single vesicle release sites (docked vesicles and their associated VGCCs). In contrast to the calyx of Held synapse, the frog NMJ does not show frequency-dependent depression, and in fact typically displays facilitation during pairs or short trains of APs (Laghaei et al., 2018). This is likely due in part to the very low probability for release at each of the thousands of single vesicle release sites contained within hundreds of AZs (Tarr et al., 2013b). In this way, a very brief presynaptic AP can ensure that very few presynaptic VGCCs open (Luo et al., 2015; Luo et al., 2011), sparing most release sites from participating in AP-evoked release. This mechanism may aid in preserving transmitter release-ready capability during subsequent APs, even at high frequency.

2.4.2 Changes in the width of the AP waveform can explain proximal-distal changes in neurotransmitter release

To computationally predict how proximal-distal changes in the AP waveform could alter calcium triggered transmitter release, we input our experimentally-imaged AP waveforms from the three regions of the presynaptic nerve terminal of the frog NMJ (Figure 8F) into an MCell simulation of 10000 VGCCs (Figure 13A; see section 2.2.4). This simulation predicted that the probability of VGCCs opening during a single AP were .203, .307, and .436 for APs from near the end, the middle, and near the last node, respectively, and also predicted a 48% increase in total calcium flux between the end and middle AP waveform, and a 119% increase in calcium flux between the nerve terminal end and AP waveform near the last node (Figure 13B). Next, we used these APs in our previously validated MCell model of a frog AZ (see section 2.2.4; (Dittrich et al., 2013; Homan et al., 2018; Laghaei et al., 2018; Ma et al., 2014)). The frog AZ model predicted large differences in the magnitude of transmitter release caused by the APs recorded from different regions of the motor nerve terminal, with the AP waveform from near the last node of Ranvier triggering approximately double the transmitter release as comparted to the AP waveform recorded near the middle, and approximately four times the transmitter release as compared to the AP waveform recorded near the end of the nerve terminal (Figure 13C). These computational results show that small changes in the width of the AP waveform can result in large changes in presynaptic calcium entry and transmitter release (Figure 13B, C). Furthermore, these results are consistent with the proximal-distal gradient in the magnitude of transmitter release along the frog motor nerve terminal reported by D’Alonzo and Grinnell (D'Alonzo & Grinnell, 1985). Therefore, we hypothesize that changes in the AP waveform along the length of the adult frog motor nerve terminal may be responsible for the proximal-distal decrease in neurotransmitter release found at the presynaptic nerve terminal of the frog NMJ (Figure 14).

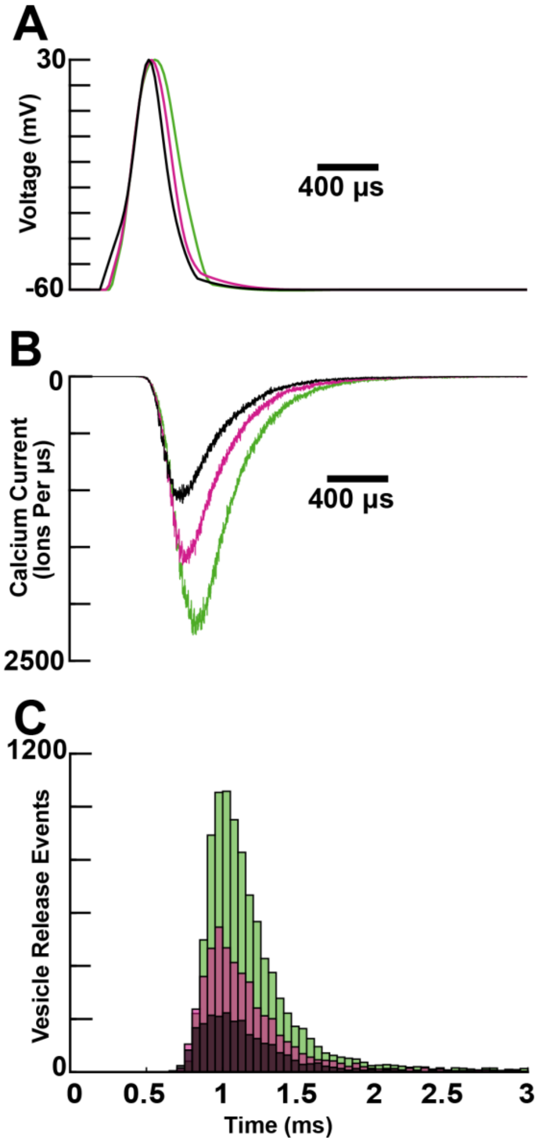

Figure 13 MCell predictions for calcium entry and transmitter release induced by AP waveforms measured from three distinct electrical regions of the nerve terminal.

A, AP waveforms used for computational simulations based on the recorded AP waveforms from near the last node of Ranvier (green), the middle region of the nerve terminal (magenta), and near the end of the nerve terminal (black). **B,** Predicted calcium current induced by each AP near the last node of Ranvier (green), the middle region of the nerve terminal (magenta), and the end of the nerve terminal (black) based on a MCell box simulation of 10,000 VGCCs. **C,** Histogram of the time course of vesicle release events predicted from 4800 runs of the frog active zone MCell model in response to calcium-entry triggered vesicle fusion induced by the APs measured from near the last node of Ranvier (green), the region of the nerve terminal (magenta), and the end of the nerve terminal (black).

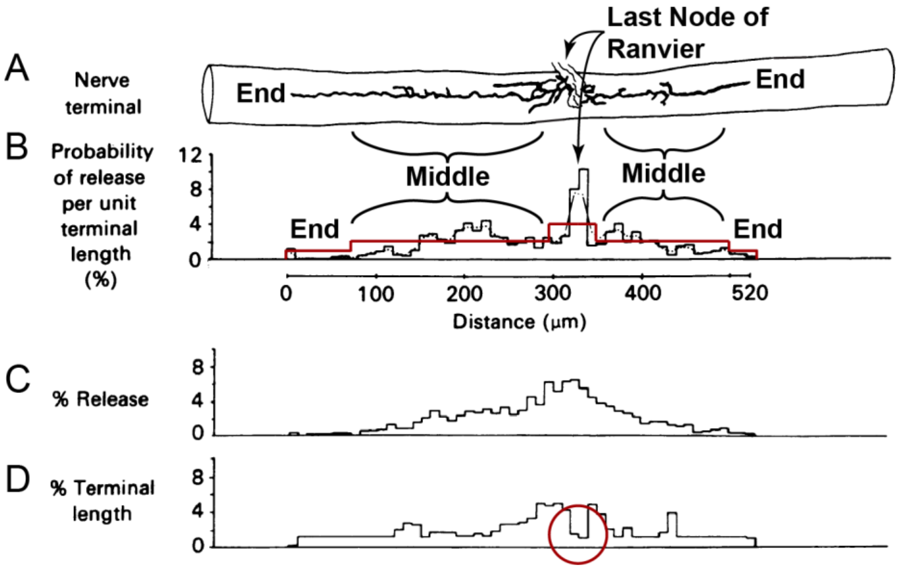

Figure 14 Changes in the AP waveform along the length of the adult frog motor nerve terminal may be responsible for the proximal-distal decrease in neurotransmitter release found at the presynaptic nerve terminal of the frog NMJ.

An outline of a single adult frog NMJ (**A**) and the associated histograms of the measured probability of release along the length of this nerve terminal. In this figure, adapted from (D'Alonzo & Grinnell, 1985), the probability of release per unit nerve length (**B**) is greatest near the last node of Ranvier, relatively constant through the middle region of the terminal, and lowest near the ends of the terminal. Red line shows changes in transmitter release predicted by our model shown in Figure 13. **C,** Raw data from **B** that was not normalized to the nerve terminal length. **D,** Variations in the measured nerve terminal length. Red circle identifies the last node of Ranvier where measured nerve terminal length is very short, leading to the relatively large increase in probability of release per unit terminal length at this central position shown in **B**. Except for this large peak in release at the nodal entry point (created by the short nerve terminal length calculated at this location), our model predictions based on changes in AP duration closely predict the measured changes in transmitter release probability along the length of this sample NMJ. Therefore, we hypothesize that these changes in transmitter release could be caused by the changes in the AP waveform we measured along the length of similar frog NMJs.

2.4.3 Relationship between axon width, the duration of the AP waveform, and AP propagation speed

We measured the propagation speed along the length of the adult frog motor nerve terminals and determined the average to about 0.6 m/s. This value is relatively slow when compared to the range of propagation speeds previously measured in mammalian peripheral axons, (even when accounting for temperature differences, for which a Q10 of 1.5 has been reported for AP conduction velocities at the squid giant synapse; Rosenthal & Bezanilla, 2000) which can range from about 120 m/s for the fastest large diameter (~20 μm) myelinated axons, to about 0.3 m/s for small diameter (~0.1 μm) unmyelinated axons (Swadlow & Waxman, 2012). Theoretically, the diameter of a nerve terminal should impact the AP waveform shape and propagation speed along a long linear nerve terminal. However, by comparing the width of the nerve terminal with both the FWHM of the AP waveform and the AP propagation speed we found no significant correlation. We hypothesize that this is because the distribution of ion channels plays a much larger role in determining the shape of the AP waveform such that modest changes in nerve terminal geometry have a negligible impact. Neurons are known to use a large variety of voltage-gated sodium and potassium channels that can lead to different AP shapes (Bean, 2007). In particular, fast-spiking neurons that employ very brief APs express higher densities of specific types of voltage-gated potassium channels (Rudy & McBain, 2001). In fact, even within the same neuron, APs can differ significantly when comparing the soma with the nerve terminal due to a non-uniform distribution of voltage-gated sodium and potassium channels (Geiger & Jonas, 2000). It is thought that the presynaptic terminal of the frog NMJ contains voltage-gated sodium channels (although the subtype is unknown, they are expected to be similar to the TTX-sensitive channels reported in mammalian axons (Caldwell et al., 2000), and BK channels have been localized selectively to AZs within frog NMJs (Robitaille, Adler, & Charlton, 1993a; Robitaille et al., 1993b). The types of voltage-gated potassium channels are unknown, but we hypothesize that the presynaptic terminal of the frog NMJ might contain Kv3 subtypes based on reports in mammalian motor nerve terminals (Brooke et al., 2004; Zemel et al., 2018). Despite decades of study, with the exception of AZ-localized BK channels (Robitaille et al., 1993a; Robitaille et al., 1993b), little is known of the expression of sodium and potassium channels within the adult frog motor nerve terminal. Further studies aimed at elucidating the density and distribution of these channels within the frog NMJ will be required to determine the mechanisms responsible for changes in the AP waveform.

3.0 A high affinity, partial antagonist effect of 3,4-diaminopyridine mediates action potential broadening and enhancement of transmitter release at NMJs

3,4-diaminopyridine (3,4-DAP) increases transmitter release from neuromuscular junctions (NMJs), and low doses of 3,4-DAP (estimated to reach ~1 μM in serum) are the FDA-approved treatment for neuromuscular weakness caused by Lambert-Eaton Myasthenic Syndrome (LEMS). Canonically, 3,4-DAP is thought to block voltage-gated potassium (Kv) channels, resulting in prolongation of the presynaptic action potential (AP). However, recent reports have shown that high concentrations of 3,4-DAP have an off-target agonist effect on the Cav1 subtype ("L-type") of voltage-gated calcium (Cav) channels, and have speculated that this agonist effect might contribute to 3,4-DAP effects on transmitter release at the NMJ. To address 3,4-DAP's mechanism(s) of action, we first use patch-clamp electrophysiology to characterize the concentration-dependent block of 3,4-DAP on the predominant presynaptic Kv channel subtypes found at the mammalian NMJ (Kv3.3 and Kv3.4). We identify a previously unreported high-affinity (1-10 μM) partial antagonist effect of 3,4-DAP in addition to the well-known low affinity (0.1-1mM) antagonist activity. Next, we use voltage imaging to show that 3,4-DAP broadens the AP waveform in a dose dependent manner, independent of Cav1 calcium channels. Finally, we demonstrate the 3,4-DAP augments transmitter release in a dose-dependent manner and this effect is also independent of Cav1 channels. From these results, we conclude that low concentrations of 3,4-DAP act solely on Kv channels to mediate AP broadening and enhance transmitter release at the NMJ.

3.1 Introduction

Lambert-Eaton Myasthenic syndrome (LEMS) is a neuromuscular disease caused by an autoantibody-mediated attack on the presynaptic Cav2.1 type (also called “P/Q-type”) voltage-gated calcium channels as well as other presynaptic proteins at neuromuscular junctions (NMJs) (Lambert, Eaton, & Rooke, 1956; Lang et al., 1983; Meriney et al., 1996; Nagel et al., 1988; Tarr et al., 2013b; Vincent et al., 1989). The resulting antibody-mediated loss of proteins associated with transmitter release sites results in a reduction of acetylcholine release from the NMJ and leads to a failure of some postsynaptic muscle fibers to initiate an action potential (AP), leading to a weaker muscle contraction. Clinical and animal model studies suggest that neuromuscular transmission, and subsequently muscle strength, can be improved by the use of 3,4-diaminopyridine (3,4-DAP), which is a small molecule that acts as an antagonist at voltage-gated potassium (Kv) channels. 3,4-DAP was recently approved by the FDA to treat LEMS (FDA, 2018, 2019; Voelker, 2019; Yoon et al., 2020), and has been shown to be effective at increasing neuromuscular strength in LEMS patients (Oh, 2016; Sanders et al., 2018; Shieh et al., 2019; Strupp et al., 2017). However, 3,4-DAP has dose-dependent side effects that restrict the amount that patients take to relatively small doses, which prevents full symptomatic relief in many LEMS patients (Lindquist & Stangel, 2011; Wirtz et al., 2010). Patients are typically prescribed 10-20 mg oral doses of 3,4-DAP to be taken several times during the day and report peak clinical effects for 3-8 hours after each dose (Sanders, 1998). 3,4-DAP has been reported to have a serum half-life of 1-3 hours, and pharmacokinetic studies cite peak serum concentrations of ~40-110 ng/ml after a 20 mg oral dose (Haroldsen et al., 2015a; Haroldsen et al., 2015b; Ishida et al., 2015; Thakkar et al., 2017; Wirtz et al., 2009). Similar doses of 3,4-DAP have also been used off-label for a variety of other neuromuscular weakness conditions, including congenital myasthenic syndrome (Banwell et al., 2004; Natera-de Benito et al., 2016a; Natera-de Benito et al., 2016b; Rodríguez Cruz et al., 2016; Rodríguez Cruz et al., 2019; Witting et al., 2015), muscle-specific receptor tyrosine kinase myasthenia gravis (Bonanno et al., 2018), downbeat nystagmus (Thurtell & Leigh, 2012), and multiple sclerosis (Flet et al., 2010; Mainero et al., 2004; Polman et al., 1994; Sheean et al., 1998).

The mechanism of action of 3,4-DAP at neuromuscular synapses is canonically thought to be a block of Kv3 (also called "A-type") voltage-gated potassium channels. Kv3.3 and Kv3.4 channels are the subtypes selectively localized at mammalian neuromuscular motor nerve terminals (Brooke et al., 2004; Zemel et al., 2018) and are thought to be predominantly responsible for speeding the repolarization of the presynaptic AP. By blocking Kv3 channels, 3,4-DAP is hypothesized to broaden the presynaptic AP duration, thus indirectly increasing calcium ion flux by increasing the number of presynaptic voltage-gated calcium (Cav2) channels that open during an AP. Because calcium-triggered acetylcholine release is non-linearly dependent on calcium concentration in nerve terminals, a relatively small increase in calcium ion entry can generate a much larger increase in neurotransmitter release (Dodge & Rahamimoff, 1967).

Recent investigations have challenged the conventional mechanism of action of aminopyridines. First, prior concentration-response studies of aminopyridine action on Kv channels have often been restricted to the use of 4-aminopyridine, and yielded an IC_{50} between 30 μM – 2.5 mM depending on the types of potassium channels expressed (Castle et al., 1994; Grissmer et al., 1994; Luneau et al., 1991; Muqeem et al., 2018; Rettig et al., 1992; Schaarschmidt et al., 2009; Stephens et al., 1994; Vega-Saenz de Miera et al., 1992; Wu et al., 2009; Yokoyama et al., 1989), with a high sensitivity to 4-aminopyridine reported for Kv3 channels (80 μM IC_{50}; (Kirsch & Drewe, 1993)). Because 4-AP crosses the blood-brain barrier better than 3,4-DAP, the latter has been preferred for the treatment of peripheral neuromuscular diseases (Lemeignan et al., 1984; Lindquist & Stangel, 2014). Therapeutic concentrations of 3,4-DAP are predicted to be in the low micromolar range, and 3,4-DAP has been reported to have significant effects on squid giant axon potassium channels at these concentrations (Kirsch & Narahashi, 1978). Second, a direct agonistic action of 3,4-DAP on Cav1 type (also called “L-type”) voltage-gated calcium channels was reported (Li et al., 2014; Wu et al., 2009). However, the clinical relevance of the reported effects of 3,4-DAP on Cav channels was debated because the 3,4-DAP concentrations evaluated in these studies were significantly above blood serum levels found in LEMS treatment conditions (Meriney & Lacomis, 2018; Wu, Chen, & Pan, 2018b). Furthermore, because Cav1 channels usually lack the synaptic protein interaction sites present in Cav2 channels (Catterall, 1999; Mochida et al., 2003; Sheng et al., 1998), Cav1 channels are thought to reside outside of synaptic vesicle release sites in the neuromuscular junction and therefore are not thought to directly control acetylcholine release (as Cav2 channels do) at healthy synapses. However, it is possible that Cav1 channels may have a minor role at neuromuscular synapses that is revealed under pharmacological conditions (Atchison, 1989; Atchison & O'Leary, 1987; Flink & Atchison, 2002; Pancrazio, Viglione, & Kim, 1989; Urbano, Rosato-Siri, & Uchitel, 2002), and Cav1 channels may have a compensatory contribution to the control of transmitter release in diseased conditions such as LEMS (Flink & Atchison, 2002; Xu et al., 1998).

Therefore, to investigate the physiological mechanism accounting for the clinical response to 3,4-DAP, we tested the effects of a therapeutic concentration of 3,4-DAP (1.5 μM) on (a) peak currents of Kv3 channels expressed in HEK293T cells, (b) the presynaptic AP waveform at frog and mouse motor nerve terminals, and (c) transmitter release from weakened frog and mouse NMJs. To explore the role of Cav1 channels in 3,4-DAP-mediated effects at NMJs, we conducted our transmitter release and AP experiments in the presence or absence of a Cav1 antagonist (nitrendipine) and compared the results. In addition, we examined the effects of a supra-therapeutic concentration of 3,4-DAP (100 μM) to allow direct comparisons with prior studies that employed this higher concentration (Li et al., 2014; Wu et al., 2018b; Wu et al., 2009). For the purpose of this report, we define a supra-therapeutic concentration as one that is about 100 fold higher (100 μM) than the measured concentration in the serum of LEMS patients after taking the typical prescribed dose of 3,4-DAP (Haroldsen et al., 2015a; Haroldsen et al., 2015b; Ishida et al., 2015; Thakkar et al., 2017; Wirtz et al., 2009).

Our results demonstrate that the therapeutic concentration of 1.5 μM 3,4-DAP has a small but significant effect on both Kv3.3 and Kv3.4 channels, and we show that this concentration broadens the presynaptic AP waveform to increase the magnitude of neuromuscular transmission independent of a Cav1 contribution. The effect of the supra-therapeutic concentration of 100 μM 3,4-DAP was more pronounced, but broadening of the AP and the increase in the magnitude of transmitter released remained independent of effects on Cav1 channels. These results support the hypothesis that the clinical effects of 3,4-DAP in the treatment of LEMS are caused by a partial block of voltage-gated potassium channels, independent of any effects of Cav1 voltage-gated calcium channels.

3.2 Results

3.2.1 3,4-DAP effects on Kv3 potassium channels

When considering which subtypes of Kv channels might be blocked by 3,4-DAP within mammalian motor nerve terminals, we were guided by prior work at the mouse NMJ which demonstrated that Kv3.3 and Kv3.4 were the subtypes detected by immunohistochemistry (Brooke et al., 2004). To determine the concentration-dependent effects of 3,4-DAP on these channel types, we expressed Kv3.3 and Kv3.4 channels in HEK293T cells and used whole-cell patch clamp electrophysiology to measure the change in current after 3,4-DAP application. Using a 100 or 500 ms step depolarization protocol (-100 mV to +40 mV), we activated Kv3.3 or Kv3.4 current and then measured the peak current before and after application of 3,4-DAP (at concentrations ranging between 0.15 - 5000 μM). We found a concentration-dependent block of both Kv3.3 and Kv3.4 currents that was similar for each channel subtype. Importantly, the therapeutic concentration of 3,4-DAP (1.5 μM) significantly reduced Kv3.3 and Kv3.4 currents by about 10% (Figure 15). We observed that the concentration-response relationship appeared to be best fit by a biphasic Hill equation (Figure 15; Prism, GraphPad, San Diego, CA). For Kv3.3 and Kv3.4, the high affinity fit yielded IC_{50} values of 2.5 and 10.3 μM and Hill coefficients of 0.7 and 0.6 respectively. Because the maximum inhibition for this high affinity activity was approximately 20-25%, 3,4-DAP binding to high affinity sites on Kv3.3 and Kv3.4 exhibited partial antagonist activity. The low affinity fits of the Kv3.3 and Kv3.4 data yielded IC_{50} values of 151 and 231 μM and Hill coefficients of 3.0 and 1.4 respectively. The maximum inhibition for this low affinity activity was near 100%.

Because we were interested in a therapeutic concentration of 3,4-DAP with respect to its effect on calcium-triggered transmitter release at the NMJ, we confirmed that 1.5 µM 3,4-DAP had no effect on Cav2.1 or Cav1.2 current. When comparing the peak and integral of calcium current before and after application of 1.5 µM 3,4-DAP, we found no significant effects on either Cav2.1 (drug/control = 1.04 ± 0.08 peak; 1.01 ± 0.09 integral; *n* = 3; mean ± SD) or Cav1.2 (drug/control = 0.95 ± 0.21 peak; 0.94 ± 0.08 integral; *n* = 3; mean ± SD) currents.

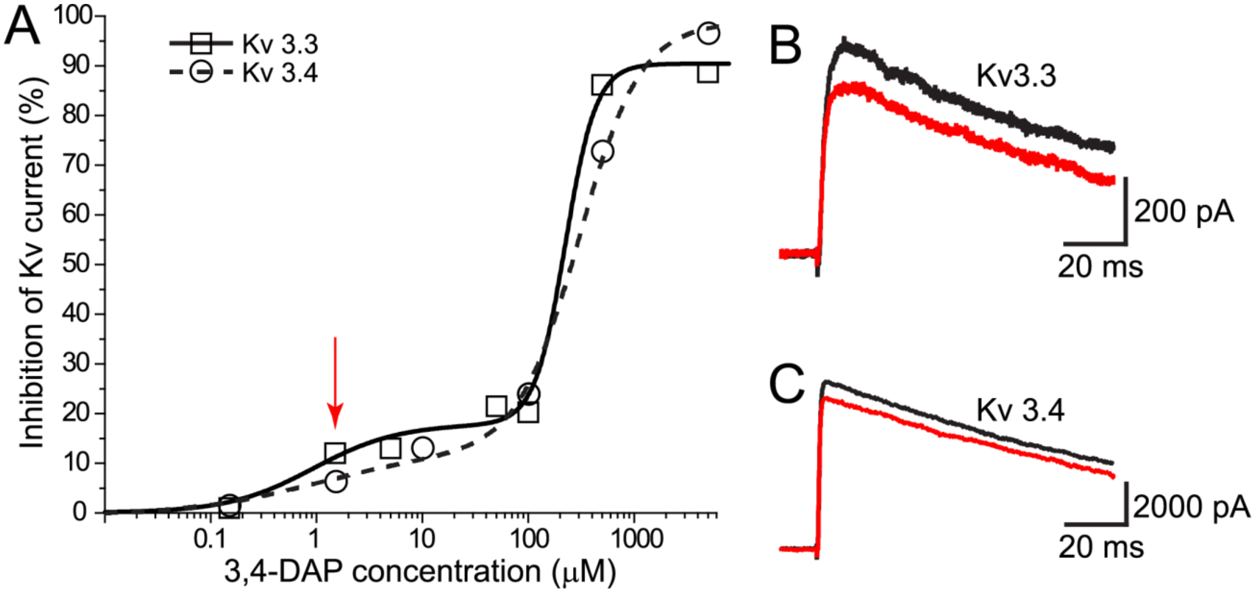

Figure 15 Concentration-dependent effects of 3,4-DAP on Kv3.3 and Kv3.4 potassium currents expressed in HEK293T cells.

A, plot of the inhibition of current through Kv3.3 (open squares, solid fit line) and Kv3.4 (open circles, dashed fit line) channels after exposure to varying concentrations of 3,4-DAP; *n* = 3-6. The red arrow indicates the data at 1.5 µM 3,4-DAP concentration for which sample currents are shown in *B* and *C*; S.D. bars are smaller than the symbol sizes. *B*, sample Kv3.3 currents activated by a voltage step from -100 mV to +40 mV and shown before (black trace) and after (red trace) exposure to 1.5 µM 3,4-DAP. *C*, sample Kv3.4 currents activated by a voltage step from -100 mV to +40 mV and shown before (black trace) and after (red trace) exposure to 1.5 µM 3,4-DAP.

3.2.2 3,4-DAP effects on the presynaptic AP waveform at the NMJ

The mechanism of action underlying the effects of 3,4-DAP at the NMJ is canonically thought to be due to a partial block of presynaptic Kv channels leading to a broadening of the presynaptic AP. To date, no studies have directly measured 3,4-DAP-mediated effects on the presynaptic AP waveform at the neuromuscular junction. Thus, we utilized a voltage-sensitive fluorescent dye (BeRST 1;(Huang et al., 2015)) to directly measure the impact of 3,4-DAP on the duration of the presynaptic AP waveform at frog and mouse NMJs. The BeRST 1 dye is fast enough to resolve the AP and has been shown to not affect the electrical properties or AP waveforms of neurons (Huang et al., 2015). We performed a paired experiment where the control AP waveform was recorded from a single nerve terminal, which was then was exposed to 3,4-DAP for 30 minutes before the AP waveform was recorded again at the same nerve terminal. To determine the duration of the presynaptic AP waveform, we measured the full width at half maximum (FWHM) of the recorded AP waveforms. This technique was performed in separate neuromuscular preparations in either vehicle or nitrendipine conditions to determine if blocking Cav1 channels affected the 3,4-DAP-mediated effects on the AP waveform.

To ensure that AP duration was not altered by prolonged experimental time in the imaging setup, we performed the imaging procedure on control experiments without 3,4-DAP over the same time course as a typical 3,4-DAP experiment. We found no significant changes in AP duration during these control experiments, demonstrating that our imaging procedure itself was not impacting the AP waveform (data not shown).

We first measured the impact of a therapeutic concentration of 1.5 μM 3,4-DAP on the duration of the presynaptic AP waveform at mouse motor nerve terminals (Figure 16). We found that 1.5 μM 3,4-DAP broadened the presynaptic AP in vehicle-treated mouse NMJs, increasing the FWHM of the AP waveform from 262.2 ± 40.7 µs to 332.2 ± 49.6 µs. The presence of nitrendipine did not significantly alter the impact of 1.5 µM 3,4-DAP, with the FWHM of the AP waveform in the nitrendipine-treated mouse NMJs increasing from 266.1 ± 50.0 µs to 306.7 ± 30.5 µs after the application of 1.5 µM 3,4-DAP (Figure 16E).

We next investigated the impact of 1.5 μM DAP on the AP waveform at frog motor nerve terminals to determine if the effects of 3,4-DAP on the AP waveform are conserved across species (Figure 17). We found that 1.5 μM 3,4-DAP broadened the presynaptic AP in vehicle-treated frog NMJs, increasing the FWHM of the AP waveform from 272.5 ± 16.9 µs to 519.5 ± 120.5 µs. Again, we found no significant impact of the presence of nitrendipine on the effect of 1.5 µM 3,4-DAP, with the FWHM of the AP waveform in the nitrendipine-treated frog NMJs increasing from 277.9 ± 22.9 µs to 481.3 ± 58.3 µs after the application of 1.5 µM 3,4-DAP (Figure 17E).

Finally, we tested the impact of a supra-therapeutic concentration (100 µM) of 3,4-DAP on the duration of the presynaptic AP waveform at the frog NMJ (Figure 18). In vehicle-treated frog NMJs, 100 μM 3,4-DAP broadened the duration of the AP waveforms from a FWHM of 280.4 ± 32.6 µs to 1729.7 ± 197.0 µs. Even at this higher concentration of 3,4-DAP, we did not see any significant impact of nitrendipine on the 3,4-DAP-mediated broadening of the presynaptic AP waveform. The FWHM of the AP waveform in the nitrendipine-treated frog NMJs increased from 270.9 ± 51.1 µs to 1925.4 ± 210.3 µs after the application of 100 µM 3,4-DAP (Figure 18C).

These data demonstrate that 3,4-DAP increases the duration of the presynaptic AP waveform at mammalian and frog NMJs in a dose-dependent manner, and that Cav1 calcium channels have no interaction with this effect. Since small changes in the duration of the AP waveform can greatly increase calcium flux and transmitter release at the NMJ (Dodge & Rahamimoff, 1967; Ginebaugh et al., 2020), these data further support the hypothesis that broadening of the presynaptic AP via the blocking of Kv3 channels is the primary mechanism by which 3,4-DAP increases transmitter release *in vivo*.

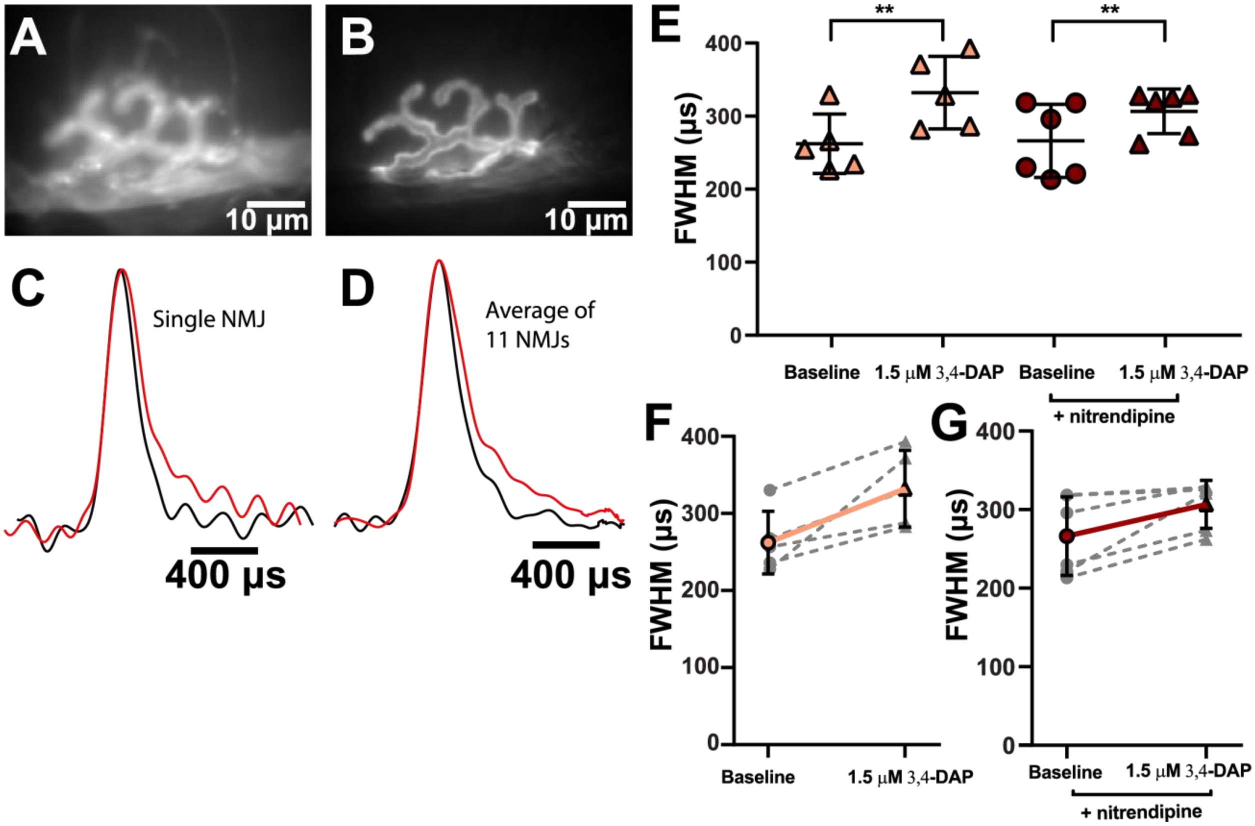

Figure 16 Therapeutic concentrations of 3,4-DAP broaden the presynaptic AP waveform independent of Cav1 channels at the mammalian NMJ.

A, a BeRST 1 dye-stained image of a mammalian presynaptic motor nerve terminal. *B*, an Alexa Fluor 488 α-BTX stained image of the same terminal as in *A*. *C*, normalized splines of presynaptic AP waveforms recorded from a single nerve terminal before (black) and after (red) the addition of 1.5 µM 3,4-DAP. *D*, the normalized average of all pre-drug (black) and post 1.5 µM 3,4-DAP (red) presynaptic AP waveform splines recorded from mammalian motor nerve terminals (*n* = 11). *E*, FWHMs of recorded AP waveforms before (circles) or after (triangles) 1.5 µM 3,4-DAP application to vehicle (peach) or nitrendipine (red) treated mouse NMJs. 1.5 µM 3,4-DAP significantly broadens the AP waveform independent of nitrendipine (two-way mixed ANOVA: there was a significant main effect of 1.5 µM 3,4-DAP (F (1,9) = 22.40, ***p* = 0.0011), but no main effect of nitrendipine (F (1,9) = 0.2139, *p* = 0.6547), or interaction between 1.5 µM 3,4-DAP and nitrendipine (F (1,9) = 1.583, *p* = 0.2399); vehicle, *n* = 5; nitrendipine, *n* = 6). *F-G*, plots of individual paired recorded values (grey dotted lines) of AP duration (FWHM) before and after application of 1.5 µM 3,4-DAP with a superimposed average (vehicle, solid peach line; nitrendipine, solid red line).

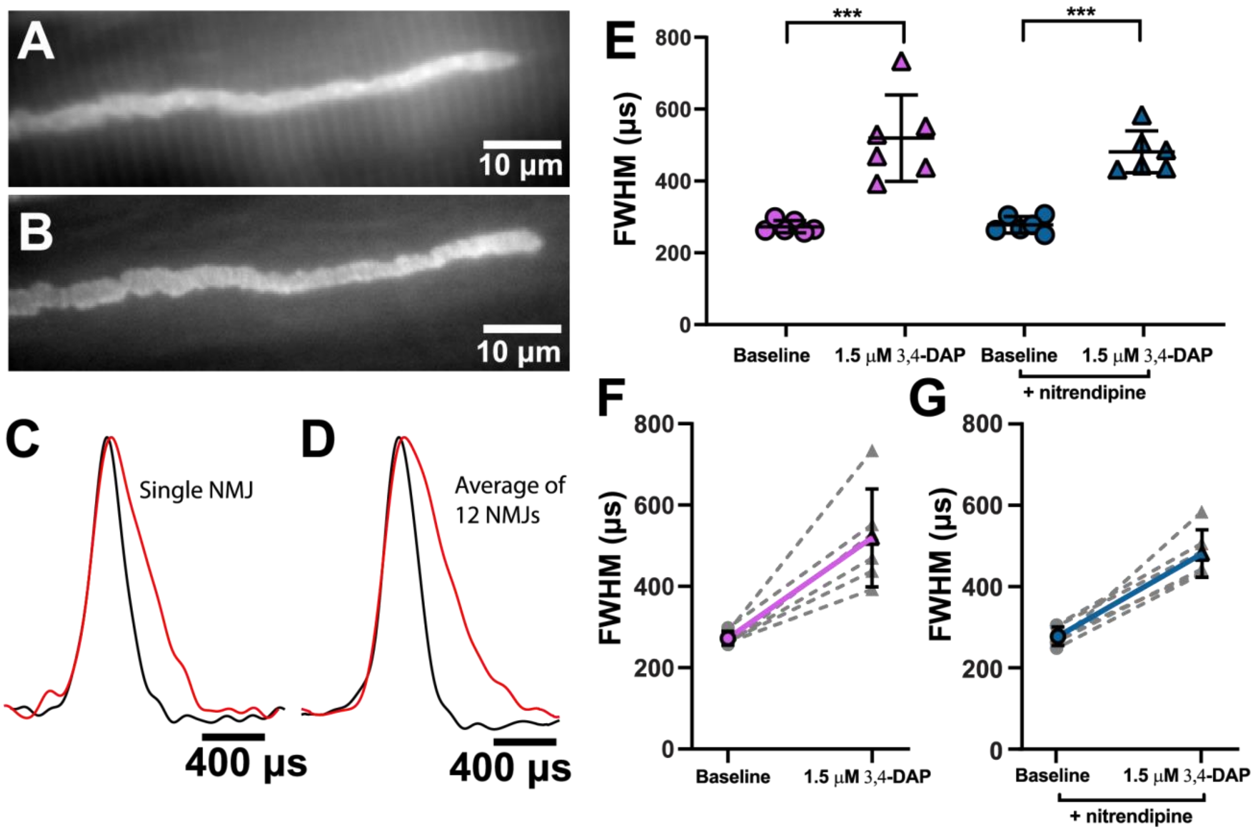

Figure 17 Therapeutic concentrations of 3,4-DAP broaden the presynaptic AP waveform independent of Cav 1 channels at the frog NMJ.

A, a BeRST 1 dye-stained image of a frog presynaptic motor nerve terminal. *B*, an Alexa Fluor 488 α-BTX stained image of the same terminal as in *A*. *C*, normalized presynaptic AP waveform splines recorded from a single nerve terminal before (black) and after (red) the addition of 1.5 µM 3,4-DAP. *D*, the normalized average of all pre-drug (black) and post-1.5 µM 3,4-DAP (red) presynaptic AP waveform splines recorded from all frog motor nerve terminals (n = 12). *E*, FWHMs of recorded AP waveforms before (circles) or after (triangles) 1.5 µM 3,4-DAP application to vehicle (pink) or nitrendipine (blue) treated frog NMJs. 1.5 µM 3,4-DAP broadens the AP waveform independent of nitrendipine (two-way mixed ANOVA: there was a significant main effect of 1.5 µM 3,4-DAP (F (1,10) = 77.68, ***$p < 0.0001$), but no main effect of nitrendipine (F (1,10) = 0.2967, $p = 0.5979$), and no significant interaction between 1.5 µM 3,4-DAP and nitrendipine (F (1,10) = 0.7278, $p = 0.4136$); vehicle, $n = 6$; nitrendipine, $n = 6$). *F-G*, plots of individual paired recorded values (grey dotted lines) of AP duration (FWHM) before and after application of 1.5 µM 3,4-DAP with a superimposed average (vehicle, solid pink line; nitrendipine, solid blue line).

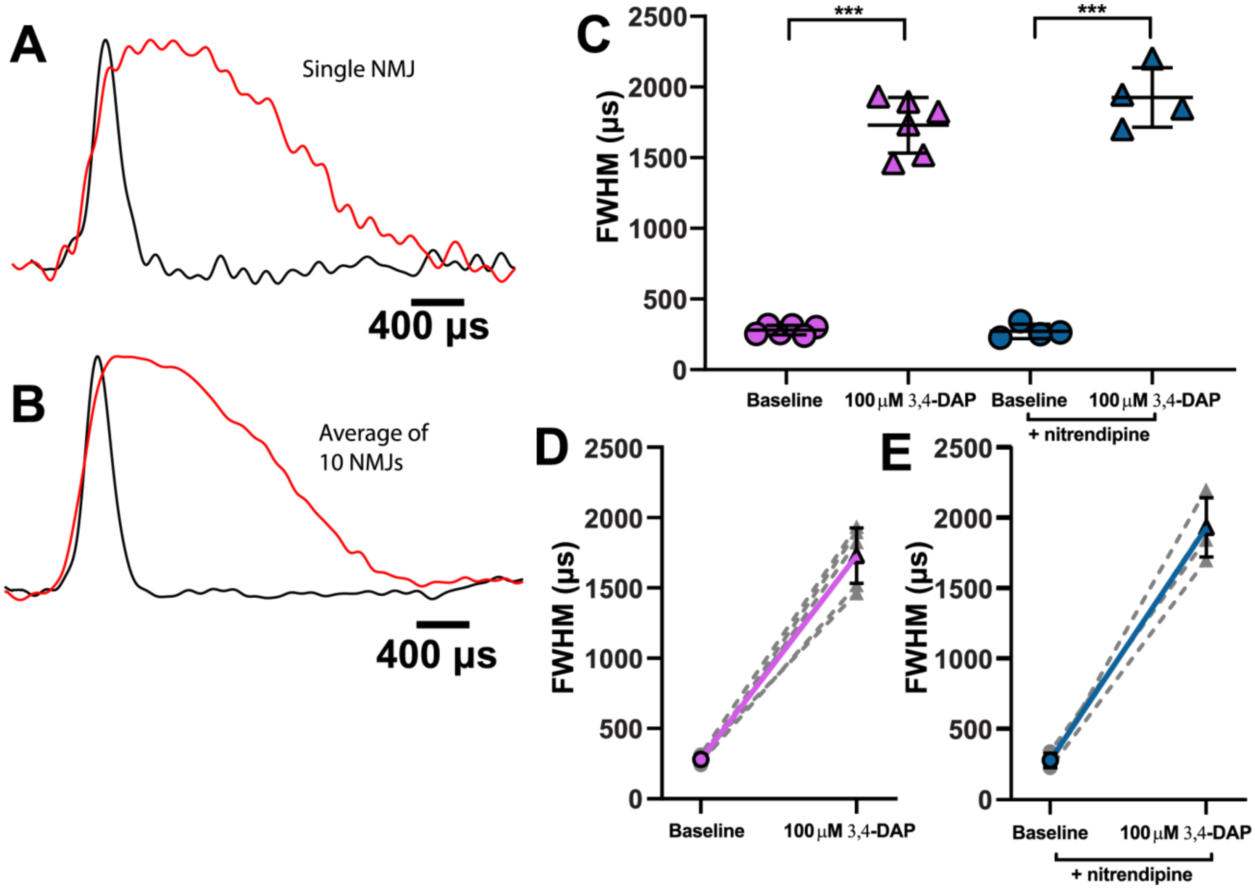

Figure 18 A supra-therapeutic concentration of 100 µM 3,4-DAP significantly broadens the frog presynaptic AP waveform independent of Cav1 channels.

A, normalized presynaptic AP waveform splines recorded from a nerve terminal before (black) and after (red) the addition of 100 µM 3,4-DAP. *B*, the normalized average of all pre-drug (black) and post 100 µM 3,4-DAP (red) presynaptic AP waveform splines recorded from all frog motor nerve terminals (*n* = 10). *C*, FWHMs of recorded AP waveforms before (circles) or after (triangles) 100 µM 3,4-DAP application to vehicle (pink) or nitrendipine (blue) treated frog NMJs. 100 µM 3,4-DAP broadens the AP waveform independent of nitrendipine (Two-way mixed ANOVA: significant main effect of 100 µM 3,4-DAP (F (1,8) = 524.7, ****p* < 0.0001), but no main effect of nitrendipine (F (1,8) = 2.035, *p* = 0.1916), and no interaction between 3,4-DAP and nitrendipine (F (1,8) = 2.292, *p* = 0.1685); vehicle, *n* = 6; nitrendipine, *n* = 4). *D-E,* plots of individual paired recorded values (grey dotted lines) of AP duration (FWHM) before and after application of 1.5 µM 3,4-DAP with a superimposed average (vehicle, solid pink line; nitrendipine, solid blue line).

3.2.3 3,4-DAP increases neuromuscular transmission in a dose-dependent manner independent of Cav1 calcium channels

To characterize the dose-dependent effects of 3,4-DAP on weakened transmitter release at the NMJ, we used paired intracellular microelectrode recordings in *ex vivo* neuromuscular preparations to measure endplate potentials (EPPs) in response to nerve-evoked APs, both before and after exposure to either therapeutic (1.5 μM) or supra-therapeutic (100 μM) concentrations of 3,4-DAP. Additionally, we measured spontaneous miniature EPPs (mEPPs) from the same population of muscle fibers to determine quantal content. We performed both EPP and mEPP recordings in the presence or absence of the Cav1 blocker nitrendipine to test the hypothesis that Cav1 calcium channels are important for 3,4-DAP effects.

We reduced the magnitude of transmitter release by performing all recordings in the presence of low concentrations of the calcium channel antagonist ω-agatoxin IVA (for Cav 2.1 channels at mouse NMJs) or ω-conotoxin GVIA (for Cav 2.2 channels at frog NMJs). Reducing transmitter release magnitude following exposure to sub-maximal concentrations of these toxins mimics the effect of neuromuscular diseases that weaken NMJs, and importantly minimizes complications during data analysis due to non-linear summation, ensuring that correction for non-linear summation is accurate (McLachlan & Martin, 1981). In the absence of these selective Cav2 calcium channel blockers, control EPPs average 10-40 mV in amplitude above resting membrane potential (e.g. from -70 mV resting membrane potential to a peak of -60 to -30 mV) at mouse and frog NMJs (Sosa & Zengel, 1993; Tarr et al., 2013b). After exposure to 3,4-DAP (especially the 100 μM concentration), EPP size can approach the acetylcholine receptor channel reversal potential (-10 mV), making 3,4-DAP-induced changes in transmitter release difficult to interpret and analyze. For these reasons, all experiments were performed using sub-maximal concentrations of a calcium channel blocker to reduce quantal content, allowing a more accurate assessment of 3,4-DAP effects on weakened neuromuscular transmission.

We first evaluated the effects of 1.5 μM 3,4-DAP at the mouse NMJ (Figure 19), since mouse NMJs are phylogenetically similar in structure and calcium channel subtype expression to human NMJs. We measured quantal content (QC; the number of vesicles released in response to an AP and calculated as the corrected and normalized mean EPP amplitude divided by corrected and normalized mean mEPP amplitude) in vehicle or nitrendipine conditions because it has been previously hypothesized that 3,4-DAP might increase neurotransmission via a direct effect on Cav1 channels to increase calcium flux (Li et al., 2014; Wu et al., 2009).

We first evaluated the effects of 1.5 μM 3,4-DAP in vehicle-treated mouse NMJs (Figure 19). After exposure to ω-agatoxin IVA, the baseline quantal content averaged approximately 14 (14.2 ± 7.0; Figure 19C-D), while the mean mEPP amplitude was 0.4 ± 0.2 mV, and nerve stimulation produced a mean baseline EPP of 5.2 ± 1.8 mV (Figure 19G-H). Bath application of a therapeutic concentration of 3,4-DAP (1.5 μM) to vehicle-treated NMJs increased EPP amplitudes by approximately 3.2-fold (16.3 ± 5.2 mV; Figure 19H), without altering mEPP amplitudes (0.4 ± 0.2 mV; Figure 19G), and increased quantal content to approximately 44 quanta per trial (44.1 ± 15.3; a 3.1-fold increase; Figure 19C-D). These results are similar to 3,4-DAP effects reported previously in LEMS model mice (Tarr et al., 2014; Tarr et al., 2013b) and in pharmacological conditions with low probability of release (Fiona et al., 2017; Molgó, Lundh, & Thesleff, 1980).

After ω-agatoxin IVA block in the presence of nitrendipine, the mean baseline EPP amplitude averaged 4.8 ± 2.0 mV, the mean mEPP amplitude averaged 0.4 ± 0.1 mV (Figure 19G, I) and the resulting quantal content was 11.7 ± 5.0; Figure 19C, E). After application of 1.5 μM

3,4-DAP, the mean EPP amplitude increased about 3.7-fold (18.5 ± 10.8 mV), without altering mEPP amplitude (0.4 ± 0.2 mV; Figure 19G, I), and quantal content increased 3.6-fold (QC = 41.6 ± 18.9; Figure 19C, E). The presence of nitrendipine did not significantly alter the effects of 1.5 μM 3,4-DAP on quantal content (Figure 19C), indicating that antagonism of Cav1 channels did not alter the effects of a therapeutic concentration (1.5 μM) of 3,4-DAP at mouse NMJs. However, we did observe a significant increase in mEPP frequency in the vehicle condition, but not the nitrendipine condition (vehicle: baseline = 129.3 ± 44.9, post-3,4-DAP = 153.3 ± 49.3; nitrendipine: baseline = 153.3 ± 38.1; post-3,4-DAP = 143 ± 70.9; values are number of events per 30 seconds; Figure 19F).

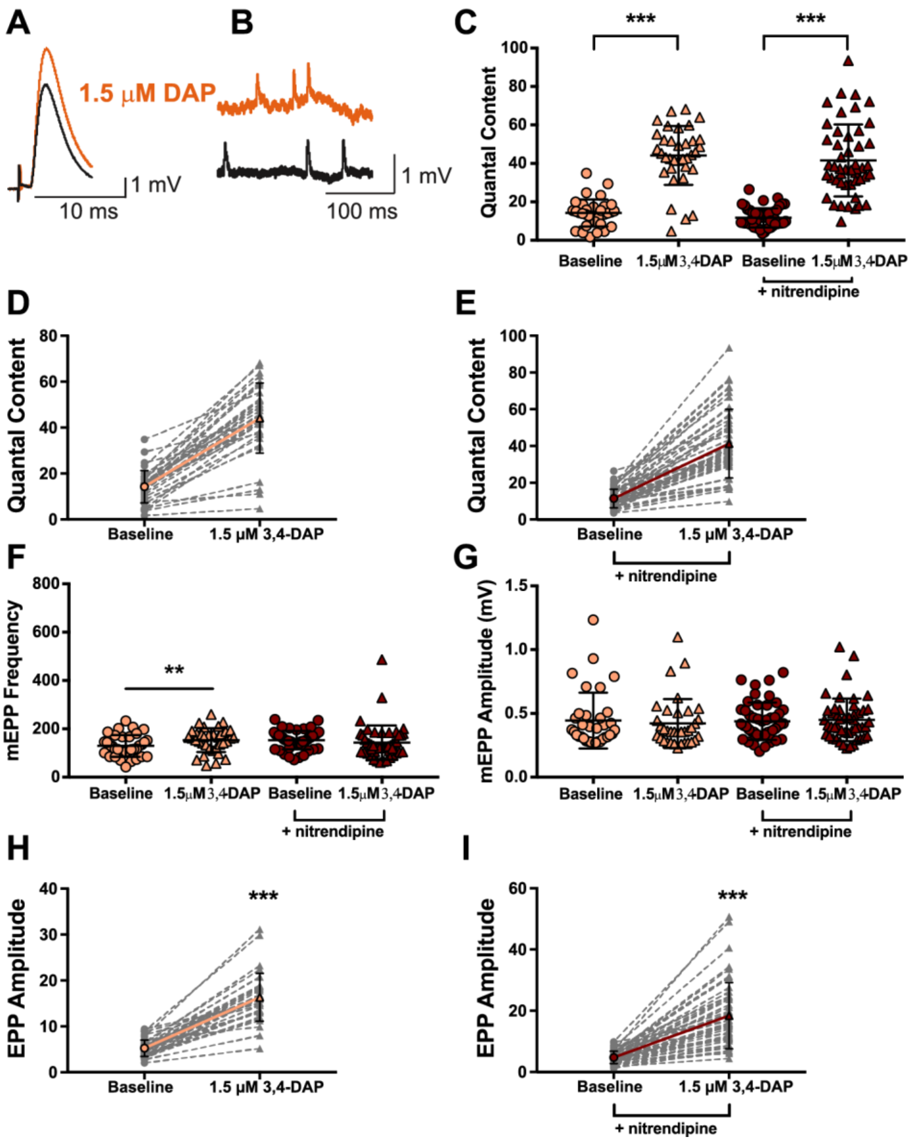

Figure 19 1.5 µM 3,4-DAP dose-dependently increases neuromuscular transmission independent of Cav1 channels in mouse neuromuscular junctions.

A-B, sample traces of electrophysiological recordings of EPPs (*A*) and mEPPs (*B*) before and after 1.5 µM 3,4-DAP application. *C*, quantified quantal content before (circles) or after (triangles) 1.5 µM 3,4-DAP application to vehicle (peach) or nitrendipine (red) -treated mouse NMJs. Two-way mixed ANOVA was used (there was a significant main effect of 1.5 µM 3,4-DAP (F (1, 81) = 347.5, *** $p < 0.0001$); no significant main effect of nitrendipine (F (1,81) = 1.136, $p = 0.2897$) or interaction between 3,4-DAP x nitrendipine (F (1,81) = 0.0002, $p = 0.9887$); vehicle, $n = 35$; nitrendipine $n = 48$). *D-E*, plots of individual paired values (grey dotted lines) with a superimposed average (solid peach line, vehicle; solid red line, nitrendipine). *F*, There was a significant interaction between the effects of 1.5 µM

3,4-DAP and nitrendipine on mEPP frequency (two-way mixed ANOVA; no main effect of nitrendipine; F (1,81) = 0.4209, *p* = 0.5183) or 3,4-DAP; F (1,81) = 1.634, *p* = 0.2048), but a significant interaction between 3,4-DAP x nitrendipine (F (1,81) = 10.02, *p* = 0.0022)). Post-hoc simple main effect analysis showed a significantly increased mEPP frequency in the vehicle (peach, ***p* = 0.0090) but not the nitrendipine (red, *p* = 0.3004) condition. *G*, The 1.5 μM dose of 3,4-DAP did not significantly alter mEPP amplitude in vehicle (peach) or nitrendipine (red) conditions; two-way mixed ANOVA (no significant main effect of nitrendipine; F (1,81) = 0.08568, *p* = 0.7705, or 3,4-DAP; F (1,81) = 0.2994, *p* = 0.5857, nor significant interaction between 3,4-DAP x nitrendipine; F (1,81) = 2.45, *p* = 0.1214). *H-I*, The 1.5 μM dose of 3,4-DAP increased EPP amplitude, shown as individual pairs (grey dotted lines) with a superimposed average (solid peach line, vehicle, *H*; solid red line, nitrendipine, *I*); Wilcoxon signed-rank test, *** $p < 0.0001$.

Next, we evaluated the effects of a supra-therapeutic concentration of 3,4-DAP (100 μM) in vehicle or nitrendipine-treated, 3,4-DAP-naïve mouse NMJ preparations (Figure 20). In NMJs treated with the vehicle, the mean mEPP amplitude was 0.4 ± 0.1 mV, and motor nerve stimulation produced a mean baseline EPP amplitude of 5.8 ± 1.9 mV after exposure to ω-agatoxin IVA (Figure 20G-H). Quantal release under these conditions was approximately 16 (15.5 ± 6.9; Figure 20C-D). After exposure to 100 μM 3,4-DAP, the mean EPP amplitude was significantly increased by approximately 8.8-fold (50.8 ± 12.3 mV), without a significant change in mean mEPP amplitude (0.4 ± 0.2 mV; Figure 20G-H). This resulted in an increase in quantal content from 15.5 quanta per trial to approximately 126 quanta per trial (126.3 ± 35.2), which is an 8.1-fold increase in quantal release (Figure 20C-D).

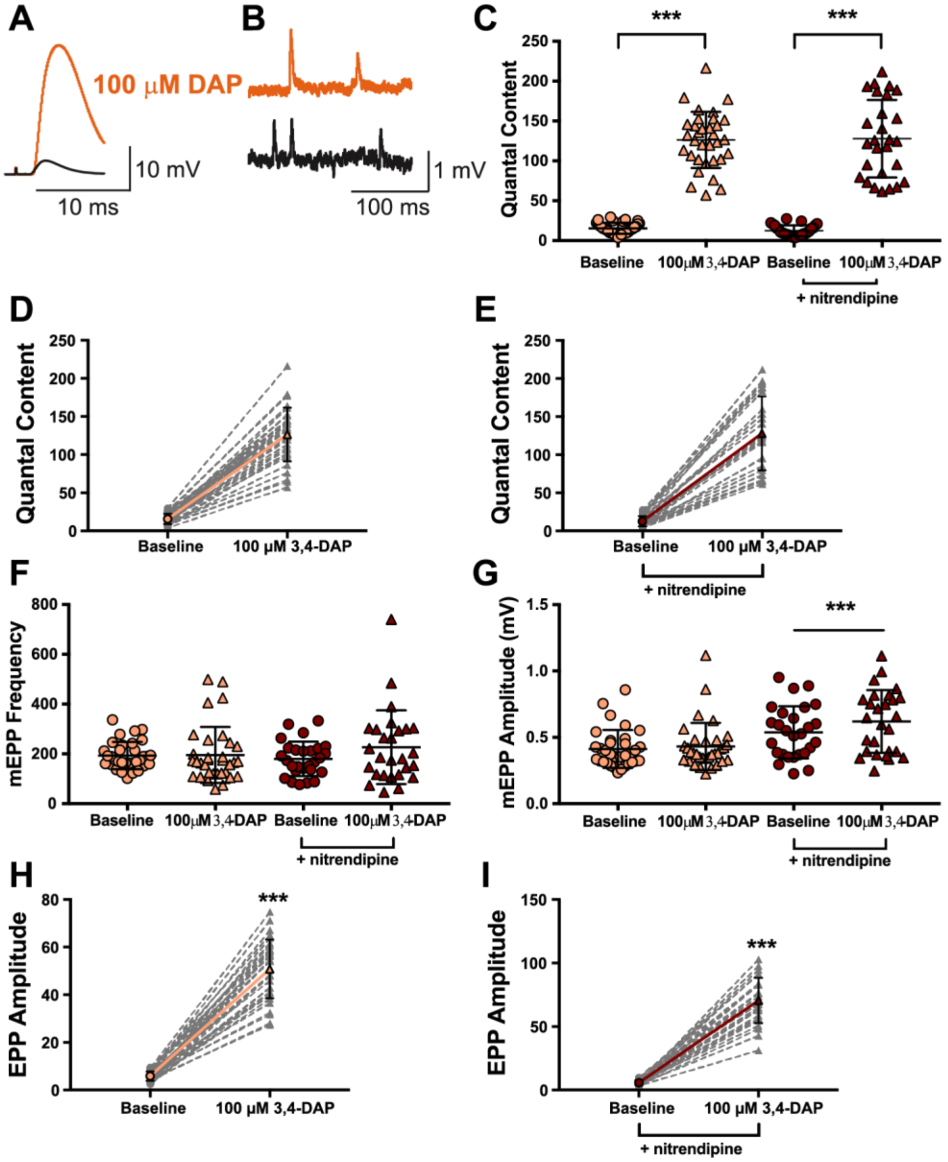

Figure 20 100 µM 3,4-DAP dose-dependently increases neuromuscular transmission independent of Cav1 channels in mouse neuromuscular junctions.

A-*B*, sample traces of electrophysiological recordings of EPPs (*A*) and mEPPs (*B*) before and after 100 µM 3,4-DAP application. *C*, quantified quantal content before (circles) or after (triangles) 100 µM 3,4-DAP application to vehicle (peach) or nitrendipine (red) -treated mouse NMJs. Two-way mixed ANOVA was used (there was a significant main effect of 100 µM 3,4-DAP (F (1, 58) = 548, *** $p < 0.0001$); no significant main effect of nitrendipine (F (1,58) = 0.01559, $p = 0.9011$) or interaction between 3,4-DAP x nitrendipine (F (1,58) = 0.2182, $p = 0.6421$); vehicle, $n = 33$; nitrendipine, $n = 27$). *D*-*E*, plots of individual paired values (grey dotted lines) with a superimposed average (solid peach line, vehicle; solid red line, nitrendipine). *F*, The 100 µM dose of 3,4-DAP did not alter mEPP frequency in the vehicle (peach) or nitrendipine (red) condition; two-way mixed ANOVA (no main effect of nitrendipine; F (1,58) = 0.1773, $p = 0.4209$, or 3,4-DAP; F (1,58) = 2.523, $p = 0.1176$, or significant interaction between 3,4-DAP x nitrendipine; F (1,58) = 2.051, $p = 0.1575$). *G*, There was a significant interaction between the effects of 100 μM 3,4-DAP and nitrendipine on mEPP amplitude (two-way mixed ANOVA: significant main effect of nitrendipine; F (1,58) = 10.91, $p = 0.0016$) and 3,4-DAP; F (1,58) = 19.03, $p < 0.0001$), and significant interaction between 3,4-DAP x nitrendipine; F (1,58) = 7.380, $p = 0.0087$)). Post-hoc simple main effect analysis showed a significantly altered mEPP amplitude in the nitrendipine (red, ***$p < 0.0001$) but not vehicle condition (peach, $p = 0.4497$). The 100 μM dose of 3,4-DAP increased EPP amplitude, shown as individual pairs (grey dotted lines) with a superimposed average (solid peach line, vehicle, *H*; solid red line, nitrendipine, *I*); Wilcoxon signed-rank test, *** $p < 0.0001$.

We next assessed whether nitrendipine could alter the effects of a supra-therapeutic concentration of 3,4-DAP (100 μM). After ω-agatoxin IVA treatment in the presence of nitrendipine, EPP amplitude averaged 5.7 ± 2.0 mV, mEPP amplitude averaged 0.5 ± 0.2 mV (Figure 20G, I) and this resulted in a quantal content of 12.5 ± 6.8 (Figure 20C, E). Bath application of 100 μM 3,4-DAP increased EPP amplitude by about 12.3-fold (70.5 ± 17.8 mV), and mEPP amplitude averaged 0.6 ± 0.2 mV (Figure 20G, I). Quantal content significantly increased to 127.8 ± 48.6 after application of 100 μM 3,4-DAP, or a 10.2-fold increase (Figure 20C, E). We did not observe a significant effect of nitrendipine on quantal content (Figure 20C) or mEPP frequency (vehicle: baseline = 193.2 ± 54.8, post-3,4-DAP = 195.6 ± 112.4; nitrendipine: baseline = 179.9 ± 69.4; post-3,4-DAP = 226.7 ± 148.1; values are number of events per 30 seconds; Figure 20F). However, we did observe a significant effect of 3,4-DAP on mEPP amplitude in the nitrendipine condition (Figure 20G).

We also tested the effect of 3,4-DAP at frog NMJs (a traditional model of neuromuscular function) in order to evaluate whether 3,4-DAP mechanisms of action are phylogenetically conserved, and determine if nitrendipine alters 3,4-DAP effects. We first assessed the effects of 1.5 μM 3,4-DAP on vehicle-treated frog NMJs (Figure 21). After exposure to ω-conotoxin GVIA, motor nerve stimulation evoked a mean baseline EPP amplitude of 3.7 ± 2.7 mV, and spontaneous release resulted in a mean mEPP amplitude of 0.8 ± 0.3 mV in vehicle-treated NMJs (Figure 21G-H), producing a quantal content of about 5 (QC = 4.8 ± 3.1; Figure 21C-D). After application of 1.5 μM 3,4-DAP, the mean EPP amplitude increased approximately 2-fold (to 7.6 ± 5.9 mV), without significantly altering mEPP amplitude (0.9 ± 0.4 mV; Figure 21G-H). Therefore, after exposure to 1.5 μM 3,4-DAP, quantal content increased to 8.8 ± 6.1 (a 1.8-fold increase; Figure 21C-D).

We next assessed 1.5 μM 3,4-DAP on frog NMJs in the presence of nitrendipine. After exposure to ω-conotoxin GVIA, the average baseline EPP amplitude was 1.3 ± 0.7 mV, the average mean mEPP amplitude was 0.5 ± 0.3 mV (Figure 21G, I), and quantal content was about 3 (QC = 3.2 ± 2.2; Figure 21C, E). After bath application of 1.5 μM 3,4-DAP, the mean EPP amplitude increased by about 2.3-fold to 3.0 ± 2.1 mV, with an average mEPP amplitude of 0.7 ± 0.3 mV (Figure 21G, I), which resulted in a quantal content of 6.0 ± 0.8 (a 1.9-fold increase; Figure 21C, E). We did not observe a significant effect of nitrendipine on quantal content (Figure 21C), though we did observe a significant difference in mEPP amplitudes in vehicle-treated versus nitrendipine-treated NMJs (Figure 21F-G). Neither 3,4-DAP nor nitrendipine altered mEPP frequency (vehicle: baseline = 61 ± 24.2, post-3,4-DAP = 57.4 ± 31.9; nitrendipine: baseline = 115.6 ± 125.3; post-3,4-DAP = 76.9 ± 69.3; values are number of events per 30 seconds).

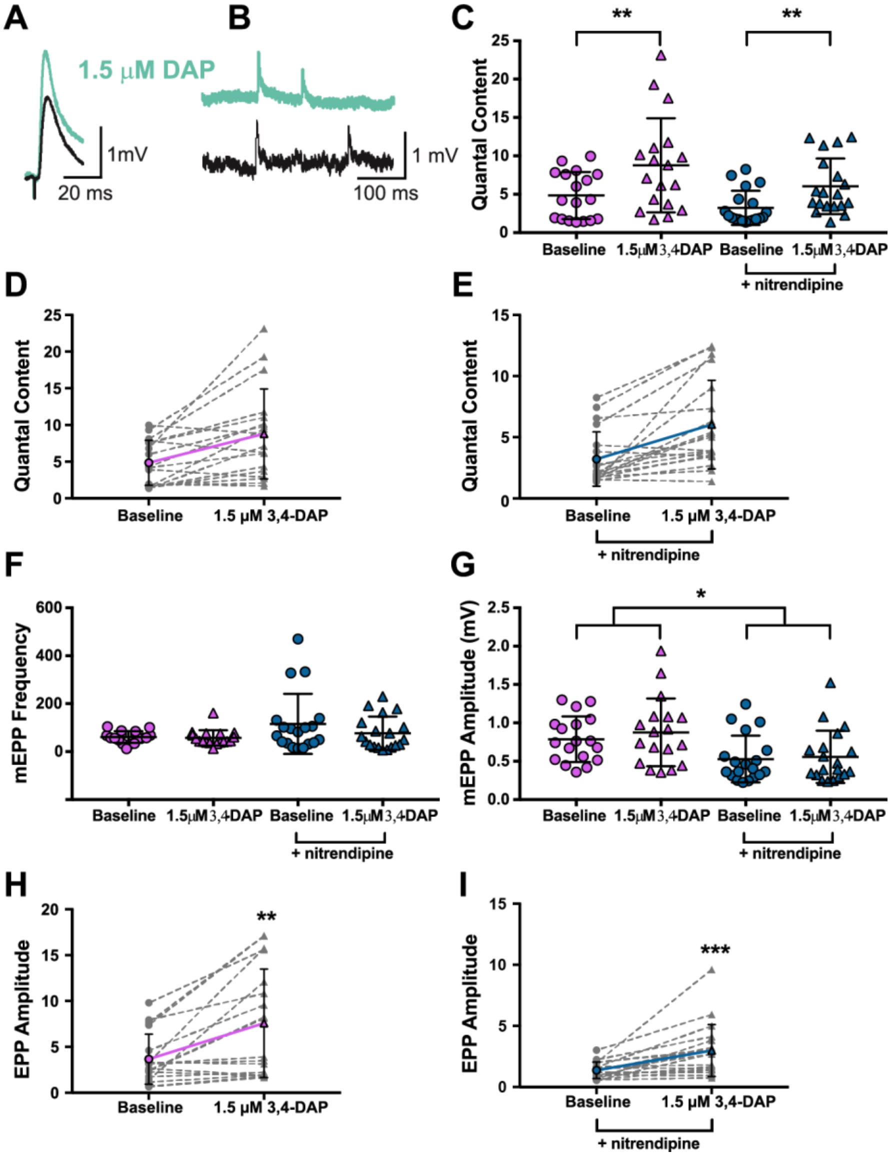

Figure 21 1.5 µM 3,4-DAP dose-dependently increases neuromuscular transmission independent of Cav1 channels in frog neuromuscular junctions.

A-*B*, sample traces of electrophysiological recordings of EPPs (*A*) and mEPPs (*B*) before and after 1.5 µM 3,4-DAP application. *C*, quantified quantal content before (circles) or after (triangles) 1.5 µM 3,4-DAP application to vehicle (pink) or nitrendipine (blue) -treated frog NMJs. Two-way mixed ANOVA was used (there was a significant main effect of 1.5 µM 3,4-DAP (F (1, 35) = 28.62, *** $p < 0.0001$); no significant main effect of nitrendipine (F (1,35) = 3.517, $p = 0.0691$) nor a significant interaction between 3,4-DAP x nitrendipine (F (1,35) = 0.785, $p = 0.3817$); vehicle, $n = 18$; nitrendipine $n = 19$). *D*-*E*, plots of individual paired values (grey dotted lines) with a superimposed average (solid pink line, vehicle; solid blue line, nitrendipine). *F*, The 1.5 µM dose of 3,4-DAP did not alter mEPP frequency in the vehicle (pink) or nitrendipine (blue) condition; two-way mixed ANOVA (no main effect of nitrendipine; F (1,35) = 2.856, *p* = 0.0999) or 3,4-DAP; F (1,35) = 3.418, *p* = 0.0729, nor a significant interaction between 3,4-DAP x nitrendipine; F (1,35) = 2.352, *p* = 0.1341). *G*, mEPP amplitude was significantly different between the vehicle (pink) and nitrendipine (blue) conditions, but was not affected by 3,4-DAP; two-way mixed ANOVA (significant main effect of nitrendipine (F (1,35) = 7.019, *p* = 0.0121), and there was no significant main effect of 3,4-DAP (F (1,35) = 2.604, *p* = 0.1156) nor significant interaction between 3,4-DAP x nitrendipine (F (1,35) = 0.6628, *p* = 0.4211)). *H-I*, The 1.5 μM dose of 3,4-DAP increased EPP amplitude, shown as individual pairs (grey dotted lines) with a superimposed average (solid pink line, vehicle, *H*; paired t test, ** p = 0.0012; solid blue line, nitrendipine, *I;* Wilcoxon signed-rank test, *** *p* < 0.0001).

Next, we assessed the effects of 100 μM 3,4-DAP on frog NMJs in the presence of vehicle (Figure 22). Before 3,4-DAP exposure, motor nerve stimulation produced an average EPP amplitude of 2.4 ± 1.2 mV, and spontaneous release resulted in an average mean mEPP amplitude of 0.7 ± 0.3 mV (Figure 22G), resulting in a quantal content of about 4 (QC = 3.8 ± 2.3; Figure 22C-D). After 100 μM 3,4-DAP treatment, the EPP amplitude increased to an average of 100.2 ± 36.5 mV (Figure 22H), and the mEPP amplitude was 0.9 ± 0.3 mV (Figure 22G). This resulted in a significant increase in quantal content to 142.6 ± 97.9 (a 37.5-fold increase; Figure 22C-D).

We subsequently assessed whether nitrendipine could modulate 100 μM 3,4-DAP effects on neurotransmission at frog NMJs. For these experiments, the average baseline EPP amplitude in the presence of nitrendipine was 2.3 ± 1.5 mV, with an average mEPP amplitude of 0.8 ± 0.2 mV (Figure 22G, I), resulting in a quantal content of about 3 (QC = 2.9 ± 1.8; Figure 22C, E). After bath application of 100 μM 3,4-DAP in the presence of nitrendipine, EPP amplitude increased to 59.6 ± 32.1 mV, the average mEPP amplitude was 0.9 ± 0.2 mV (Figure 22G), resulting in a quantal content of about 68 (QC = 67.8 ± 38.3, a 23.4-fold increase; Figure 22C, E). We did not observe an effect of nitrendipine on 3,4-DAP-induced changes in quantal content. Therefore, there was no significant difference between the effect of 100 μM 3,4-DAP in the absence or presence of nitrendipine (Figure 22C). However, we did find that 100 μM 3,4-DAP increased mEPP frequency regardless of vehicle or nitrendipine condition (vehicle: baseline = 46 ± 37.0, post-3,4-DAP = 73.9 ± 65.0; nitrendipine: baseline = 46.8 ± 23.8; post-3,4-DAP = 79.3 ± 45.4; values are number of events per 30 seconds; Figure 22F-G). Therefore, we found that 100 μM 3,4-DAP increased mEPP frequency and amplitude regardless of vehicle or nitrendipine condition.

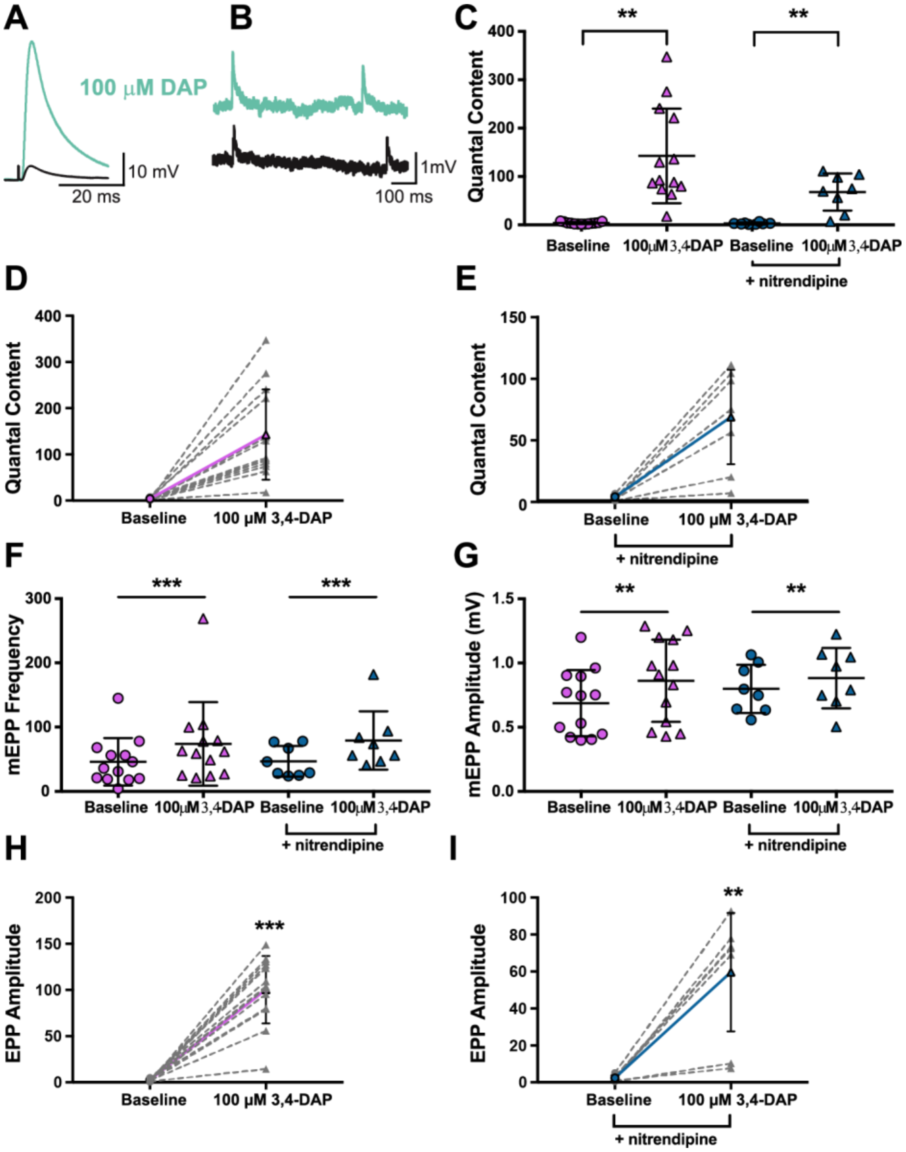

Figure 22 100 µM 3,4-DAP dose-dependently increases neuromuscular transmission independent of Cav1 channels in frog neuromuscular junctions.

A-B, sample traces of electrophysiological recordings of EPPs (*A*) and mEPPs (*B*) before and after 100 µM 3,4-DAP application. *C*, quantified quantal content before (circles) or after (triangles) 100 µM 3,4-DAP application to vehicle (pink) or nitrendipine (blue) -treated frog NMJs. Two-way mixed ANOVA was used (there was a significant main effect of 100 µM 3,4-DAP (F (1, 19) = 31.66, *** $p < 0.0001$; no significant main effect of nitrendipine (F (1,19) = 4.226, $p = 0.0538$) nor a significant interaction between 3,4-DAP x nitrendipine (F (1,19) = 4.162, $p = 0.0555$): vehicle, $n = 13$; nitrendipine $n = 8$). *D-E*, plots of individual paired values (grey dotted lines) with a superimposed average (solid pink line, vehicle; solid blue line, nitrendipine). *F*, The 100 µM dose of 3,4-DAP increased mEPP frequency in both the vehicle (pink) and nitrendipine (blue) conditions; two-way mixed ANOVA (significant main effect of 3,4-DAP; F (1,19) = 9.541, *p* = 0.006; no main effect of nitrendipine; F (1,19) = 0.0264, *p* = 0.8727) nor a significant interaction between 3,4-DAP x nitrendipine; F (1,19) = 0.0568, *p* = 0.8143). *G*, The 100 μM dose of 3,4-DAP significantly altered mEPP amplitude in both the vehicle (pink) and nitrendipine (blue) conditions; two-way mixed ANOVA (significant main effect of 3,4-DAP; F (1,19) = 11.88, *p* = 0.0027, but not nitrendipine; F (1,19) = 0.3468, *p* = 0.5628, and no significant interaction between 3,4-DAP x nitrendipine; F (1,19) = 1.436, *p* = 0.2454). *H-I*, The 100 μM dose of 3,4-DAP increased EPP amplitude, shown as individual pairs (grey dotted lines) with a superimposed average (solid pink line, vehicle, *H*; solid blue line, nitrendipine, *I*); paired t test, ** *p* = 0.0012, *** *p* < 0.0001.

These data, taken together with the effect of low micromolar concentrations of 3,4-DAP on Kv3 channels (Figure 15) and action potential waveforms (Figure 16), lead us to conclude that low micromolar concentrations of 3,4-DAP enhance the magnitude of AP-evoked transmitter release at mammalian NMJs by partial antagonist activity on Kv3 channels in the motor nerve terminal, which broaden the presynaptic action potential without directly affecting Cav1 channels. Furthermore, Cav1 channels do not significantly contribute to the effects on AP waveforms or quantal content at the NMJ of a higher concentration (100 μM) of 3,4-DAP.

3.3 Discussion

3,4-DAP is the FDA-approved first-line treatment for patients with Lambert-Eaton Myasthenic Syndrome (LEMS; (FDA, 2018, 2019; Voelker, 2019; Yoon et al., 2020)). Although 3,4-DAP is canonically thought to mediate its effects by partially blocking presynaptic voltage-gated potassium channels, a previous report that millimolar concentrations of 3,4-DAP could have off-target effects on Cav1 channels led to the question of whether 3,4-DAP mechanisms of action at therapeutic concentrations (estimated to be in the low micromolar range) involve Cav1 channels. For this reason, we sought to characterize the effects of 3,4-DAP on Kv3 potassium current, the presynaptic AP waveform, and transmitter release to determine if effects on AP waveforms and transmitter release were altered after using nitrendipine to block Cav1 (L-type) calcium channels. We found that the effects of 3,4-DAP on AP-evoked transmitter release at low micromolar concentrations could be explained by a partial block of Kv3 channels that results in the broadening of the presynaptic AP independent of any contribution from Cav1 calcium channels.

We did observe some small but significant effects of 3,4-DAP on mEPP frequency and amplitude, which may be due to as yet undetermined presynaptic and/or postsynaptic effects. It is possible that high doses of 3,4-DAP are not selective for presynaptic Kv3 channels, and affect postsynaptic Kv channels to indirectly modulate acetylcholine receptor sensitivity. In addition, the large amount of calcium influx into motor nerve terminals induced by 100 μM 3,4-DAP may alter normal homeostatic mechanisms of calcium buffering and handling, resulting in increased spontaneous vesicle release. While it is also unclear how nitrendipine might alter the effects of 3,4-DAP on mEPPs in mouse and frog NMJs, it is evident that the change in the magnitude of neurotransmission (quantal content) induced by 3,4-DAP is unaffected by Cav1 channels.

Previously, 4-aminopyridine has been reported to have IC_{50} values for blocking Kv3 channels of 30 μM – 2.5 mM (depending in the Kv subtype; (Castle et al., 1994; Grissmer et al., 1994; Luneau et al., 1991; Muqeem et al., 2018; Rettig et al., 1992; Schaarschmidt et al., 2009; Stephens et al., 1994; Vega-Saenz de Miera et al., 1992; Wu et al., 2009; Yokoyama et al., 1989)), and while 3,4-DAP effects on the squid giant axon potassium channel (SqKv1A; (Rosenthal, Vickery, & Gilly, 1996)) have been reported in the low micromolar range (Kirsch & Narahashi, 1978), we are not aware of any prior study characterizing the concentration-dependent effects of 3,4-DAP on the Kv3 subtype of potassium channels. While we found that 3,4-DAP could strongly inhibit Kv3 channels in the high micromolar to millimolar range with IC_{50} values of 150-250 μM (which we defined as low affinity binding), we remarkably discovered distinct high affinity effects of 3,4-DAP on Kv3 channels. We have shown that 3,4-DAP has similar effects on Kv3.3 and Kv3.4 and acts as a partial antagonist, binding in the low micromolar range (IC_{50} = 2.5-10 μM). In particular, Kv3.3 and Kv3.4 are both blocked by about 10% following exposure to the therapeutically relevant concentration of 1.5 μM 3,4-DAP. Thus, we predict that even a 10% decrease in Kv3.3 or Kv3.4 current would have a significant effect on the AP duration in motor nerve terminals.

Kv3 currents have been shown to mediate the dominant outward current during brief AP depolarizations within many nerve terminals (Alle, Kubota, & Geiger, 2011; Rowan et al., 2016; Rowan et al., 2014; Rowan & Christie, 2017), and have also been shown to have rapid activation and inactivation characteristics that enable nerve terminals to fire APs with short duration and at high frequency (Kaczmarek & Zhang, 2017; Rudy & McBain, 2001; Zemel et al., 2018). These data are consistent with the AP waveforms that were recently optically recorded from frog presynaptic nerve terminals (Ginebaugh et al., 2020). Here, we report concentration-dependent broadening of the presynaptic AP at the frog and mouse NMJ after exposure to 3,4-DAP. Even relatively small changes in presynaptic AP duration (15-20%) have been predicted to have significant effects on calcium ion entry and transmitter release (Ginebaugh et al., 2020). Thus, the roughly 20% broadening reported here at the mouse NMJ would be predicted to underlie the approximate 3-fold increase in transmitter release we observed (Ginebaugh et al., 2020). Interestingly, we found that 1.5 μM 3,4-DAP broadened the presynaptic AP waveform in the frog

NMJ to a greater extent that at the mouse NMJ. A potential species difference in presynaptic ion channel subtype expression and/or density may underlie these results and requires further investigation.

At neuromuscular synapses, the very brief presynaptic AP waveform only activates a small percentage of the Cav2 voltage-gated calcium channels positioned within transmitter release sites (Luo et al., 2015; Luo et al., 2011). This is thought to ensure that each of the hundreds of transmitter release sites within a single NMJ releases transmitter with low probability, conserving resources for repeated activation during normal activity (Tarr, Dittrich, & Meriney, 2013a). A brief AP activating only a small subset of available presynaptic Cav2 channels leads to neuromuscular weakness after many of these calcium channels are attacked and removed by autoantibodies in the disease LEMS. Mechanistically, 3,4-DAP is an effective symptomatic treatment for LEMS because the partial block of presynaptic Kv3 channels broadens the presynaptic AP, which increases the percentage of presynaptic voltage-gated calcium channels that open, and thus increases calcium entry and calcium-triggered transmitter release, leading to an improvement in neuromuscular strength in LEMS patients.

3.4 Experimental procedures

3.4.1 Ethics statement

The experimental procedures in this study were conducted in compliance with the US National Institutes of Health laboratory animal care guidelines and approved by the Institutional

Animal Care and Use Committee of the University of Pittsburgh. All efforts were made to minimize the suffering of animals.

3.4.2 Whole-cell perforated patch clamp electrophysiology

Recordings were performed as previously described (Wu et al., 2018a) using HEK293T cells transfected with either Kv3.3 (Kv 3.3 α subunit (Dr. Leonard Kaczmarek) and GFP at a DNA ratio of 1:1), Kv3.4 (Kv 3.4 α subunit (Dr. Manuel Covarrubias) and GFP at a DNA ratio of 1:1), Cav2.1 (Cav 2.1 α1 subunits, Addgene #26573; Cav β3, Addgene #26574; Cav $\alpha2\delta1$, Addgene #26575, and GFP at a DNA ratio of 1:1:1:1), or Cav1.2 (Cav 1.2 α1 subunits, Addgene #26572; Cav β3, Addgene #26574; Cav $\alpha2\delta1$, Addgene #26575, and GFP at a DNA ratio of 1:1:1:1). All recordings were performed at room temperature (20-22 °C).

For recording potassium currents, the pipette solution contained 70 mM CH_3KO_3S, 60 mM KCl, 10 mM HEPES, and 1 mM $MgCl_2$ at pH 7.4, and the bath saline contained 130 mM NaCl, 10 mM HEPES, 10 mM glucose, 3 mM $CaCl_2$, and 1 mM $MgCl_2$ at pH 7.4. For recording calcium currents, the pipette solution contained 70 mM CH_3O_3SCs, 60 mM CsCl, 10 mM HEPES, and 1 mM $MgCl_2$ at pH 7.4, and the bath saline contained 130 mM choline chloride, 10 mM HEPES, 10 mM TEA-Cl, 5 mM $BaCl_2$, and 1 mM $MgCl_2$ at pH 7.4. Patch pipettes were fabricated from borosilicate glass and pulled to a resistance of ~1-4 MΩ. Prior to each experiment, 3 mg amphotericin-B was dissolved in 50 μM DMSO. Each hour, 10 μl of this amphotericin-B stock was mixed with 500 μl of pipette solution and vortexed. Pipettes were filled in a two-step process. The tip of the pipette was dipped into a droplet of filtered pipette solution for 1 second, and then the remainder of the pipette was back-filled with the amphotericin-B/pipette solution mixture using a syringe and a 34 G quartz needle (MicroFil MF34G, World Precision Instruments, Sarasota, FL). This filled pipette was then used to make a GΩ seal with a fluorescent cell and 5-10 minutes was provided for amphotericin-B-mediated perforated patch access. Access resistances ranged from 5-15 MΩ and were compensated by 85%. Voltage clamp of cells under study was controlled by an Axopatch 200B amplifier driven by Clampex 10 software (Molecular Devices, Sunnyvale, CA). Data were filtered at 5 kHz, digitized at 10 or 50 kHz, and analyzed using Clampfit 10 software (Molecular Devices). Capacitive transients and passive membrane responses to the voltage steps were subtracted, and the liquid junction potential was corrected before each recording. Current through calcium or potassium channels was activated by depolarizing steps from a holding potential of -100 mV to +20 or +40 mV. In all cases currents were activated both before and after exposure to 3,4-DAP (dissolved in extracellular saline) in each cell, and current amplitudes were compared. For analysis before plotting, each current amplitude was normalized to its peak current amplitude before 3,4-DAP application to derive the normalized block at each concentration. The ratio described above was subtracted from 1 and the resulting value then was multiplied by 100 to obtain the percent inhibition.

3.4.3 Tissue preparation

Adult male and female frogs (*Rana pipiens*) were anaesthetized via immersion in 0.6% tricaine methane sulphonate, decapitated, and double pithed. The cutaneous pectoris neuromuscular preparation was dissected and bathed in normal frog Ringer saline (NFR, in mM: 116 NaCl, 10 mM BES buffer, 2 mM KCl, 5 mM glucose, 1 mM $MgCl_2$, 1.8 mM $CaCl_2$, pH 7.3). Adult male and female Swiss Webster mice (3-6 months of age; Charles River Laboratories, Wilmington, MA) were sacrificed using CO_2 inhalation, followed by thoracotomy. The epitrochleoanconeous neuromuscular preparation was bilaterally dissected and bathed in normal mouse Ringer saline (NMR, in mM: 150 NaCl, 10 mM BES buffer, 5 mM KCl, 11 mM glucose, 1 mM $MgCl_2$, 2 mM $CaCl_2$, pH 7.4).

3.4.4 Intracellular microelectrode electrophysiology

The muscle nerve was stimulated using a suction electrode and muscle contraction was blocked following a 1 hr incubation in a bath containing 50 μM of the irreversible muscle myosin inhibitor BHC (Heredia et al., 2016). After BHC washout using normal saline, microelectrode recordings were made in the presence of 1 μM nitrendipine (Sigma, St. Louis, MO) or the vehicle (0.01% DMSO) plus a selective muscle voltage-gated sodium channel blocker (1 μM μ-conotoxin PIIIA for the frog NMJ or 5 μM μ-conotoxin GIIIB for the mouse NMJ; Alomone Labs Ltd, Jerusalem, Israel). Additionally, in order to reduce the magnitude of transmitter released, 250-900 nM ω-conotoxin GVIA (to block N-type channels at the frog NMJ) or 50 – 100 nM ω-agatoxin IVA (to block P/Q-type channels at the mouse) was included in the recording bath. The range of concentrations listed was used iteratively with each preparation to reduce control endplate potentials (EPPs) to below 10 mV. Intracellular recordings of muscle cell membrane potentials were obtained using borosilicate glass microelectrodes pulled to a resistance of ~40-60 MΩ and filled with 3 M potassium chloride. For each muscle fiber recording made adjacent to visualized NMJs, spontaneous miniature synaptic events (mEPPs) were collected for 1-2 min, followed by 10-30 EPPs elicited by low frequency (0.2 Hz) stimulation. Subsequently, neuromuscular preparations were incubated in freshly made 1.5 μM or 100 μM 3,4-DAP for 30-60 minutes. After 3,4-DAP incubation, paired recordings were made from the same neuromuscular junctions that had been studied in control saline (resulting in paired data sets). Data were collected using an

Axoclamp 900A and digitized at 10 kHz for analysis using pClamp 10 software (Molecular Devices). Spontaneous and evoked endplate potentials were normalized to -70 mV and corrected for non-linear summation (McLachlan & Martin, 1981). We measured the magnitude of transmitter release by determining the quantal content (QC) using the direct method of dividing the peak of the averaged and normalized EPP trace by the peak of the averaged and normalized mEPP trace.

3.4.5 Voltage imaging

Voltage imaging was performed as described previously (Ginebaugh et al., 2020). To load nerve terminals with dye for the voltage-imaging procedure, a mixture of 5 mL of NFR (for frog preparations) or NMR (for mouse preparations) with a BeRST 1 voltage-sensitive dye (Huang et al., 2015) concentration of 0.5 μM and 10 μg/mL of Alexa Fluor 488-conjugated α-bungarotoxin (BTX; to counterstain postsynaptic receptors at the NMJ and block muscle contractions) was freshly made before each experiment. Then, the neuromuscular preparation was bathed in this dye mixture for 90 minutes, rinsed, and mounted on the stage of an Olympus BX61 microscope with a 60x water immersion objective. The nerve was then drawn into a suction electrode for supra-threshold stimulation. If the BTX conjugated to Alexa Fluor 488 did not completely block muscle contractions, 10 μM curare was added to the imaging saline to completely block any remaining nerve-evoked muscle contractions.

The postsynaptic BTX stain was used to identify nerve terminals and bring them into focus for voltage imaging. After locating a well-stained nerve terminal, an imaging region of interest (ROI) that contained a large portion of the nerve terminal branch (usually an ROI of approximately

80x30 µm for frog or 60x40 µm for mouse) was selected. All voltage imaging recordings were performed at room temperature (20-22 °C).

After a nerve terminal was selected for imaging, the presynaptic axon was stimulated at 0.2 Hz. During each stimulation, there was a brief 100 µs image collection window where the preparation was illuminated by a 640 nm laser (89 North laser diode illuminator) and the BeRST 1 dye fluorescence of the nerve terminal was recorded by an EMCCD camera (Pro-EM 512, Princeton Instruments). A custom routine on a Teensy 3.5 USB development board (PJRC) created a delay between the stimulation of the nerve and the triggering of the camera and laser. This delay in the 100 µs collection window was increased by 20 µs after each stimulation. After 100 sequential delays of 20 µs, a full time-course of 2 ms in which the entire AP waveform could be sampled was obtained (for 100 µM 3,4-DAP recordings, 300 moving bins for a total time course of 6 ms were used). For each frog nerve terminal recording, this process was repeated 5-15 times. For mouse nerve terminal recordings, this process was repeated 10-50 times (the BeRST 1 dye signal at the mouse terminals was weaker than at the frog terminals, and thus required more recordings to obtain a high-quality averaged AP waveform).

Custom written scripts in ImageJ and MATLAB (Mathworks) were used to analyze images. An "align slices in stack" ImageJ plugin (https://sites.google.com/site/qingzongtseng/template-matching-ij-plugin; see (Tseng et al., 2012; Tseng et al., 2011)) was used to correct the image stack for x-y drift. Then, an unbiased ROI selection (a subsection of the full imaging ROI) containing the nerve terminal was created by applying an Otsu local imaging threshold (Otsu, 1979) to the average fluorescence z-projection of the BeRST 1 image stack. The average fluorescence inside this ROI was used as the nerve signal (for frog recordings, 20 µm near the end of the nerve terminal and last node of Ranvier were excluded to restrict recordings to the middle electrical region of the terminal; see (Ginebaugh et al., 2020)). The average fluorescence from the region outside of the Otsu-selected ROI was used as the background signal. Both the nerve and background signals were then low-pass filtered offline (f_{pass}= 4 kHz). The following analysis was then performed separately for both the filtered and unfiltered signals: the background signal was divided from the nerve signal to generate a corrected fluorescence signal. We then fit a cubic B-spline through the unstimulated points in the fluorescence time course (the first and last 15 points of the 100 total points in each time series), and divided this cubic spline from each point in the fluorescence signal. This resulted in a ΔF/F fluorescence signal that did not fluctuate as a result of drift of the nerve muscle preparation or dye bleaching.

Two AP waveforms were then created by separately averaging the APs from the filtered and unfiltered ΔF/F fluorescence signal. The R^2 value between the filtered and unfiltered AP waveforms was then calculated. Since these are not linear models, the R^2 is not an exact measure of fit between the filtered and unfiltered AP waveforms, but rather is a metric of fit that is heavily weighted by the strength (in terms of the amplitude of the ΔF/F fluorescence signal) of the recorded signal. This weight is important because normalizing slight bumps on an almost flat signal could appear as an AP. Thus, the R^2 value provides a heuristic metric to estimate the quality of our recorded AP waveforms, and is not used for any statistical purposes.

Image artifacts in the background (e.g. a BeRST 1 dye-stained free-floating piece of connective tissue) occasionally resulted in the background not properly dividing the nerve signal, resulting in a noisier signal (and worse R^2 value). If the R^2 was less than 0.95 for frog recordings (or 0.90 for the 300 bin recordings for the 100 μM 3,4-DAP recordings), or 0.85 for the mouse recordings, the fluorescence of an approximately 15x30 μm section of the background near the nerve terminal was used as the background fluorescence rather than the complete background region. If this smaller background subsection also resulted in a R^2 value lower than the values listed above, the recording was not included in the data analysis. If the recording was of high enough quality to produce a sufficient R^2 value, the average filtered AP was normalized to the first 15 points (the baseline of the trace) and fit with cubic spline interpolation at an oversampled time resolution of 2 μs. Finally, the full width at half maximum (FWHM) of the normalized spline of the AP waveform was calculated.

3.4.6 Statistical analysis

Data was statistically analyzed using Prism v.7 or v.8 (Graphpad). Electrophysiology data were determined to be outliers if the data exceeded 1.5 times the interquartile range. The distribution of the data was assessed for normality using Shapiro-Wilk test. Statistical comparisons were performed using a two-way repeated measures mixed ANOVA with a between-subjects factor of bath (nitrendipine or control vehicle bath) and a within-subjects factor of 3,4-DAP (baseline or post 3,4-DAP bath application), or with a paired t test or Wilcoxon matched-pairs signed-rank test. If there was a significant interaction found, post-hoc simple effect tests were performed. Results were considered statistically significant when the *p*-value was < 0.05. The results represent the mean ± standard deviation (S.D.) of at least three independent experiments.

4.0 Development of a computational model of neuromuscular active zones in seropositive and seronegative Lambert-Eaton myasthenic syndrome predicts that a reduction in synaptotagmin can match known physiology in seronegative LEMS

Lambert-Eaton Myasthenic Syndrome (LEMS) is an autoimmune-mediated neuromuscular disease thought to be caused by autoantibodies against voltage-gated calcium channels (VGCCs) reducing the number of VGCCs in the presynaptic terminal of the neuromuscular junction (NMJ) and disrupting the organization of active zones (AZs; sites of transmitter release sites). However, up to 15% of LEMS patients are seronegative for antibodies against VGCCs. Furthermore, the specificity of these antibodies has been brought into question by multiple reports of antibodies against VGCCs in patients with other diseases but not LEMS, as well as healthy controls. Here, we construct a computational model of healthy mammalian NMJ AZs and then utilize this model to study LEMS-mediated effects on AZ organization and transmitter release. We show that healthy AZs can be modified to predict the transmitter release and short-term facilitation characteristics of LEMS by altering the AZs according to microscopy and electrophysiology data, and that disruption of AZ structure contributes more than the decrease in number of VGCCs to the LEMS-mediated reduction in transmitter release. We also show that seronegative LEMS can be caused by reducing the number of fast synaptotagmin proteins in healthy AZs, and that LEMS treatment with 3,4-diaminopyridine is less effective in this model. These results suggest that antibodies against AZ proteins may play an important role in seropositive LEMS in combination with anti-VGCC antibodies, antibody-mediated removal of synaptotagmin could cause seronegative LEMS, and an in-depth characterization of autoantibodies in LEMS patient serum will be crucial to understanding seropositive and seronegative LEMS.

4.1 Introduction

Lambert-Eaton Myasthenic Syndrome (LEMS) is an autoimmune-mediated neuromuscular disease that causes a reduction in synchronous neurotransmitter release from the presynaptic terminal of the neuromuscular junction (NMJ), which results in severe muscle weakness. The reduction of neurotransmitter release is typically ascribed to antibodies targeting the P/Q-type voltage gated calcium channels (VGCCs) that are primarily responsible for the calcium flux that triggers transmitter release in the active zones (AZs; the site of neurotransmitter release) of healthy mammalian NMJs. However, antibodies to VGCCs are not detected in 10-15% of LEMS patients (Kesner et al., 2018; Lennon et al., 1995; Motomura et al., 1997; Nakao et al., 2002; Takamori et al., 1995). These seronegative LEMS patients have similar clinical presentations to the seropositive LEMS patients that express the P/Q-type VGCC antibodies (Nakao et al., 2002; Oh et al., 2007). Although the seronegative LEMS patients do not produce antibodies to the P/Q-type VGCCs, the repeated injection of mice with seronegative LEMS patient serum is able to passively transfer LEMS symptoms to the mice, suggesting that seronegative LEMS is still antibody mediated (Nakao et al., 2002). These findings suggest that seronegative LEMS may be caused by antibodies targeting other proteins important to the release of neurotransmitter in the AZ.

Synaptotagmin-1 and synaptotagmin-2 are both found in the AZs of mouse NMJs (Pang et al., 2006a), and are known to be the calcium-sensing proteins responsible for fast synchronous release of neurotransmitter (Pang et al., 2006b). Antibodies to synaptotagmin-1 have been found in the serum of LEMS patients (Takamori, Komai, & Iwasa, 2000a; Takamori et al., 1995). Thus, it has been hypothesized that synaptotagmin antibodies could be responsible for seronegative LEMS. This hypothesis is supported by the finding that rats injected with synaptotagmin antibodies developed electrophysiological characteristics of LEMS (Takamori et al., 1994), experiments demonstrating that synaptotagmin-2 knock-out mice display similar electrophysiological characteristics to LEMS (Pang et al., 2006a), and a recent report of a rare genetic alteration of synaptotagmin-2 in human patients that causes symptoms similar to LEMS (Herrmann et al., 2014).

We have previously developed computational models of an AZ in the healthy frog NMJ (Dittrich et al., 2013; Ma et al., 2014), and have recently developed a preliminary model of AZs in the mouse NMJ (Laghaei et al., 2018). Here, we further develop our computational model of AZs in the healthy mouse NMJ, and then utilize it to investigate LEMS induced changes to the AZs. We find that rearranging the number and placement of VGCCs within our model of healthy mouse AZs is able to predict the electrophysiological behavior of LEMS, consistent with the hypothesized mechanism of seropositive LEMS. We then show that removal of a majority of the synaptotagmin-1-like fast calcium sensors produces similar results, providing computational evidence in support of the synaptotagmin-antibody hypothesis of seronegative LEMS. Finally, we test the impact of experimentally-recorded AP waveforms from mouse NMJs in the presence of 3,4-diaminopyridine (3,4-DAP) on our seronegative- and seropositive-LEMS computational AZ models, and hypothesize that the heterogeneity of antibodies in LEMS patients could be primarily responsible for the wide range of effectiveness of 3,4-DAP in the treatment of muscle weakness in LEMS patients.

4.2 Methods

4.2.1 Monte Carlo simulations

MCell version 3.4 (www.mcell.org) was used to study synchronous vesicle release at the mouse NMJ. MCell is a stochastic particle-based diffusion-reaction simulator that can model biological systems with arbitrarily complex 3D geometries (Bartol et al., 1991; Kerr et al., 2008; Stiles et al., 1996). For each simulation, 6000-10000 sperate MCell seeds were run. During each run, an AP (or a train of APs) caused VGCCs to open according to a Markov-chain ion channel gating scheme. Calcium was then released from open VGCCs and diffused into the terminal. As they diffused, the calcium ions either bound to calcium sensors located on synaptic vesicles or to calcium buffer molecules evenly distributed throughout the terminal. Our models are based on previously developed MCell models of the frog AZ (Dittrich et al., 2013; Ma et al., 2014) and a recently developed preliminary model of mouse AZs (Laghaei et al., 2018). We then further constrained these models with new biophysical parameters from literature.

4.2.2 Action potentials and VGCCs

To constrain our model to biological data, we used AP waveform inputs based on recently published AP waveforms recorded from the mouse NMJ via voltage-imaging (chapter 3.0). We used the average AP waveforms from both control and 3,4-DAP recordings, and prepared them for use in our simulations similarly to previously described (Ginebaugh et al., 2020). In brief, the average AP waveforms were normalized to a peak voltage of 30 mV and a resting potential of -60 mV. We then removed fluctuations caused by noise in the experimental data in the onset of the rising edge of each of the AP waveforms by replacing the first 10% of the rising edge with a line that had the same slope as the next 10% of the rising edge. We then removed fluctuations in the falling edge of each AP waveform by fitting a second-degree polynomial through the last 30% of the falling edge and then replacing that 30% with the polynomial (Figure 23 A and B).

The kinetics of the VGCCs were based on the Markov-chain model used in our excess-calcium-binding-site model of the frog NMJ (Dittrich et al., 2013), which consisted of three closed states and one open state. However, because the previously published model was based on the frog which uses primarily N-type VGCCs, whereas the mouse uses primarily P/Q-type VGCCs and because prior research has shown that VGCC gating is best fit by a model with two open states (DeStefino et al., 2010), we altered the previous VGCC gating scheme to contain two open states and reparametrized it to fit the average calcium currents from previously-published recordings from HEK293 cells expressing P/Q type VGCCs (Tarr et al., 2014) (Figure 23 C and D). The rate constants α, β, and k were the same as used in previous models (Dittrich et al., 2013; Ma et al., 2014) except the reversal potential for calcium used in the calculation of k was +60 mV rather than the +50 mV value that was used in those previous models (Campbell, Giles, & Shibata, 1988).

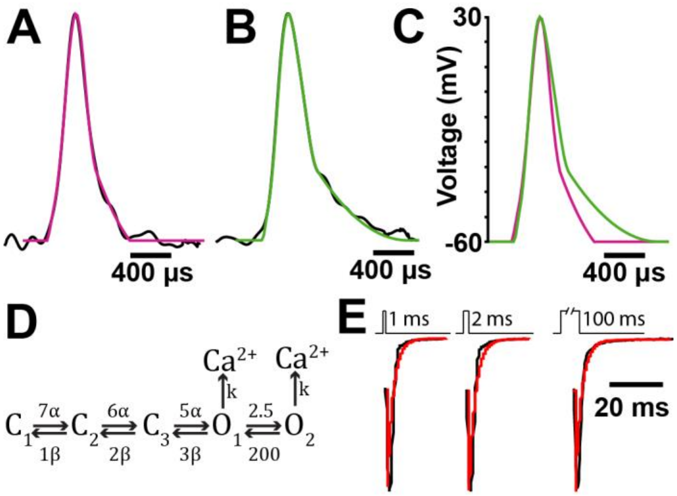

Figure 23 AP waveforms and VGCC kinetics in the MCell models.

A: The normalized average of AP waveforms recorded from mouse NMJs (black) and the computational AP waveform used in MCell simulations (magenta). *B*: The normalized average of AP waveforms recorded from mouse NMJs in the presence of 1.5 μM 3,4-DAP (black) and the computational AP waveform used to simulate 3,4-DAP in MCell (green). *C*: A comparison of the computational AP waveforms used in control (magenta) and 3,4-DAP (green) simulations. *D*: The Markov-chain ion channel gating scheme used to determine the behavior of VGCCs in our simulation. *E*: Model output of calcium current (red) overlaid onto experimental data (black) from the average trace of 6 recordings from P/Q-type VGCCs expressed in HEK293 cells. The voltage steps used to activate the currents are shown above each set of traces. Average AP waveforms in A and B are from (Ginebaugh et al., 2020). Patch clamp recordings of P/Q-type VGCCs expressed in HEK293 cells are from (Tarr et al., 2014).

4.2.3 Mouse MCell model and vesicle fusion

To construct an MCell model of mouse NMJ AZs, the NMJ ultrastructure and placement of the AZs was the same as previously described in our preliminary mouse model (Laghaei et al., 2018). The healthy mouse model consisted of six AZs placed 500 nm apart, and each AZ contained two docked synaptic vesicles (Figure 24A).

The vesicle fusion mechanism was similar to our previously described mechanism (Ma et al., 2014). In brief, the bottom of each vesicle contained two different types of calcium sensors. The first type was a fast sensor which represents synaptotagmin-1 (syt1) or synaptotagmin-2 (syt2). The second was a slow second-sensor binding site. Since the publication the NMJ AZ model that contained a second-sensor binding site (Ma et al., 2014), it was revealed that this second sensor is likely to be synaptotagmin-7 (syt7) (Jackman et al., 2016). Thus, to be more consistent with the literature, we altered the calcium binding on- and off-rates of both the syt1-like and syt7-like sensors based on a previous simulation of phospholipid binding of both sty1 and syt7 (Jackman & Regehr, 2017). The calcium binding rates for the syt1-like sensor were set to $k_{on} = 2.2 * 10^7\ M^{-1}s^{-1}$ and $k_{off} = 910\ s^{-1}$, and the calcium binding rates for the syt7-like sensor were set to $k_{on} = 1 * 10^7\ M^{-1}s^{-1}$ and $k_{off} = 15\ s^{-1}$.

When bound by a sufficient number of calcium ions, the calcium sensors were considered activated and contributed to increasing the probability of vesicular fusion. Vesicles fuse in a probabilistic manner, with fusion for each vesicle determined with the Metropolis-Hastings sampling protocol (Hastings, 1970; Metropolis et al., 1953) using the probability $P = min\left(exp\left(-\frac{E_b - n_{S1} \cdot \Delta E_{S1} - n_{S7} \cdot \Delta E_{S7}}{k_B T}\right), 1\right)$. Here, $E_b = 40\ k_BT$ is the free energy barrier preventing vesicle release (Li et al., 2007; Martens et al., 2007), n_{S1} and n_{S7} are the number of syt1-like sensors and syt7-like sensors that have been activated by calcium, and ΔE_{S1} and ΔE_{S7} are the amount each active calcium sensor contributes to overcoming the 40 k_BT free energy barrier.

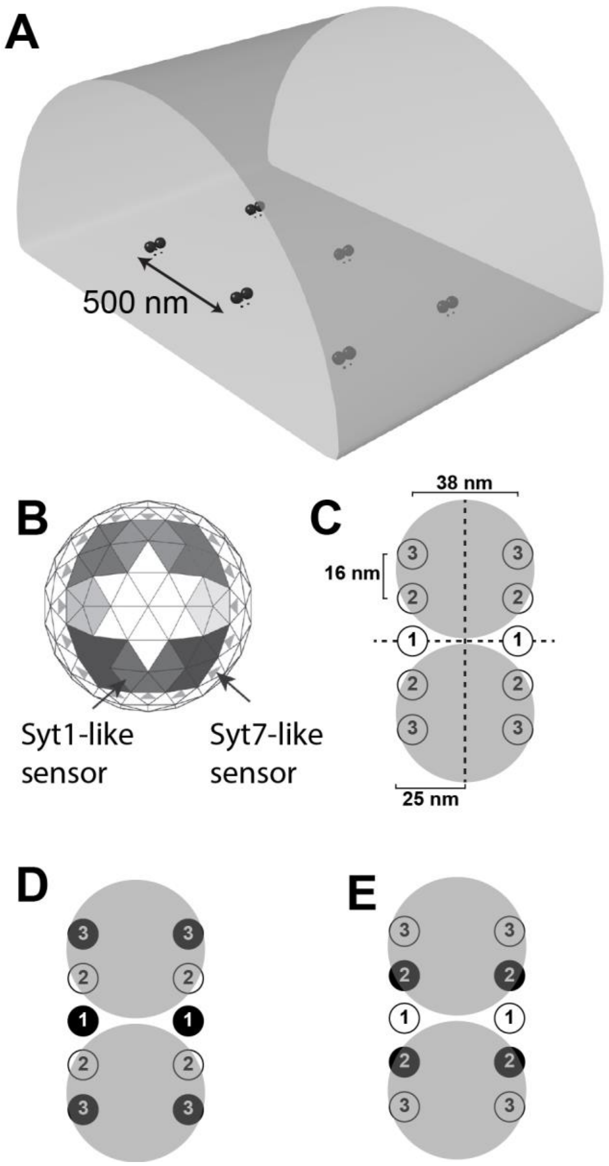

Figure 24 Diagrams of the healthy mouse AZ MCell model and VGCC placement parameter sweep.

A: Visualization of the geometry of the health mouse AZ MCell model. Six AZs are modeled and each AZ consists of VGCCs (small black dots) and two docked synaptic vesicles (black spheres). *B:* A diagram of the calcium sensors on the underside of each synaptic vesicle. Each vesicle has up to 8 syt1-like sensors, consisting of 5 binding sites each. A syt1-like sensor is activated when at least two of its 5 sites are bound to calcium. Each vesicle also has 16 syt7-sensors, positioned in a single annulus around the outside of the syt1-like sensors. Each syt-7 like sensors only contain one calcium-binding site, and are activated when the site is bound by a calcium ion. Adapted from (Laghaei et al., 2018). *C*: A schematic of the AZ from above, showing the possible placement positions for VGCCs based on freeze-fracture data. The schematic shows two docked synaptic vesicles (grey translucent circles) with a row of 5

VGCCs placed on each side (numbered circles). The VGCC placement must be symmetrical over both the x and y axes (dotted lines), resulting in only 3 different positions which may be selected for VGCCs placement (i.e., a selection of position 3 requires all four of the VGCCs labeled 3 to be selected). *D*: An example of a 6 VGCC AZ model created by selecting positions 1 and 3 to contain VGCCs. *E*: The 4 VGCC AZ model, created by selecting position 2 to contain VGCCs, which best predicted experimental results.

4.3 Results

4.3.1 Constraining the healthy mouse AZ model

Our MCell model of the healthy mouse AZ was initially based on previous MCell models of the frog AZ (Dittrich et al., 2013; Ma et al., 2014), a preliminary model of the mouse AZ (Laghaei et al., 2018), and experimental and biophysical data (see section 4.2). The only free parameters in our model were the number and location of VGCCs as well as the number and energy contribution of the syt1-like and syt7-like calcium binding sites toward overcoming the 40 k_BT free energy barrier for synaptic vesicle fusion. We constrained the number of syt1-like sensors to between 5 and 8 based on based our previous model (Ma et al., 2014) and the geometrical arrangement of 5 to 8 syntaxin that helps form the fusion pore (Han et al., 2004). Based on biophysics literature, we constrained the energy contribution of calcium-activated syt1-like sensors toward overcoming the 40 k_BT free energy barrier for vesicle fusion to be either 18 k_BT (Gruget et al., 2020; Gruget et al., 2018) or 20 k_BT (Martens et al., 2007). Although much has been learned about synaptotagmin-7 since its discovery as an important calcium sensor in neurotransmitter release (Jackman et al., 2016), much is still unknown. Thus, we decided to keep the number of syt7-like binding sites at 16 as was used in our previous model (Ma et al., 2014) due to the ability of this model to fit experimental data, since this aspect of syt7 stoichiometry remains unknown (Figure 24B). Based on computational predictions that the energy contribution of syt7 is lower than syt1 (Jackman & Regehr, 2017), as well as our previous model (Ma et al., 2014), we allowed the syt7-like contribution to vesicle fusion energy to be any positive integer less than or equal to 11.

To constrain the number of possible placements for the VGCCs, we assumed that VGCCs must be represented by the double rows of intramembranous particles on each side of the vesicles seen in freeze-fracture electron microscopy, and constrained the placement of the VGCCs to the average measured placement of these particles in freeze-fracture electron microscopy replicas (Fukuoka et al., 1987). Based on the rapid release of neurotransmitter during an AP, and the known close association of P/Q-type VGCCs with various AZ proteins (Catterall, 1999; Kaeser et al., 2011; Mochida et al., 2003; Sheng et al., 1998), we constrained the placement of VGCCs to the first row of the double rows on each side of the AZ. Although this narrowed the placement of VGCCs to 10 possible locations, this still created $2^{10}-1 = 1023$ different possible placement combinations for VGCCs. To further narrow down the possible VGCC configurations, we constrained the placement of VGCCs in the AZ to be symmetrical across both the vertical and horizontal midline of the AZ. This results in only three different locations for VGCC placement, resulting in only 7 different possible VGCC-placement configurations (Figure 24C).

With these constraints, we performed a parameter sweep of VGCC placement combinations and synaptotagmin-like sensor number and energy contributions to find model conditions which best fit experimental data (Table 1). We found that two possible 6-channel models (Figure 24D) with 5 syt1-like sensors, 18 k_BT energy contribution of activated syt1-like sensors, and no syt7-like energy contribution (i.e. the synaptotagmin parameters that would cause the fewest number of vesicles to be released) resulted in a probability of release per active zone (Pr_{AZ}) higher than the experimentally calculated value of 0.22 Pr_{AZ} (Laghaei et al., 2018) (Table 1). Similarly, we found that the 2-channel model with 8 syt1-like sensors, 20 k_BT syt1-like energy contribution, and 11 syt7-like energy contribution (i.e., the synaptotagmin parameters that would cause the greatest number of vesicles to fuse) resulted in a Pr_{AZ} lower than the experimental value. Thus, only the two possible four-VGCC placements remained as plausible organizations for our AZ model.

To determine which of these VGCC placements and synaptotagmin parameters best fit experimental results, we first ran a parameter sweep to find all combinations of synaptotagmin parameters that would predict the experimental Pr_{AZ} value of 0.22. We then investigated the ability of these parameters to fit the experimental paired pulse facilitation (PPF) results (Table 1). We found that the 4-VGCC model with VGCCs in position 2 (Figure 24E) best predicted the experimental PrAZ and PPF (Table 1). This model also accurately predicted a slight depression over short trains of stimuli (Figure 25A), a paired pulse facilitation that is relatively unchanged by changes in inter-spike interval (Figure 25B), and a vesicle release latency following an AP (Figure 25C) that is in agreement with previously published experimental data (Wang, Pinter, & Rich, 2010). In addition, our model predicted a log-log ratio between extracellular calcium and transmitter release (also known as the calcium-release ratio, or CRR; Figure 25D) of ~2.7, which is consistent with experimental data (Urbano et al., 2003). Thus, this model that resulted from our evaluation of VGCC placement closely recapitulates experimental results for a variety of experiments. Our model places VGCCs only ~15 nm away from the nearest synaptic vesicle (and the calcium sensors attached to it), which is similar to the estimated distance between VGCCs and calcium sensors in fast-spiking hippocampal GABAergic interneurons (Arai & Jonas, 2014;

Bucurenciu et al., 2008) and the mature calyx of Held (Chen et al., 2015; Nakamura et al., 2015). Thus, our VGCC placement agrees with the hypothesis that VGCCs are tightly coupled to docked synaptic vesicles in the NMJ to mediate fast synchronous transmitter release (Stanley, 2016).

Table 1 Parameter sweep of VGCC configuration and calcium-sensor settings.

#VGCCs	VGCC position(s)	n_{S1}	ΔE_{S1}	ΔE_{S7}	Pr_{AZ}	PPF P2/P1	PPF P3/P1
6	1,3	5	18	0	0.251	0.828	0.742
6	1,2	5	18	0	0.271	0.813	0.691
2	1	8	20	11	0.161	0.982	0.941
4	2	5	18	7	0.200	1.014	0.981
4	**2**	**5**	**18**	**8**	**0.228**	**1.009**	**0.952**
4	2	5	18	9	0.241	1.015	0.949
4	2	5	20	6	0.203	0.993	0.949
4	2	5	20	7	0.228	0.992	0.940
4	2	5	20	8	0.242	1.002	0.933
4	2	6	18	4	0.205	0.918	0.862
4	2	6	18	5	0.214	0.945	0.897
4	2	6	18	6	0.224	0.962	0.905
4	3	5	18	8	0.207	0.993	0.955
4	3	5	18	10	0.222	0.988	0.922

#VGCCs, number of VGCCs in the model; VGCC position(s), position of VGCCs based on Figure 24; n_{S1}, number of syt1-like sensors; ΔE_{S1}, energy contribution toward fusion of activated syt1-like sensors; ΔE_{S7}, energy contribution toward fusion of syt7-like sensors; Pr_{AZ}, probability of release per AZ; PPF, paired pulse facilitation for the second or third pulse (P2,P3) compared to the first pulse (P1). Values in bold show the model which best matches experimental conditions (Pr_{AZ} =0.22, PPF P2/P1= 1.01, PPF P3/P1 = 0.94).

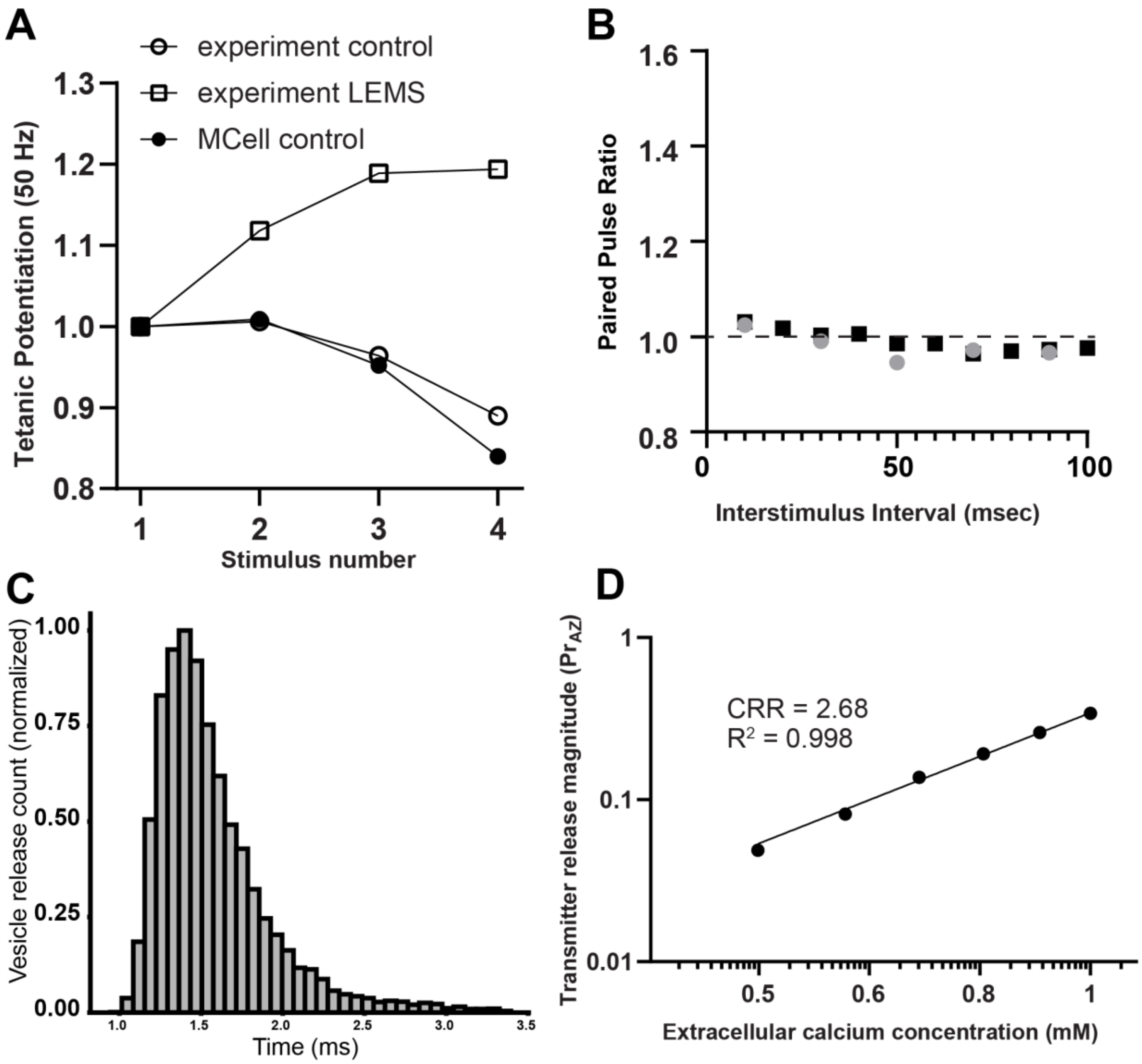

Figure 25 Validation of the healthy mouse AZ MCell model.

A: Plot of tetanic potentiation at 50 Hz. Our MCell model of the healthy mouse AZs (black circles) closely matched experimental results (open circles). The tetanic potentiation seen in LEMS-model mice (open squares) is added for comparison. Experimental results for both LEMS and control tetanic potentiation from (Tarr et al., 2013b). *B*: The paired pulse ratio measured as the interstimulus interval is changed from 10 to 90 msec. The outputs from the MCell model (grey circles) and the experimental data (black squares) both predict little change over a changing interstimulus interval. Experimental data from (Laghaei et al., 2018) *C*: Plot of changes in transmitter release magnitude in our MCell model as the extracellular calcium concentration was varied. The log-log best fit line for the data is shown with a slope of 2.69 and an R^2 value of 0.998. *D*: The predicted latency of vesicle release following a single presynaptic AP is plotted based on our MCell model.

4.3.2 Constructing a MCell model of LEMS-modified AZs

We sought to create a MCell model which would fit the experimental electrophysiological characteristics seen in LEMS-model mice by altering our model of healthy mouse AZs. We altered our model of healthy mouse AZs based on the experimental evidence that LEMS (1) reduces the number of P/Q-type VGCCs in the AZs (Smith et al., 1995; Xu et al., 1998), (2) causes a compensatory upregulation of other VGCC subtypes (primarily L-type) outside of the AZs (Flink & Atchison, 2002; Xu et al., 1998), (3) reduces the number of AZs, (Fukunaga et al., 1982; Fukunaga et al., 1983) and (4) disrupts the organization of particles in many of the remaining AZs (Fukuoka et al., 1987). The experimental results we sought to predict with our model were: a 60-75% reduction in quantal content compared to healthy control mice, an increase in facilitation over short trains of stimuli, (Lang et al., 1984; Lang et al., 1983; Tarr et al., 2014; Tarr et al., 2013b), and a large portion of transmitter release being attributed to VGCCs located outside of the AZs (Flink, 2003; Flink & Atchison, 2002; Giovannini et al., 2002).

Since LEMS both decreases the number of P/Q-type VGCCs and increases the number of L-type VGCCs, we decided to begin creating our MCell model of LEMS-modified AZs by first constructing a model of P/Q-type-VGCC-only LEMS-modified AZs without any compensatory upregulation of L-type VGCCs. Experiments measuring quantal release in LEMS-model mice before and after exposure to the L-type VGCC blocker nimodipine revealed that blocking L-type VGCCs in LEMS-model mice reduces transmitter release ~40% compared to LEMS-model mice without the channel blocker (Flink & Atchison, 2002). Since LEMS-model mice have a 60-75% reduction of transmitter release compared to controls, and blocking L-type VGCCs further decreases the transmitter release of LEMS-model mice by ~40%, LEMS-model mice with blocked L-type calcium currents are expected to release 76-85% less transmitter release than healthy controls. Thus, to fit experimental data, a model of LEMS AZs with only P/Q-type VGCCs should have 76-85% less quantal release than the healthy control AZ model.

Perineural recordings of calcium currents at the NMJs of *ex vivo* nerve-muscle perpetrations from healthy and LEMS-model mice indicate that calcium current from P/Q-type VGCCs is only reduced by about 30-40% in LEMS-model mice (Smith et al., 1995; Xu et al., 1998). We found that randomly removing ~40% (9 out of 24) of the VGCCs only reduced transmitter release by 42%. This is a less than the 60-75% reduction of transmitter release seen in LEMS-model mice, and is much less than the 76-85% reduction in transmitter release seen in LEMS-model mice with blocked L-type calcium current (Flink & Atchison, 2002). We found that in order to reduce transmitter release to 22% compared to control by randomly removing VGCCs, it was necessary to remove 75% (18 out of 24) of the VGCCs. This results in a much greater reduction in calcium current than the experimentally measured value of a 30-40% reduction (Smith et al., 1995; Xu et al., 1998). These results suggest that simply removing VGCCs is not sufficient to explain the effect of LEMS on transmitter release.

Not only does LEMS reduce the current through P/Q-type VGCCs, but freeze-fracture electron microscopy reveals that LEMS also disrupts the normally well-organized structure of the AZs and reduces the number of well-organized AZs by 70-85% (Fukunaga et al., 1982; Fukunaga et al., 1983; Fukuoka et al., 1987). These studies also found that LEMS causes a large number of clusters of intramembranous particles (which are likely highly unorganized AZs (Fukuoka et al., 1987)) to appear, and to outnumber the remaining well-organized AZs. Thus, we investigated the impact of structural disorganization of the AZs in our model by moving the VGCCs way from the AZs. We found that by simply moving the VGCCs 20 nm away from the synaptic vesicles in the AZ (Figure 26A) we were able to reduce transmitter release by 61%. This suggests that the disorganization of the AZs structure plays an essential role in determining the reduced magnitude of transmitter release seen in LEMS.

Thus, to create our LEMS MCell model, we first altered our 6 AZ healthy mouse model by removing 2 AZs and denoting the remaining 4 AZs as 1 “normal” AZ with unaltered P/Q-type VGCC locations (Figure 24E) and 3 “clusters” with the P/Q-type VGCCs moved an additional 20 nm away from the AZ (Figure 26A). We then randomly removed 6 of the 16 remaining VGCCs to simulate the 30-40% reduction in P/Q-type calcium current (assuming that all VGCCs are equally likely to be removed by anti-VGCC antibodies, and that the VGCCs from the two otherwise destroyed AZs remain in the presynaptic terminal). We found that this P/Q-type-only LEMS model resulted in an 80% reduction in transmitter release compared to control, which is a good fit for the experimentally measured values of transmitter release recorded from LEMS-model mice in the presence of drugs to block L-type VGCCs (Flink & Atchison, 2002).

Having successfully constructed an MCell model of P/Q-type-only LEMS-modified AZs, we next sought to add in L-type VGCCs to construct a more complete model of LEMS with both P/Q- and L-type VGCCs. Although it is known that L-type VGCCs are upregulated in LEMS and contribute to transmitter release, little is known about their number and location relative to the AZs. However, it is thought that they do not localize with the AZs because they lack the necessary synaptic protein interaction site (Catterall, 1999; Mochida et al., 2003; Sheng et al., 1998). Furthermore, buffer experiments have shown that the contribution of L-type VGCCs to transmitter release in LEMS is blocked by low concentrations of fast calcium buffer, placing them outside of the AZ (Flink, 2003). To model this increase in L-type current and its effect on transmitter release, we simply placed another row of 2 VGCCs on each side of the AZ an additional 55 nm beyond the first rows of VGCCs in our P/Q-type-only LEMS model (Figure 26A). In our MCell models, we use the same channel gating scheme (Figure 23D) for all VGCCs, but for simplicity we will herein refer to VGCCs in our model placed inside the AZs as P/Q-type and VGCCs placed further outside the AZs as L-type. We also did not randomly remove a proportion of the L-type VGCCs as we did with P/Q-type VGCCs. We found that the addition of L-type VGCCs to our P/Q-type-only LEMS model increased transmitter release from an 80% reduction to a 65% reduction when compared with controls. This 65% reduction is within the range of experimentally measured reductions in quantal content in LEMS. The addition of L-type VGCCs also increased the facilitation over short trains of stimuli to levels seen in experimental data from LEMS-model mice (Figure 26B). These results show that we were able to alter our MCell model of the healthy mouse AZs to predict the electrophysiology observed in LEMS by reducing the number of AZs and altering the number and location of VGCCs within the remaining AZs.

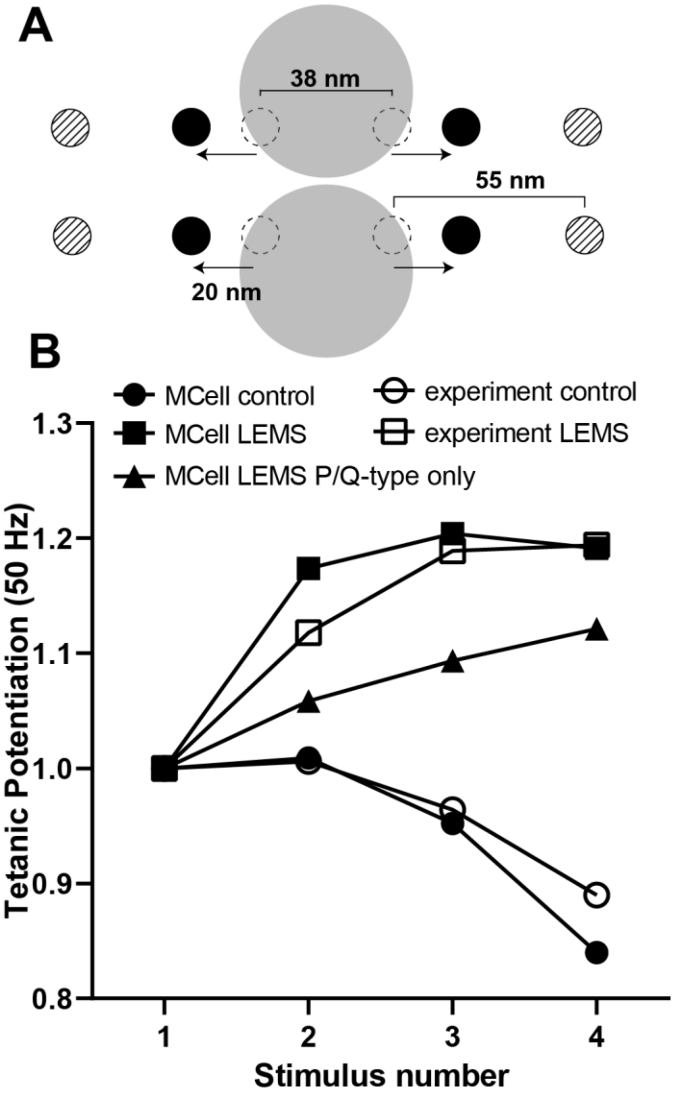

Figure 26 The seropositive LEMS MCell model.

A: A diagram of the AZ in the MCell model, showing the location of vesicles (grey circles) P/Q-type VGCCs in "normal" MCell model AZs (dashed circles), the location of P/Q-VGCCs in "cluster" MCell model AZs (black circles), and the location of L-type VGCCs in both the "normal" and "cluster" LEMS MCell model AZs (circles with lines through them). Diagram is to scale except for the size of the VGCCs. *B:* Plot of tetanic potentiation at 50 Hz. Our model predicts that moving P/Q-type VGCCs and randomly removing some P/Q-type VGCCs (black triangles) increases tetanic potentiation, but not to the experimentally measured value of LEMS-model mice (open squares). The addition of L-type VGCCs to our MCell model (black squares) increases the predicted tetanic potentiation to levels consistent with experimental results. Experimental results from (Tarr et al., 2013b).

4.3.3 Loss of fast-synaptotagmin-like sensors produces similar results to LEMS-model AZs

We next wanted to investigate the nature of seronegative LEMS by attempting to alter our healthy mouse AZ MCell model to predict the electrophysiological behavior of LEMS, but without altering the number or location of VGCCs. Based on reports of seronegative LEMS patients producing antibodies to syt1, we hypothesized that reducing the number of fast syt1-like calcium sensors on our healthy mouse model would also be able to predict the electrophysiological properties of LEMS-model mice NMJs. We expected that reducing the number of syt1-like sensors would reduce the magnitude of transmitter release. In addition, reducing the number of syt1-like sensors would increase the reliance on the syt7-like sensors for release, which we hypothesized would produce the increased facilitation over short trains of stimuli seen in LEMS. Indeed, we found that transmitter release decreased and short-term facilitation increased relative to the number of syt1-like sensors removed (Figure 27). These results suggest that antibodies against synaptotagmin-1 and synaptotagmin-2 may be sufficient to cause LEMS-like effects on transmitter release in the absence of anti-VGCC antibodies.

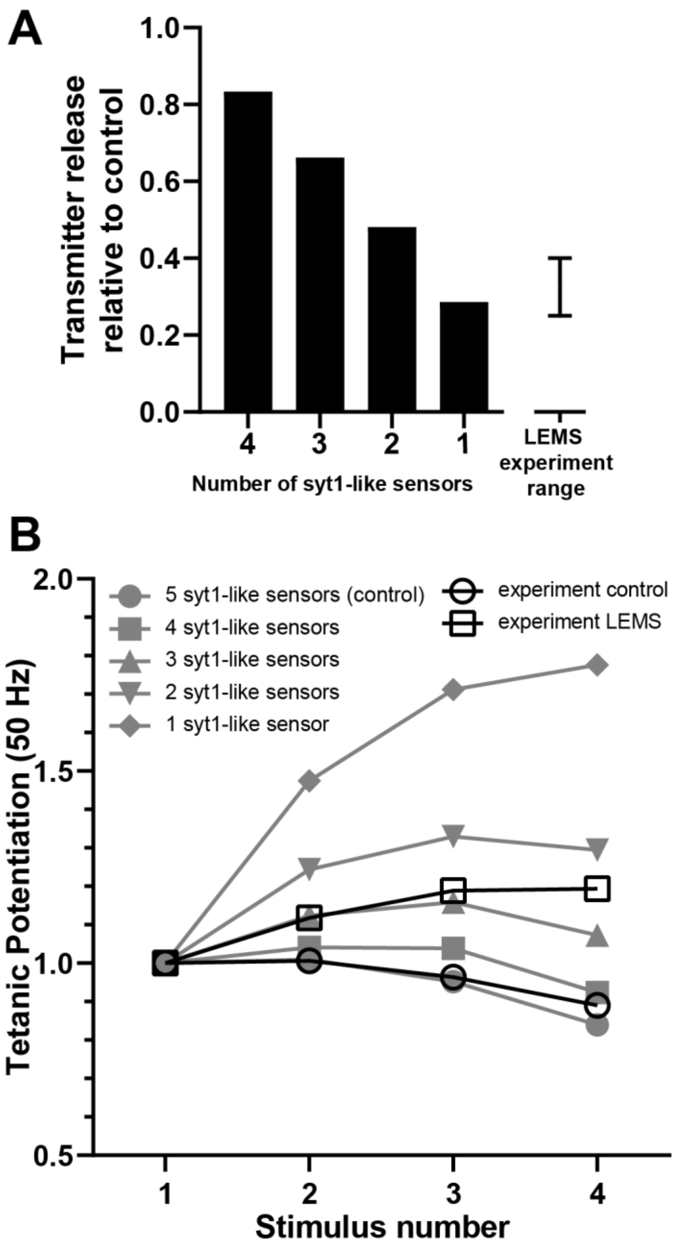

Figure 27 Reducing the number of syt1-like sensors in the MCell model produces levels of transmitter release and tetanic potentiation similar to those seen in experiments on LEMS-model mice.

A: The level of transmitter release of our healthy mouse AZ MCell model with reduced numbers of syt1-like sensors compared to the control model with 5 syt1-like sensors. Bar showing general range of experimental values for quantal content in LEMS-model mice compared to controls (25-40%) is added for comparison. *B*: tetanic potentiation over short trains of stimuli at 50 Hz, showing that a decrease in syt1-like sensors is associated with an increase in facilitation. Experimental results from (Tarr et al., 2013b).

4.3.4 Mechanisms of LEMS-induced reduction in transmitter release are predicted to differentially impact treatment effectiveness

3,4-DAP is a potassium channel antagonist that indirectly increases calcium flux into the nerve terminal by broadening the AP, which increases the probability that VGCCs in the terminal open during an AP (see chapter 3.0). It has been shown to be effective in increasing transmitter release in LEMS-model mice (Tarr et al., 2014) and partially alleviating symptoms of muscle-weakness in LEMS patients (Sanders, 1998; Sanders et al., 2018; Shieh et al., 2019; Strupp et al., 2017), and is currently the only FDA approved treatment for LEMS (Oh, 2020; Voelker, 2019; Yoon et al., 2020). However, 3,4-DAP has dose-limiting side effects, and the effectiveness of 3,4-DAP can vary greatly between patients such that up to 70% of LEMS patients require other treatments, such as immunotherapy, in combination with 3,4-DAP (Maddison et al., 2001; Titulaer et al., 2011a).

To our knowledge, no studies to date have studied potential mechanistic differences in the effectiveness of 3,4-DAP on seropositive and seronegative LEMS. However, one study on patients with a congenital syt2 mutation found that treatment with 3,4-DAP provided only slight improvements in symptoms and had provided no measurable change in initial compound muscle action potential although slight improvements were detected with single-fiber EMG (Whittaker et al., 2015). In comparison, 3,4-DAP was shown to increase compound muscle action potential in seropositive LEMS patients (Wirtz et al., 2009). Thus, we used our seronegative and seropositive LEMS models to investigate if the antibodies in LEMS could play a role in determining the effectiveness of 3,4-DAP treatment. We tested the effects of a clinically-relevant concentration (1.5µm) of 3,4-DAP on our MCell models by replacing the AP waveform in the simulations

(Figure 23A) with the average AP waveform from voltage-imaging recordings of the presynaptic terminal of the mouse NMJ in the presence of 1.5 µm 3,4-DAP (chapter 3.0) (Figure 23 B&C).

Experiments on LEMS-model mice generated using patient serum from seropositive patients found that 1.5 µm 3,4-DAP increased the quantal content of the LEMS-weakened NMJ terminals by 1.84 fold (Tarr et al., 2014). This result was accurately recapitulated by our seropositive LEMS MCell model, which predicted a 1.78 fold increase in transmitter release from the 1.5 µm 3,4-DAP-modified AP waveform compared to the control AP waveform. In contrast, the seronegative MCell models (MCell models with the same VGCC placement as the control MCell model, but fewer syt1-like sensors) did not see substantial increases in transmitter release from the 1.5 µm 3,4-DAP-modified AP waveform compared to the control AP waveform (Figure 28). These results suggest that the mechanism by which the AZ function is disrupted in LEMS may impact the effectiveness of LEMS treatments.

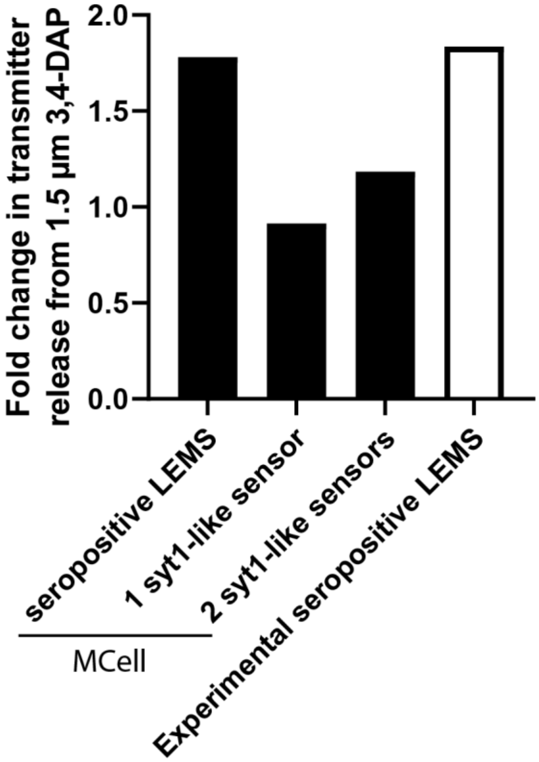

Figure 28 MCell models of seronegative LEMS have less improvement in transmitter release from 1.5 µM 3,4-DAP than the seropositive model.

The fold change in transmitter release resulting from the 3,4-DAP AP waveform compared to the control AP waveform for MCell models (black bars) of the seropositive LEMS model and the seronegative LEMS model with 1 or 2 syt-1 like sensors are compared to the experimentally recorded value (empty bar) from (Tarr et al., 2014).

4.4 Discussion

Here, we have constructed a computational model of a healthy mouse NMJ AZ. We then explored the impact of modifying this model based on physiological data collected in the mouse model for the neurological disease LEMS, which attacks the AZ. We demonstrated that by rearranging our healthy mouse model based on findings from freeze-fracture electron microscopy and measured calcium currents in LEMS-model mice, we were able to construct models of LEMS-modified AZs that were able to predict the electrophysiological behavior of LEMS. We then utilized our models to investigate the hypothesis that antibodies against fast calcium-sensing proteins (synaptotagmin-1 and -2) can result in the electrophysiological behavior seen in LEMS. Finally, we tested the impact of 3,4-DAP broadened AP waveforms, and found that our model predicted that the molecular mechanisms behind the loss of transmitter release in LEMS could impact response to this FDA-approved treatment.

4.4.1 Disruption of the AZ structure is essential for the presentation of seropositive LEMS

It is generally thought that, other than in rare seronegative cases, LEMS is caused by antibodies to P/Q-type VGCCs. The electrophysiological behavior of LEMS is often ascribed entirely to a loss of P/Q-type VGCCs and a compensatory upregulation of other VGCC types. However, this is a simplified notion of LEMS that ignores evidence from freeze-fracture electron microscopy showing a significant reduction in the number of AZs and a high level of dysregulation in the organization of many of the remaining AZs. Early freeze-fracture electron microscopy studies in human LEMS patients (Fukunaga et al., 1982) and LEMS-model mice which had been injected with low doses of human LEMS serum daily for several weeks (Fukunaga et al., 1983) found that LEMS NMJs had 70-85% fewer AZs per μm^2 than controls as well as a large increase in the number of disorganized clusters of intramembranous particles. A later study, which instead created LEMS-model mice by injecting a high dose of IgG three times daily for two days, again found a 70% reduction of normal AZs per μm^2 in LEMS-model mice compared to controls. They found an increase in the number of clusters, but also identified the presence of partially disrupted "abnormal" AZs. The authors of this study suggested these abnormal AZs were an intermediate stage between the normal well-organized AZ and the highly disorganized cluster, and this implied that the clusters were actually highly disorganized AZs (Fukuoka et al., 1987). Furthermore, these results showed that a removal of AZs and disruption of the remaining AZs was not a delayed response, but a rapid effect of the LEMS IgG.

Our model suggested that removing 40% of the P/Q-type VGCCs (as suggested by recordings of calcium currents in LEMS-model mice (Smith et al., 1995; Xu et al., 1998)) only reduced transmitter release by 42%. This is a lesser reduction of transmitter release than the 60-75% reduction seen in LEMS, and is much less than the 76-85% reduction in transmitter release seen in LEMS without compensatory upregulation of other VGCC types (Flink & Atchison, 2002). We also found that moving the location of VGCCs within the AZ an additional 20 nm away from the docked synaptic vesicles in AZ created a greater reduction in transmitter release than removing 40% of the VGCCs. Based on these computational results and the level of disorganization seen in freeze-fracture electron microscopy of LEMS NMJs, we hypothesize that the disorganization of normally well-ordered structure of AZs, beyond the simple removal of VGCCs, is an essential part of the pathology of seropositive LEMS.

4.4.2 VGCC antibodies and LEMS

Our results, along with the findings of other studies on seronegative LEMS, suggest that anti-VGCC antibodies are not necessary for LEMS. In addition, other evidence suggests that anti-VGCC antibodies alone may also not be sufficient for LEMS. In patients with small cell lung cancer and no symptoms of LEMS or other neurological dysfunction, it was found that 1-4% produced P/Q-type VGCC antibodies (Titulaer et al., 2009; Zalewski et al., 2016). Antibodies to P/Q-type VGCCs have been found in patients that present with a variety of other neurological conditions but not with symptoms of LEMS (Di Lorenzo et al., 2018; Zalewski et al., 2016), and also in healthy controls (Di Lorenzo et al., 2018; Lennon et al., 1995; Zalewski et al., 2016). Recent studies have found that tests for the presence of P/Q- and N-type VGCC antibodies have low sensitivity to detecting LEMS and produce a large number of false positives (Abboud et al., 2017; Albadareen et al., 2017; Di Lorenzo et al., 2018). Furthermore, rats injected with peptides or recombinant proteins to various VGCC domains were reported to have a reduction in quantal content, but only by about 30% (Komai, Iwasa, & Takamori, 1999; Takamori, Iwasa, & Komai, 1998), and this result has been difficult to reproduce (personal communication). This is less of a reduction than the 60-75% reduction in quantal content seen in LEMS-model mice. These findings suggest a possibility that although antibodies to P/Q-type VGCCs play an important role in a majority of LEMS cases, they may require cooperation with antibodies targeting other AZ proteins to cause the clinical symptoms of LEMS, especially when not present at high titer.

This multi-antibody hypothesis may be supported by the marked reduction in the number of AZs as well as a disruption of the normally well-organized structure of the remaining intramembranous particles comprising AZs seen in human LEMS patients (Fukunaga et al., 1982) and LEMS passive-transfer mice (Fukunaga et al., 1983; Fukuoka et al., 1987). The AZ contains numerous interconnected structural and functional proteins (Sudhof, 2012, 2013), and it is possible that auto-antibody mediated removal of P/Q-type VGCCs could result in damage to the AZ structure which would result in some level of disorganization. Furthermore, both P/Q-type VGCC knockout mice and N-type VGCC knockout mice have shown a reduction in the number of AZs (Chen, Billings, & Nishimune, 2011). However, the LEMS-mediated reduction in the total number of AZs and the high level of disruption in the organization of remaining AZs is perhaps a much greater level of damage to the AZ structure than one would expect from the removal of the number of P/Q-type VGCCs necessary to cause the 30-40% reduction in P/Q-type calcium current seen in LEMS (Smith et al., 1995; Xu et al., 1998).

4.4.3 Is the organization of the AZ altered in seronegative LEMS?

If an autoantibody attack on P/Q-type VGCCs can impact other AZ proteins attached to the VGCCs and subsequent disruption of the AZ organization, then there is also the possibility that antibody-mediated removal of other AZ proteins could indirectly result in the removal and disorganization of VGCCs. For example, the protein laminin β2 has been found to be essential for the expression of P/Q-type VGCCs in the AZs (Chand et al., 2015), and the interaction of laminin β2 and VGCCs is essential for the organization of the AZs (Chen et al., 2011; Nishimune, Sanes, & Carlson, 2004). Antibodies against the laminin β2-binding domain on P/Q-type VGCCs (Rogers & Nishimune, 2017; Takamori, Maruta, & Komai, 2000b) have been identified in LEMS patients. Although antibodies specifically against laminin β2 have not been identified in LEMS, it has been hypothesized that the presence of anti-laminin β2 antibodies (or antibodies against a variety of other AZ proteins) could cause LEMS. We propose that an in-depth characterization of antibodies present in LEMS patients could provide insight into seronegative LEMS and the mechanism of seropositive LEMS beyond anti-VGCC antibodies.

5.0 General discussion

5.1 The contribution of brief AP waveforms to the reliability of NMJs

Voltage imaging experiments in chapter 2.0 revealed that the AP waveform is very brief in the motor nerve terminal of the adult frog NMJ, with an average FWHM of only 274 μs. This is much briefer than the AP waveforms recorded from spinal motoneuron cell bodies of adult frogs (Dambach & Erulkar, 1973; Erulkar & Soller, 1980; Ovsepian & Vesselkin, 2006), and these AP waveforms from adult frog motoneurons are narrower than AP waveforms recorded from frog embryonic motoneuron synaptic varicosities (Pattillo et al., 2001; Yazejian et al., 1997). In chapter 3.0, we found that the AP waveform in the nerve terminals of adult mouse NMJs is also very brief, with an average FWHM of 264 μs. Furthermore, a recent study has found that the AP waveform in the soma of mouse spinal motoneurons is broader than our recorded waveform from the nerve terminal, and that the AP waveform in the soma narrows during maturation (Smith & Brownstone, 2020). Although the AP waveforms in the soma of frog and mouse spinal motoneurons are broader than the AP waveforms at the motoneuron nerve terminals, they are still quite narrow (<1 ms FWHM) compared to many other neuron types. For example, the AP in a mammalian midbrain dopamine neuron has an FWHM of approximately 4 ms (Bean, 2007). This suggests that mouse and frog spinal motoneurons share conserved mechanisms for a relatively narrow AP waveform in the soma, narrowing the AP waveform during maturation, and a further narrowing of the AP waveform as it propagates from the soma to the nerve terminal.

In section 2.4.1, we discussed how the narrowing of the AP during maturation in frog motoneurons is analogous to changes seen during maturation in the calyx of Held, and how those changes contribute to the strength and reliability of the adult calyx of Held. We also discussed how this narrow AP waveform could contribute to the strength and reliability of the NMJ by ensuring that only a small number of VGCCs open during an AP, which helps prevent depletion of the docked synaptic vesicles during trains of stimuli.

Narrow APs are often associated with a behavior referred to as “fast spiking”. Fast-spiking refers to the ability of some neurons to fire at high frequency for prolonged periods (Bean, 2007). This fast-spiking phenotype has been observed in several types of neurons including interneurons (Berke, 2011; Martina et al., 1998), Purkinje neurons (Martina, Metz, & Bean, 2007; Martina, Yao, & Bean, 2003; McKay & Turner, 2004; Southan & Robertson, 2000), neurons in the subthalamic nucleus (Bevan & Wilson, 1999; Wigmore & Lacey, 2000), and the calyx of Held (Brew & Forsythe, 1995; Ishikawa et al., 2003; Wang et al., 1998). The common mechanism creating the narrow APs that allow fast spiking in all of these neurons is thought to be the presence of the Kv3 family of voltage-gated potassium channels (Kaczmarek & Zhang, 2017; Rudy & McBain, 2001). This is the same type of Kv channel found in the mouse NMJ (Brooke et al., 2004), and likely the frog NMJ (although this has not yet been directly investigated experimentally). Thus, the narrow AP of the motoneurons and the presence of Kv3 channels suggests that frog and mouse motoneurons, like fast spiking neurons, are built for their reliability during repeated stimulation.

Another phenomenon seen in both mouse and frog motoneurons is the narrowing of the AP waveform as it propagates from the soma to the axon. This too is seen in other types of neurons, including granule cells in the dentate gyrus (Geiger & Jonas, 2000), layer 5 pyramidal neurons (Popovic et al., 2011), and cerebellar stellate cells (Rowan et al., 2016). The exact mechanisms by which this occurs are not completely understood, but appear to be a combination of changes in ion channel type and distribution as well as changes in membrane geometry (Ginebaugh et al., 2020;

Rowan et al., 2016; Rowan et al., 2014). We hypothesize that this narrowing of the AP between the soma and the axon further contributes to the reliability of the NMJ by helping to prevent depletion of docked synaptic vesicles.

Interestingly, these mechanisms are not conserved across all NMJs. The AP waveform at presynaptic terminal of the *Drosophila* NMJ is approximately six times broader than the AP waveforms at frog and mouse motoneuron terminals and does not narrow between soma and axon (Ford & Davis, 2014). The broader AP at the *Drosophila* motoneuron is likely due partially to the presence of Kv1 channels (Jan, Jan, & Dennis, 1977). Furthermore, the large difference in behavior and structure between the *Drosophila* NMJ and the mouse and frog NMJs is likely driven by the differences in function and organization of the muscle system of arthropods compared to vertebrates (Slater, 2015).

5.2 LEMS-modified organization of the AZ and its effects on synaptic transmission

It has long been thought that the reduction in calcium current through P/Q-type VGCCs is the primary mechanism by which transmitter release is reduced in LEMS. However, this is likely an over-simplistic view of LEMS. Measurements of calcium current in LEMS-model mice only saw a 30-40% reduction in P/Q-type calcium current (Smith et al., 1995; Xu et al., 1998), and freeze-fracture electron microscopy has shown a reduction in the number of AZs found in the NMJs of LEMS-model mice and human patients as well as a disorganization in the structure of remaining AZs. In chapter 4.0, our MCell models predicted that reducing 40% of P/Q-type VGCCs to match the experimentally measured LEMS-mediated reduction in P/Q-type calcium current would only cause a 42% reduction in quantal release; not nearly enough to match the experimentally measured reduction in transmitter release found in LEMS. In comparison, moving VGCCs 20 nm away from the docked synaptic vesicles in the AZs of the healthy mouse MCell model was predicted to reduce transmitter release by 61%. These results suggest that subtle changes to the normally well-organized structure of the mammalian AZ can have large effect, such that moving all of the VGCCs 20 nm away from the synaptic vesicles in the AZ had almost 1.5-fold greater of an effect on transmitter release than removing 40% of the VGCCs. The importance of AZ structure in determining its function (especially the distances between VGCCs and the calcium sensing proteins) is consistent with other modeling results (Bennett, Farnell, & Gibson, 2000a, 2000b; Matveev, Bertram, & Sherman, 2011)

In our P/Q-type-only LEMS model, removing 2 of the 6 AZs and moving the VGCCs 20 nm away from the docked synaptic vesicles in 3 of the 4 remaining AZs resulted in a 64% reduction in transmitter release compared to the control model. Randomly removing ~40% of the remaining channels only reduced transmitter release another 16% (for a total reduction of 80%). These findings suggest that the disruption of the AZ structure (the removal of AZs and the displacement of intramembranous particles in remaining AZs) has a much greater role in LEMS pathology than what is suggested in much of the LEMS literature. In fact, these results suggest that the removal and disorganization of AZs contributes much more to LEMS pathology than a reduction in the number of P/Q-type VGCCs.

Other than the reduction in transmitter release, another electrophysiological feature of LEMS is a large increase in tetanic potentiation over short trains of stimuli from a slight depression in healthy mouse NMJs to a facilitation in LEMS-model mouse NMJs. We found that removing ~40% of VGCCs in our healthy mouse MCell model only slightly increased tetanic potentiation. In contrast, moving all of the VGCCs 20 nm further away from the AZ greatly increased the facilitation. Surprisingly, a model in which the VGCCs were moved as well as having ~40% of them removed had a lesser facilitation than only moving the channels (Figure 29). The fact that two changes that each increase tetanic potentiation do not cause an even greater tetanic potentiation when combined suggests that the relationships between tetanic potentiation and VGCC number and placement are complex and nonlinear.

In our P/Q-type only LEMS model, the tetanic potentiation was much higher than in the control model, but was less than the model with both ~40% of VGCCs removed and all channels moved 20 nm away from the AZ. This is because the one “normal” AZ in our LEMS P/Q-only model was responsible for as much transmitter release as 2 to 3 of the “cluster” AZs, so the facilitation was skewed toward the levels seen in the “normal” AZ.

Our P/Q-type only LEMS model had less facilitation and transmitter release than the LEMS experimental results. Based on experimental data that L-type VGCCs are upregulated in LEMS and contribute to transmitter release, we examined the effect of placing more VGCCs even further outside the AZs. We found that adding more VGCCs further outside of the AZ was able to increase transmitter release and facilitation to LEMS experimental levels. This is consistent with the experimental data showing that L-type VGCCs contribute to transmitter release in LEMS (Flink & Atchison, 2002), and is also consistent with experimental results showing that L-type VGCCs contribute to facilitation in LEMS (Flink, 2003).

The experimental results from LEMS-model mice are highly variable. This is likely due to the high variability in antibody titer and type from the LEMS patients. In LEMS-model mice, the reduction in transmitter release often ranges from 60-75%. Similarly, there are differences seen in the levels of facilitation. During a short train of stimuli, the quantal content of the 4th stimulus commonly ranges from 1.2-1.4 times the quantal content of the 1st stimuli. The high impact of

VGCC placement in our model on both transmitter release and facilitation suggest that differences in the extent of AZ disorganization caused by variation in the antibody makeup of serum from LEMS patients could be a determining factor for electrophysiological variation in LEMS-model mice.

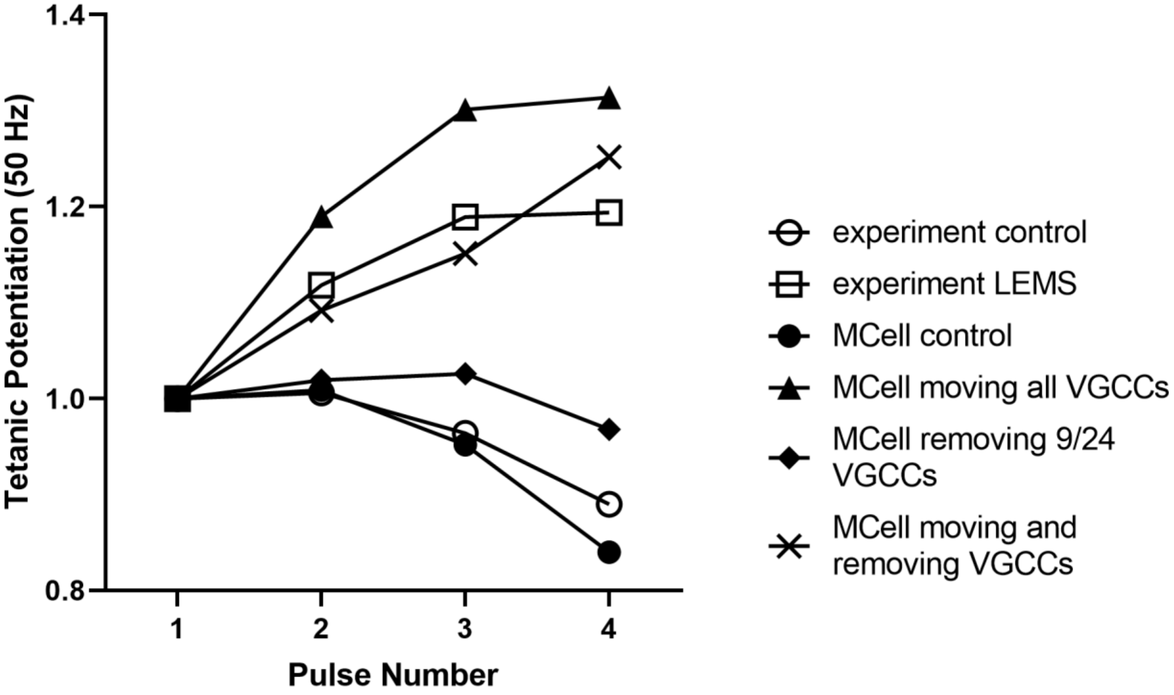

Figure 29 Changes in tetanic potentiation from altering the number and location of VGCCs in the healthy MCell model.

Removing 9/24 VGCCs (37.5%) in the MCell model causes a slight increase in facilitation compared to the control model. Moving all VGCCs in the MCell model 20 nm further away from the synaptic vesicles in the AZs causes a much greater facilitation. Both removing 9/24 VGCCs and moving the remaining VGCCs 20 nm further away from the synaptic vesicles in the AZs causes less facilitation than only moving the VGCCs.

5.3 The interaction between LEMS and the AP waveform at the NMJ

In Chapter 2.0 (Ginebaugh et al., 2020), it was shown that slight changes in the width of the AP waveform could create large changes in the calcium flux and transmitter release. Even a 35% increase in AP width was predicted to cause the probability of VGCCs opening and the total calcium flux during the AP to more than double. In an MCell model of an AZ in the frog NMJ, this AP-broadening-mediated increase in calcium flux was predicted to quadruple transmitter release (Figure 13). In our modeling of LEMS in chapter 4.0, we utilized the average AP waveform of our recordings from healthy mouse NMJs. However, it is possible that LEMS itself could alter the AP waveform and its propagation through the presynaptic terminal of the NMJ.

Calcium-activated potassium (BK) channels are known be present in NMJ AZs (see section 1.2.2). These BK channels help speed the repolarization phase of the AP, and blocking them has been shown to increase transmitter release — presumably through a broadening of the AP waveform. The BK channels are thought to be colocalized with VGCCs in the AZ to allow for a rapid transduction of the calcium signal from the VGCCs to the BK channels. It is unclear how the AZ disruption in LEMS would impact the BK channels: when VGCCs are targeted by antibodies and removed, are BK channels removed as well or do they remain in the AZ? When VGCCs are moved during the disorganization of the AZ, are the BK channels moved with them, or do the BK channels remain in their original position, or are the BK channels and VGCCs moved independently? It is almost certain that a reduction in the number of VGCCs alone would disrupt at least some of the BK channel activity, but the extent of this disruption would depend largely on how much the LEMS-induced disorganization of the AZ decouples the positioning of the VGCCs and BK channels. This disruption would be expected to broaden the AP waveform and reduce the impact of the BK channel blocker iberiotoxin (IBTX) on the behavior of the NMJ.

As mentioned previously, a slight broadening of the AP waveform can cause a large increase in calcium flux and transmitter release. For the construction of the LEMS MCell model, we removed 37.5% of the P/Q-type VGCCs to simulate the 30-40% reduction in P/Q-type calcium current seen in experiments on LEMS-model mice (Smith et al., 1995; Xu et al., 1998). Removing ~40% of the P/Q-type VGCCs to simulate a ~40% reduction in P/Q-type calcium current relies on the assumption that the AP waveform driving the behavior of VGCCs and calcium influx is unchanged. If there is a significant disruption of BK channel activity in LEMS and a subsequent broadening of the AP waveform, then the probability of VGCCs opening would increase, and a 40% reduction in P/Q-type calcium current would require a removal of greater than 40% of the P/Q-type VGCCs.

We performed some preliminary voltage-imaging experiments investigating the effects of the BK channel blocker iberiotoxin (IBTX) on the AP waveform in LEMS-model mice. These experiments were a pre- and post-drug paired-recording design similar to the experiments in section 3.2.2, where the AP waveform was recorded from a nerve terminal in a control bath and then the AP waveform was recorded again from the same nerve terminal after 30 minutes of bath exposure to the drug. In this experiment, the mice used were C57BL/6 mice that had been passively transferred LEMS via repeated injection of serum from human LEMS patients, and the drug used was 200 nM IBTX. In total, we successfully recorded pre-post drug effects from 6 different mice. We also recorded AP waveforms from an additional 5 terminals of LEMS model mice that did not have paired post-drug data. In the paired experiments, we found that there was a slight but not statistically significant broadening of the AP waveform after the addition of IBTX (Figure 30 **Error! Reference source not found.**A&B). Furthermore, there was no significance difference in FWHM between of the LEMS AP waveforms in control bath and the AP waveforms from healthy mice in the pre-drug vehicle bath from section 3.2.2 (Figure 30 C&D). However, the strain of the mice used in section 3.2.2 was swiss-webster rather than C57BL/6, and it is possible that differences in mouse strain could make a statistical comparison between the two experimental results incompatible. For proper conclusions regarding the impact of LEMS on the AP waveform and BK channel activity, the paired pre-post IBTX experiments should be performed on nerve terminals from healthy C57BL/6 mouse NMJs. I hypothesize that the pre-drug AP waveforms from healthy mice would be slightly narrower than the pre-drug AP waveform from the LEMS-model mice, and that IBTX would broaden the AP waveform in healthy mouse NMJs to the width of the LEMS-model mice AP waveforms. I also hypothesize that there is in fact a very slight broadening of the AP waveform in the LEMS-model mice. However, due to the high variability in voltage imaging and the small expected effect of IBTX on the AP waveform in LEMS-model mice, a larger *n* is needed before conclusions can be made.

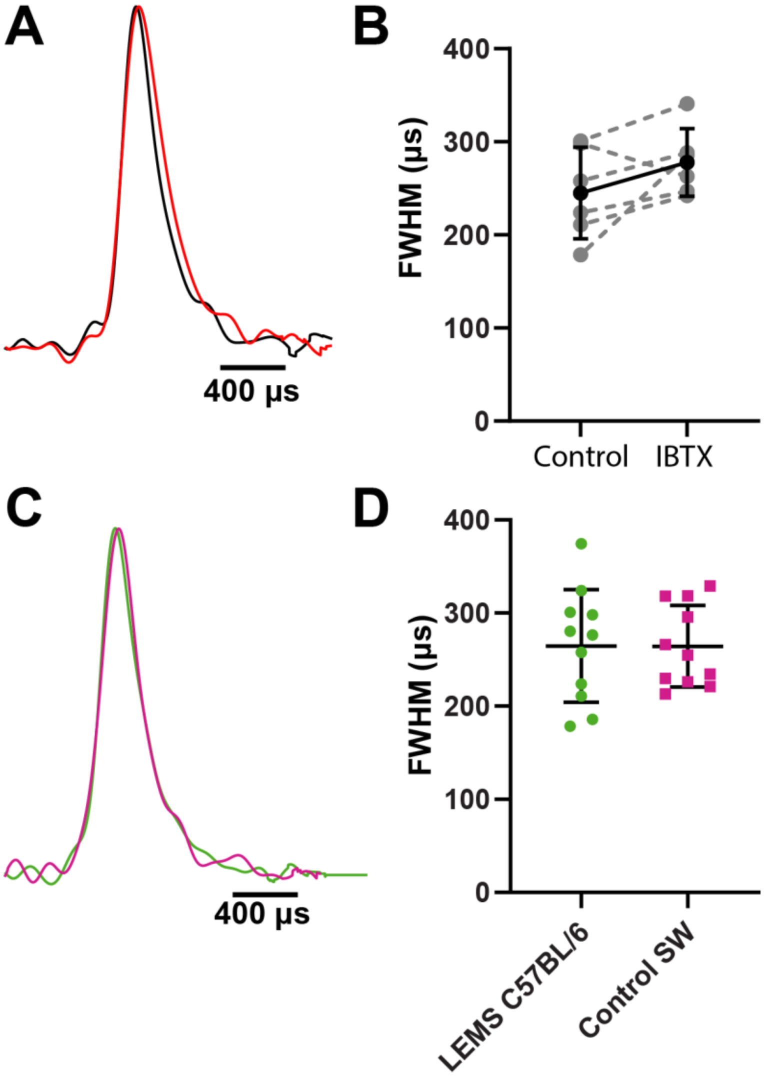

Figure 30 Effect of LEMS and IBTX on the presynaptic AP waveform in LEMS-model mouse NMJs.

A: The normalized average of all pre-drug (black) and post 200 nM IBTX (red) presynaptic AP waveform splines recorded from LEMS-model mouse motor nerve terminals (n = 6). *B*: Plots of individual paired recorded values (grey dotted lines) of AP duration (FWHM) before and after application of 200 nM IBTX with a superimposed average (solid black line). There is a slight but not statistically significant increase in FWHM (n = 6, p = 0.138, paired t-test). *C*: The normalized average of all control recordings from LEMS passive-transfer C57BL/6 mice (green trace, n = 11) and all pre-drug recordings from swiss-webster mice in section 3.2.2 (magenta trace, trace from Figure 16D, n = 11). *D*: There is no significant difference (p = 0.9883) in FWHM between AP waveforms recorded from *ex vivo* preparations from LEMS-model C57BL/6 mice (n = 11) and healthy Swiss Webster mice (n = 11, data from section 3.2.2).

5.4 BK channels as a future direction for research

The effect of IBTX on transmitter release in both mouse and frog NMJs suggests the presence of an important feedback mechanism by which VGCCs can alter the AP waveform and thus the behavior of the nerve terminal. In the presynaptic terminals of the frog and mouse NMJs, blocking BK channels causes an increase in transmitter release (Anderson et al., 1988; Flink & Atchison, 2003; Robitaille et al., 1993a; Robitaille & Charlton, 1992; Vatanpour & Harvey, 1995), and it is thought that the main function of BK channels in these NMJs is to create a more rapid repolarization of the AP. BK channels can have a wide variety of effects, and BK channels in other types of neurons and the NMJs of other species can have different effects than the BK channels in frog and mouse NMJs. For example, blocking BK channels in *Drosophila* NMJs (Lee, Ueda, & Wu, 2008) or mammalian CA1 pyramidal cells of the hippocampus (Hu et al., 2001) does not increase transmitter release. However, BK channels have been found to compensate for Kv channel inactivation during repeated stimulation in the presynaptic terminal of the *Drosophila* NMJ (Ford & Davis, 2014). This suggests that the BK channels are part of a complex feedback mechanism involving VGCCs, BK channels, and the AP waveform. To understand this feedback mechanism, a detailed analysis of the relationships between VGCCs, BK channels, and the AP waveform is necessary.

The impact of BK channels on the function of the nerve terminal and the unknowns regarding their functions suggest that research into BK channels is an important future direction. Future research into BK channels will help elucidate the behavior of the presynaptic terminal of the NMJ as well as the mechanisms regulating synaptic transmission in general. Furthermore, the behavior of BK channels in neurological diseases including LEMS is greatly understudied.

Currently, many of the computational tools available for the study of the behavior of neurons are not able to thoroughly investigate the mechanisms of BK channels. Because the function of BK channels is so heavily linked to their organization and relationship with VGCCs, programs such as NEURON that are not able to model neurons at the level of AZ organization have difficulty modeling the structure-function relationship between BK channels and VGCCs. Particle-based programs such as MCell can handle the structure-function relationship between BK channels and VGCCs, but are unable to rapidly analyze the output from the BK channels and use the information to accurately alter the AP waveform to simulate the effects of the BK channel feedback loop in subsequent time steps. To address this, development of a program called pyNEUCell is underway. This program is a combination of NEURON and MCell (with a python interface). At each time step, this program will compute the movement and behavior of particles using MCell and then send the results of the time step to NEURON, which will then use these results to recalculate input parameters for the next time step. For our MCell models of AZs in the frog and mouse NMJs, this would allow us to track the calcium ion binding and voltage activation of BK channels, and then use the information from the BK channels to alter the AP waveform for subsequent time steps. This will allow for the complete feedback mechanism of the BK channels to be simulated.

5.5 Heterogeneity or homogeneity among AZs?

Although our MCell model of healthy mouse AZs assumes that all AZs are the same, there is evidence that AZs are not homogenous. As mentioned in section 2.4.2, transmitter release in the frog motor nerve terminal has been found to be highest near the last node of Ranvier and decrease along the length of the terminal (D'Alonzo & Grinnell, 1985). We showed that changes in AP waveform may be responsible for some of these difference in transmitter release, but there is also the possibility that other unknown factors could be influencing differences in transmitter release along the length of the terminal. There is also evidence of AZ heterogeneity at the mouse NMJ. Much of this evidence comes from experiments utilizing synaptopHluorin (spH), a pH-sensitive exocytosis reporter (Miesenbock, De Angelis, & Rothman, 1998). The first spH studies at the mouse NMJ found that there were “hot spots” of release, suggesting that only some of the AZs contributed to release while the others were silent (Tabares et al., 2007; Wyatt & Balice-Gordon, 2008). However, these studies used repeated trains of stimuli to increase the fluorescence signal. A later study found that these hot spots were not present during single stimuli or short trains, but only appeared after a high frequency train of 5-25 stimuli (Gaffield, Tabares, & Betz, 2009).

The frog and mouse NMJs are not the only synapses with AZ heterogeneity. The *Drosophila* NMJ also shows significant variability in probability of release amongst AZs (Melom et al., 2013; Peled & Isacoff, 2011), as does the calyx of Held (Sheng et al., 2012). Multiple mechanisms for this variation in AZ function have been proposed. These include differences in actin (Sakaba & Neher, 2003), cAMP (Sakaba & Neher, 2001; Zhong & Zucker, 2005), and SNARE repriming (Deak et al., 2006; Rizo & Rosenmund, 2008). However, recent evidence at the *Drosophila* NMJ has suggested that variability in the number of VGCCs per AZ could be responsible for much of the variability for AZs (Akbergenova et al., 2018), and evidence from the calyx of Held has suggested that the distance between VGCCs and synaptic vesicles could contribute to AZ heterogeneity (Fekete et al., 2019).

Freeze-fracture electron microscopy of human LEMS patients and LEMS-model mice suggests that LEMS causes some AZs to be completely removed, other AZs to be turned into disorganized clusters of intramembranous particles, and a small portion of the AZs to remain relatively unchanged. The possibility of heterogeneity amongst AZs raises an important question about this phenomenon: is the outcome of a given AZ in LEMS a random chance based on which particles happen to be attacked by antibodies, or is the outcome influenced by the individual physiology of the AZ? If the heterogeneity among mouse AZs is caused by differences in the number or location of VGCCs within the AZs (similar to proposed mechanisms for AZ heterogeneity at the *Drosophila* NMJ or the calyx of Held), then it is possible that anti-VGCC antibodies would cause greater disruption to AZs that contain a greater number of VGCCs or have a tighter coupling of VGCCs with the AZ.

5.6 What causes seronegative LEMS?

Early investigations into LEMS revealed that repeatedly injecting mice with serum from human LEMS patients was able to passively transfer the disease, suggesting it was antibody mediated (Fukunaga et al., 1983; Lang et al., 1983). It was later discovered that LEMS patients expressed anti-VGCC antibodies (el Far et al., 1995; Lennon et al., 1995; Takamori et al., 1995). However, a minority of LEMS patients are seronegative for anti-VGCC antibodies.

The absence of anti-VGCC antibodies in some LEMS patients was noted in the first studies that identified P/Q-type VGCCs as the primary antibody for seropositive LEMS patients (Lennon et al., 1995; Takamori et al., 1995). In a later study, Nakao et al. discovered that seronegative LEMS can also be passively transferred to mice, and thus seronegative LEMS is also antibody mediated. The authors of that study suggested several different explanations for this phenomenon, including the possibility that antibodies toward certain P/Q-type VGCCs epitopes may not be detectable in their test, the titer of anti-VGCC antibodies were too low for detection by the test, or that seronegative LEMS was cause by antibodies to molecules other than P/Q type VGCCs (Nakao et al., 2002). There is growing evidence in support of their hypothesis that molecules other than P/Q-type VGCCs are responsible for seronegative LEMS. This includes reports that antibodies against P/Q-type VGCCs are not specific to LEMS and can occur in patients with other neurological diseases or even healthy controls (Abboud et al., 2017; Albadareen et al., 2017; Di Lorenzo et al., 2018; Lennon et al., 1995; Zalewski et al., 2016), multiple reports of antibodies against synaptotagmin-1 in both seropositive and seronegative LEMS patients (Takamori et al., 2000a; Takamori et al., 1995), experiments in mice showing that disrupting the function of synaptotagmin causes LEMS-like features (Pang et al., 2006a; Takamori et al., 1994), and reports of various congenital myasthenic syndromes in human patients (notably, one of which is caused by a mutation of synaptotagmin-2 (Herrmann et al., 2014)) that cause LEMS-like symptoms (Engel et al., 2015; Lorenzoni et al., 2018; Rodriguez Cruz, Palace, & Beeson, 2018). However, the specific antibodies responsible for seronegative LEMS have not yet been identified.

Myasthenia gravis (MG) is similar to LEMS in that both MG and LEMS are autoimmune-mediated neuromuscular diseases characterized by muscle weakness (Conti-Fine, Milani, & Kaminski, 2006). However, MG results from the immune system attacking the postsynaptic side of the NMJ, rather than the presynaptic side as in LEMS. In MG, the most common target for antibodies is the nicotinic acetylcholine receptor. The antibody mediated disruption of the acetylcholine receptors prevents muscles from receiving signals from the presynaptic terminal of the NMJ. Antibodies toward muscle-specific tyrosine kinase, which helps cluster the acetylcholine receptors in the postsynaptic membrane of the NMJ, can also be the main autoantibody in some MG patients (Hoch et al., 2001). Like LEMS, some MG patients are seronegative for these common MG-associated antibodies. The double-seronegative MG patients have been found to produce a variety of autoantibodies specific to other NMJ proteins, including antibodies toward LRP4, Kv1.4 channels, collagen Q, agrin, and contractin (Yi et al., 2018). Furthermore, a recent study using a high-sensitivity radioimmunoprecipitation assay identified titin autoantibodies in several seronegative MG patients (Stergiou et al., 2016). Thus, seronegative MG can likely be caused by a variety of autoantibodies, and it is likely that an in-depth investigation into autoantibodies produced by seronegative LEMS patients will also find a variety of pathogenic autoantibodies.

The most likely target for antibodies responsible for seronegative LEMS is synaptotagmin. As mentioned above, antibodies to synaptotagmin-1 have been identified in some, but not all, seronegative LEMS patients. However, synaptotagmin-2 is also important to transmitter release at mammalian NMJs (Pang et al., 2006a; Pang et al., 2006b), and it is not clear if the tests use to identify antibodies against synaptotagmin-1 would be able to identify antibodies against synaptotagmin-2. Thus, there is a possibility that the seronegative LEMS patients who tested negative for synaptotagmin-1 antibodies were simply producing synaptotagmin-2 antibodies instead. The hypothesis that anti-synaptotagmin antibodies could be responsible for seronegative LEMS is further supported by our computational modeling of AZs in the mouse NMJ in chapter 4.0, which showed that reducing the number of fast calcium sensors (that simulate the behavior of synaptotagmin-1 or -2) can predict the reduced transmitter release and increased facilitation seen in electrophysiology on LEMS-model mice.

There are several potential targets for autoantibodies in seronegative LEMS other than synaptotagmin. One potential target is M1 muscarinic acetylcholine receptors, as antibodies against these receptors have been found in LEMS patients (Takamori, 2008). In experiments on adult rat NMJs, chemically blocking M1 muscarinic acetylcholine receptors was found to reduce EPP amplitude by approximately 50% (Santafe et al., 2006; Santafe et al., 2003). Another potential target is laminin β2. Although antibodies against laminin β2 have not been identified in LEMS patients, mutations in laminin β2 have been found to cause a congenital myasthenic syndrome and a severe reduction in transmitter release at the NMJ (Maselli et al., 2009). Because laminin β2 has been shown to be important for the organization of AZs at the NMJ (Nishimune et al., 2004; Rogers & Nishimune, 2017), an antibody-mediated destruction of laminin β2 could cause disorganization in the AZs leading to LEMS. Many of the other mutations that cause congenital myasthenic syndromes affect proteins that are located inside the presynaptic terminal and do not contain transmembrane domains, so they are not likely targets for antibody-mediated removal. It is clear that a complete understanding of seronegative LEMS will require an extensive characterization of antibodies in LEMS patient serum.

5.7 Future research in LEMS treatment

Although much is understood about LEMS, the current FDA approved LEMS treatment (3,4-DAP) only provides a moderate improvement in symptoms. It is clear that there is still much to be done both in understanding the basic biology of LEMS and its effects on the NMJ as well as in development of more effective treatment for LEMS.

Our lab recently developed a novel calcium channel agonist, called GV-58, which directly increases transmitter release through P/Q- and N-type VGCCs by increasing their mean open time after they are opened by an increase in membrane voltage. GV-58 was found to have a similar effect on transmitter release as 3,4-DAP, but in combination with 3,4-DAP was shown to have a super-additive effect that completely restored neurotransmission in LEMS-model mice *ex vivo* preparations to healthy levels (Tarr et al., 2014). However, these *ex vivo* experiments were performed using the maximum tolerated concentration (1.5 µM) of 3,4-DAP and the maximally effective (50 µM) concentration of GV-58. Prior to potential clinical trials of this drug combination, a parameter sweep is necessary to determine the optimal combination of the two drugs to maximize effectiveness while minimizing dose-dependent side effects. Due to the difficulty in obtaining the human LEMS serum required to create LEMS-model mice, a large-scale parameter sweep of dose combinations is difficult. It may be possible to reduce the number of mice needed for such a parameter sweep by utilizing our MCell model of the LEMS-modified AZs to estimate the optimal combination of the two drugs. Using calcium current data from P/Q-type VGCCs expressed in HEK293 cells in the presence of GV-58 (Tarr et al., 2014) and new information on the mechanism of GV-58 (unpublished), we were able to simulate the effects of GV-58 and the supra-additive effects of GV-58 + 3,4-DAP on transmitter release in our MCell model of LEMS AZs from section 4.3.2 (Figure 31). This shows that utilizing our MCell models to perform an *in silico* parameter sweep of drug concentration combinations may be able to accurately estimate the optimal combination of GV-58 + 3,4-DAP for preclinical trails.

Another potential treatment for LEMS could come from improvements on the molecular structure of 3,4-DAP. 3,4-DAP was originally created by modifying the structure of another potassium channel agonist, 4-aminopyridine (4-AP). 4-AP, like 3,4-DAP, broadens the presynaptic AP at the NMJ. However, it crosses the blood-brain barrier at a higher rate than 3,4-DAP, and thus causes more severe central nervous system side effects that prevent it from being used at a high enough concentration to significantly improve symptoms in LEMS patients(Lemeignan et al., 1984; Lindquist & Stangel, 2014). Although 3,4-DAP does not cross the blood-brain barrier as easily as 4-AP, it still does so at high enough concentrations to limit its dosage in LEMS patients; at high concentrations, 3,4-DAP can cause seizures (Lindquist & Stangel, 2011; Wirtz et al., 2010; Wirtz et al., 2009). Our understanding of chemistry and ability to develop new drugs have significantly improved since the original synthesis of 3,4-DAP in the 1970s. A novel potassium channel agonist with an even lower ability to cross the blood-brain barrier could possibly be used at higher concentrations in LEMS patients to further broaden the AP waveform and increase transmitter release at the NMJ without causing severe central nervous system side effects like seizures.

Finally, our understanding of the immune system and our ability to modulate its function have recently greatly improved, largely due to advances in sequencing technology and systems biology. Single-cell RNA-seq is particularly useful for investigating the transcriptomic changes in immune cells that contribute to diseased states. Recent preliminary investigations have been made in myasthenia gravis transcriptomics (Guo et al., 2019; Lee et al., 2020; Park et al., 2016), however these used bulk transcriptomic techniques rather than single-cell, which would not allow investigations into the changes in gene expression of specific immune cell types (Chen, Ye, & Guo, 2019). Using single-cell RNA-seq, future investigations into the transcriptomic alterations of immune cells in LEMS patients may provide novel insights into the causes and potential treatments of LEMS.

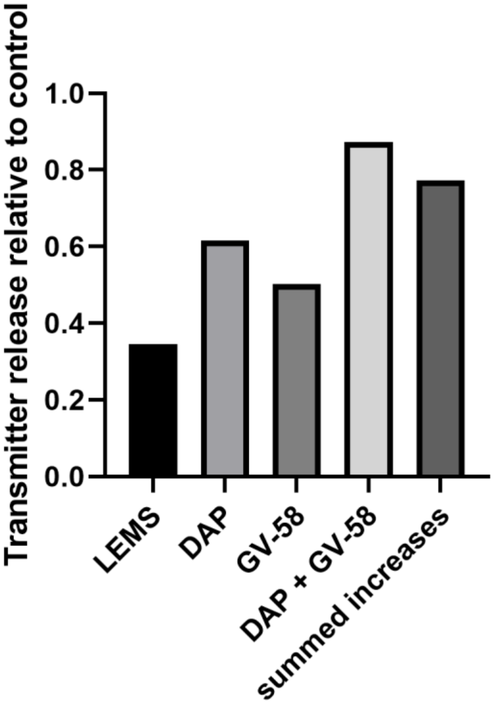

Figure 31 MCell model of LEMS AZs predicts a super-additive effect of DAP + GV-58.

Quantity of transmitter release of various MCell models of LEMS AZs relative to the MCell model of healthy mouse AZs. Values for the LEMS AZ with the 3,4-DAP-modified AP waveform, a GV-58-modified VGCC gating scheme, or both the modified AP waveform and the modified VGCC gating scheme are shown. The combination of the two drugs has a super-additive effect in that it caused a greater improvement in transmitter release than the sum of the increases in transmitter release caused by each drug separately.

Bibliography

Abbe, E. (1873). Beiträge zur Theorie des Mikroskops und der mikroskopischen Wahrnehmung. *Archiv f. mikrosk. Anatomie, 9*, 413-468. doi:10.1007/BF02956173

Abboud, H., Rossman, I., Mealy, M. A., Hill, E., Thompson, N., Banerjee, A., . . . Levy, M. (2017). Neuronal autoantibodies: differentiating clinically relevant and clinically irrelevant results. *J Neurol, 264*(11), 2284-2292. doi:10.1007/s00415-017-8627-4

Adler, E. M., Augustine, G. J., Duffy, S. N., & Charlton, M. P. (1991). Alien intracellular calcium chelators attenuate neurotransmitter release at the squid giant synapse. *J Neurosci, 11*(6), 1496-1507.

Akbergenova, Y., Cunningham, K. L., Zhang, Y. V., Weiss, S., & Littleton, J. T. (2018). Characterization of developmental and molecular factors underlying release heterogeneity at Drosophila synapses. *Elife, 7*. doi:10.7554/eLife.38268

Albadareen, R., Gronseth, G., Goeden, M., Sharrock, M., Lechtenberg, C., & Wang, Y. (2017). Paraneoplastic autoantibody panels: sensitivity and specificity, a retrospective cohort. *Int J Neurosci, 127*(6), 531-538. doi:10.1080/00207454.2016.1207644

Alle, H., Kubota, H., & Geiger, J. R. (2011). Sparse but highly efficient Kv3 outpace BKCa channels in action potential repolarization at hippocampal mossy fiber boutons. *J Neurosci, 31*(22), 8001-8012. doi:10.1523/JNEUROSCI.0972-11.2011

Anderson, A. J., Harvey, A. L., Rowan, E. G., & Strong, P. N. (1988). Effects of charybdotoxin, a blocker of Ca2+-activated K+ channels, on motor nerve terminals. *Br J Pharmacol, 95*(4), 1329-1335. doi:10.1111/j.1476-5381.1988.tb11772.x

Arai, I., & Jonas, P. (2014). Nanodomain coupling explains Ca(2)(+) independence of transmitter release time course at a fast central synapse. *Elife, 3*. doi:10.7554/eLife.04057

Arganda-Carreras, I., Fernandez-Gonzalez, R., Munoz-Barrutia, A., & Ortiz-De-Solorzano, C. (2010). 3D reconstruction of histological sections: Application to mammary gland tissue. *Microsc Res Tech, 73*(11), 1019-1029. doi:10.1002/jemt.20829

Atchison, W. D. (1989). Dihydropyridine-sensitive and -insensitive components of acetylcholine release from rat motor nerve terminals. *J Pharmacol Exp Ther, 251*(2), 672-678.

Atchison, W. D., & O'Leary, S. M. (1987). Bay K 8644 increases release of acetylcholine at the murine neuromuscular junction. *Brain Research, 419*(1), 315-319. doi:10.1016/0006-8993(87)90599-3

Banwell, B. L., Ohno, K., Sieb, J. P., & Engel, A. G. (2004). Novel truncating RAPSN mutations causing congenital myasthenic syndrome responsive to 3,4-diaminopyridine. *Neuromuscul Disord, 14*(3), 202-207. doi:10.1016/j.nmd.2003.11.004

Bartol, T. M., Jr., Land, B. R., Salpeter, E. E., & Salpeter, M. M. (1991). Monte Carlo simulation of miniature endplate current generation in the vertebrate neuromuscular junction. *Biophys J, 59*(6), 1290-1307. doi:10.1016/S0006-3495(91)82344-X

Baydyuk, M., Xu, J., & Wu, L. G. (2016). The calyx of Held in the auditory system: Structure, function, and development. *Hear Res, 338,* 22-31. doi:10.1016/j.heares.2016.03.009

Bean, B. P. (2007). The action potential in mammalian central neurons. *Nat Rev Neurosci, 8*(6), 451-465. doi:10.1038/nrn2148

Beier, H. T., Roth, C. C., Bixler, J. N., Sedelnikova, A. V., & Ibey, B. L. (2019). Visualization of Dynamic Sub-microsecond Changes in Membrane Potential. *Biophys J, 116*(1), 120-126. doi:10.1016/j.bpj.2018.11.3129

Bennett, M., Jones, P., & Lavidis, N. (1986a). Transmitter secretion varies between visualized release sites at amphibian neuromuscular junctions. *Neurosci Lett, 65*(3), 311-315. doi:10.1016/0304-3940(86)90280-6

Bennett, M. R., Farnell, L., & Gibson, W. G. (2000a). The probability of quantal secretion near a single calcium channel of an active zone. *Biophys J, 78*(5), 2201-2221. doi:10.1016/S0006-3495(00)76769-5

Bennett, M. R., Farnell, L., & Gibson, W. G. (2000b). The probability of quantal secretion within an array of calcium channels of an active zone. *Biophys J, 78*(5), 2222-2240. doi:10.1016/S0006-3495(00)76770-1

Bennett, M. R., Jones, P., & Lavidis, N. A. (1986b). The probability of quantal secretion along visualized terminal branches at amphibian (Bufo marinus) neuromuscular synapses. *J Physiol, 379*, 257-274. doi:10.1113/jphysiol.1986.sp016252

Bennett, M. R., Lavidis, N. A., & Lavidis-Armson, F. (1989). The probability of quantal secretion at release sites of different length in toad (Bufo marinus) muscle. *J Physiol, 418*, 235-249. doi:10.1113/jphysiol.1989.sp017837

Berke, J. D. (2011). Functional properties of striatal fast-spiking interneurons. *Front Syst Neurosci, 5*, 45. doi:10.3389/fnsys.2011.00045

Bevan, M. D., & Wilson, C. J. (1999). Mechanisms underlying spontaneous oscillation and rhythmic firing in rat subthalamic neurons. *J Neurosci, 19*(17), 7617-7628.

Bezanilla, F. (2000). The voltage sensor in voltage-dependent ion channels. *Physiol Rev, 80*(2), 555-592. doi:10.1152/physrev.2000.80.2.555

Bonanno, S., Pasanisi, M. B., Frangiamore, R., Maggi, L., Antozzi, C., Andreetta, F., . . . Mantegazza, R. (2018). Amifampridine phosphate in the treatment of muscle-specific kinase myasthenia gravis: a phase IIb, randomized, double-blind, placebo-controlled, double crossover study. *SAGE Open Medicine, 6*, 2050312118819013. doi:10.1177/2050312118819013

Borst, J. G., & Sakmann, B. (1998). Calcium current during a single action potential in a large presynaptic terminal of the rat brainstem. *J Physiol, 506 (Pt 1)*, 143-157. doi:10.1111/j.1469-7793.1998.143bx.x

Borst, J. G., & Sakmann, B. (1999). Effect of changes in action potential shape on calcium currents and transmitter release in a calyx-type synapse of the rat auditory brainstem. *Philos Trans R Soc Lond B Biol Sci, 354*(1381), 347-355. doi:10.1098/rstb.1999.0386

Boutin, E., Rey, C., Romeu, M., Pouget, J., & Franques, J. (2013). [Favourable outcome after treatment with rituximab in a case of seronegative non-paraneoplastic Lambert-Eaton myasthenic syndrome]. *Rev Med Interne, 34*(8), 493-496. doi:10.1016/j.revmed.2013.04.007

Braun, M., & Schmidt, R. F. (1966). Potential changes recorded from the frog motor nerve terminal during its activation. *Pflugers Arch Gesamte Physiol Menschen Tiere, 287*(1), 56-80. doi:10.1007/BF00362454

Brew, H. M., & Forsythe, I. D. (1995). Two voltage-dependent K+ conductances with complementary functions in postsynaptic integration at a central auditory synapse. *J Neurosci, 15*(12), 8011-8022.

Brooke, R. E., Moores, T. S., Morris, N. P., Parson, S. H., & Deuchars, J. (2004). Kv3 voltage-gated potassium channels regulate neurotransmitter release from mouse motor nerve terminals. *Eur J Neurosci, 20*(12), 3313-3321. doi:10.1111/j.1460-9568.2004.03730.x

Bucurenciu, I., Kulik, A., Schwaller, B., Frotscher, M., & Jonas, P. (2008). Nanodomain coupling between Ca2+ channels and Ca2+ sensors promotes fast and efficient transmitter release at a cortical GABAergic synapse. *Neuron, 57*(4), 536-545. doi:10.1016/j.neuron.2007.12.026

Burkitt, A. N. (2006). A review of the integrate-and-fire neuron model: I. Homogeneous synaptic input. *Biol Cybern, 95*(1), 1-19. doi:10.1007/s00422-006-0068-6

Caldwell, J. H., Schaller, K. L., Lasher, R. S., Peles, E., & Levinson, S. R. (2000). Sodium channel Na(v)1.6 is localized at nodes of ranvier, dendrites, and synapses. *Proc Natl Acad Sci U S A, 97*(10), 5616-5620. doi:10.1073/pnas.090034797

Campbell, D. L., Giles, W. R., & Shibata, E. F. (1988). Ion transfer characteristics of the calcium current in bull-frog atrial myocytes. *J Physiol, 403*, 239-266. doi:10.1113/jphysiol.1988.sp017248

Carnevale, N. T., & Hines, M. L. (2005). *The NEURON book*. Cambridge ; New York: Cambridge University Press.

Castle, N. A., Fadous, S., Logothetis, D. E., & Wang, G. K. (1994). Aminopyridine block of Kv1.1 potassium channels expressed in mammalian cells and Xenopus oocytes. *Mol Pharmacol, 45*(6), 1242-1252.

Catterall, W. A. (1999). Interactions of presynaptic Ca2+ channels and snare proteins in neurotransmitter release. *Ann N Y Acad Sci, 868*, 144-159. doi:10.1111/j.1749-6632.1999.tb11284.x

Catterall, W. A. (2010). Ion channel voltage sensors: structure, function, and pathophysiology. *Neuron, 67*(6), 915-928. doi:10.1016/j.neuron.2010.08.021

Catterall, W. A. (2011). Voltage-gated calcium channels. *Cold Spring Harb Perspect Biol, 3*(8), a003947. doi:10.1101/cshperspect.a003947

Chand, K. K., Lee, K. M., Schenning, M. P., Lavidis, N. A., & Noakes, P. G. (2015). Loss of beta2-laminin alters calcium sensitivity and voltage-gated calcium channel maturation of neurotransmission at the neuromuscular junction. *J Physiol, 593*(1), 245-265. doi:10.1113/jphysiol.2014.284133

Chen, C., Satterfield, R., Young, S. M., Jr., & Jonas, P. (2017). Triple Function of Synaptotagmin 7 Ensures Efficiency of High-Frequency Transmission at Central GABAergic Synapses. *Cell Rep, 21*(8), 2082-2089. doi:10.1016/j.celrep.2017.10.122

Chen, H., Ye, F., & Guo, G. (2019). Revolutionizing immunology with single-cell RNA sequencing. *Cell Mol Immunol, 16*(3), 242-249. doi:10.1038/s41423-019-0214-4

Chen, J., Billings, S. E., & Nishimune, H. (2011). Calcium channels link the muscle-derived synapse organizer laminin beta2 to Bassoon and CAST/Erc2 to organize presynaptic active zones. *J Neurosci, 31*(2), 512-525. doi:10.1523/JNEUROSCI.3771-10.2011

Chen, Z., Das, B., Nakamura, Y., DiGregorio, D. A., & Young, S. M., Jr. (2015). Ca2+ channel to synaptic vesicle distance accounts for the readily releasable pool kinetics at a functionally mature auditory synapse. *J Neurosci, 35*(5), 2083-2100. doi:10.1523/JNEUROSCI.2753-14.2015

Cohen, M. W., Jones, O. T., & Angelides, K. J. (1991). Distribution of Ca2+ channels on frog motor nerve terminals revealed by fluorescent omega-conotoxin. *J Neurosci, 11*(4), 1032-1039.

Collot, M., Ashokkumar, P., Anton, H., Boutant, E., Faklaris, O., Galli, T., . . . Klymchenko, A. S. (2019). MemBright: A Family of Fluorescent Membrane Probes for Advanced Cellular Imaging and Neuroscience. *Cell Chem Biol, 26*(4), 600-614 e607. doi:10.1016/j.chembiol.2019.01.009

Conti-Fine, B. M., Milani, M., & Kaminski, H. J. (2006). Myasthenia gravis: past, present, and future. *J Clin Invest, 116*(11), 2843-2854. doi:10.1172/JCI29894

Couteaux, R., & Pecot-Dechavassine, M. (1970). [Synaptic vesicles and pouches at the level of "active zones" of the neuromuscular junction]. *C R Acad Hebd Seances Acad Sci D, 271*(25), 2346-2349.

D'Alonzo, A. J., & Grinnell, A. D. (1985). Profiles of evoked release along the length of frog motor nerve terminals. *J Physiol, 359,* 235-258. doi:10.1113/jphysiol.1985.sp015583

Dambach, G. E., & Erulkar, S. D. (1973). The action of calcium at spinal neurones of the frog. *J Physiol, 228*(3), 799-817. doi:10.1113/jphysiol.1973.sp010113

David, P., el Far, O., Martin-Mouto, N., Poupon, M. F., Takahashi, M., & Seagar, M. J. (1993). Expression of synaptotagmin and syntaxin associated with N-type calcium channels in small cell lung cancer. *FEBS Lett, 326*(1-3), 135-139. doi:10.1016/0014-5793(93)81777-w

Deak, F., Shin, O. H., Tang, J., Hanson, P., Ubach, J., Jahn, R., . . . Sudhof, T. C. (2006). Rabphilin regulates SNARE-dependent re-priming of synaptic vesicles for fusion. *EMBO J, 25*(12), 2856-2866. doi:10.1038/sj.emboj.7601165

Dean, C., Dunning, F. M., Liu, H., Bomba-Warczak, E., Martens, H., Bharat, V., . . . Chapman, E. R. (2012). Axonal and dendritic synaptotagmin isoforms revealed by a pHluorin-syt functional screen. *Mol Biol Cell, 23*(9), 1715-1727. doi:10.1091/mbc.E11-08-0707

Del Castillo, J., & Katz, B. (1957a). A comparison of acetylcholine and stable depolarizing agents. *Proc R Soc Lond B Biol Sci, 146*(924), 362-368. doi:10.1098/rspb.1957.0017

Del Castillo, J., & Katz, B. (1957b). The identity of intrinsic and extrinsic acetylcholine receptors in the motor end-plate. *Proc R Soc Lond B Biol Sci, 146*(924), 357-361. doi:10.1098/rspb.1957.0016

Del Castillo, J., & Katz, B. (1957c). Interaction at end-plate receptors between different choline derivatives. *Proc R Soc Lond B Biol Sci, 146*(924), 369-381. doi:10.1098/rspb.1957.0018

Del Castillo, L., & Katz, B. (1957d). A study of curare action with an electrical micromethod. *Proc R Soc Lond B Biol Sci, 146*(924), 339-356. doi:10.1098/rspb.1957.0015

DeStefino, N. R., Pilato, A. A., Dittrich, M., Cherry, S. V., Cho, S., Stiles, J. R., & Meriney, S. D. (2010). (R)-roscovitine prolongs the mean open time of unitary N-type calcium channel currents. *Neuroscience, 167*(3), 838-849. doi:10.1016/j.neuroscience.2010.02.041

Di Lorenzo, R., Mente, K., Li, J., Shayya, L., Rae-Grant, A., Li, Y., & Jammoul, A. (2018). Low specificity of voltage-gated calcium channel antibodies in Lambert-Eaton myasthenic syndrome: a call for caution. *J Neurol, 265*(9), 2114-2119. doi:10.1007/s00415-018-8959-8

Dittrich, M., Pattillo, J. M., King, J. D., Cho, S., Stiles, J. R., & Meriney, S. D. (2013). An excess-calcium-binding-site model predicts neurotransmitter release at the neuromuscular junction. *Biophys J, 104*(12), 2751-2763. doi:10.1016/j.bpj.2013.05.023

Dodge, F. A., Jr., & Rahamimoff, R. (1967). Co-operative action a calcium ions in transmitter release at the neuromuscular junction. *J Physiol, 193*(2), 419-432. doi:10.1113/jphysiol.1967.sp008367

Eaton, L. M., & Lambert, E. H. (1957). Electromyography and electric stimulation of nerves in diseases of motor unit; observations on myasthenic syndrome associated with malignant tumors. *J Am Med Assoc, 163*(13), 1117-1124. doi:10.1001/jama.1957.02970480021005

Eggermann, E., Bucurenciu, I., Goswami, S. P., & Jonas, P. (2011). Nanodomain coupling between Ca(2)(+) channels and sensors of exocytosis at fast mammalian synapses. *Nat Rev Neurosci, 13*(1), 7-21. doi:10.1038/nrn3125

el Far, O., Marqueze, B., Leveque, C., Martin-Moutot, N., Lang, B., Newsom-Davis, J., . . . Seagar, M. J. (1995). Antigens associated with N- and L-type calcium channels in Lambert-Eaton myasthenic syndrome. *J Neurochem, 64*(4), 1696-1702. doi:10.1046/j.1471-4159.1995.64041696.x

Elezgarai, I., Diez, J., Puente, N., Azkue, J. J., Benitez, R., Bilbao, A., . . . Grandes, P. (2003). Subcellular localization of the voltage-dependent potassium channel Kv3.1b in postnatal and adult rat medial nucleus of the trapezoid body. *Neuroscience, 118*(4), 889-898. doi:10.1016/s0306-4522(03)00068-x

Engel, A. G., Shen, X. M., Selcen, D., & Sine, S. M. (2015). Congenital myasthenic syndromes: pathogenesis, diagnosis, and treatment. *Lancet Neurol, 14*(5), 461. doi:10.1016/S1474-4422(15)00010-1

Ertel, E. A., Campbell, K. P., Harpold, M. M., Hofmann, F., Mori, Y., Perez-Reyes, E., . . . Catterall, W. A. (2000). Nomenclature of voltage-gated calcium channels. *Neuron, 25*(3), 533-535. doi:10.1016/s0896-6273(00)81057-0

Erulkar, S. D., & Soller, R. W. (1980). Interactions among lumbar motoneurons on opposite sides of the frog spinal cord: morphological and electrophysiological studies. *J Comp Neurol, 192*(3), 473-488. doi:10.1002/cne.901920307

Fakler, B., & Adelman, J. P. (2008). Control of K(Ca) channels by calcium nano/microdomains. *Neuron, 59*(6), 873-881. doi:10.1016/j.neuron.2008.09.001

FDA. (2018). FDA approves first treatment for Lambert-Eaton myasthenic syndrome, a rare autoimmune disorder [Press release]. Retrieved from https://www.fda.gov/news-events/press-announcements/fda-approves-first-treatment-lambert-eaton-myasthenic-syndrome-rare-autoimmune-disorder

FDA. (2019). FDA approves first treatment for children with Lambert-Eaton myasthenic syndrome, a rare autoimmune disorder [Press release]. Retrieved from https://www.fda.gov/news-events/press-announcements/fda-approves-first-treatment-children-lambert-eaton-myasthenic-syndrome-rare-autoimmune-disorder

Fedchyshyn, M. J., & Wang, L. Y. (2005). Developmental transformation of the release modality at the calyx of Held synapse. *J Neurosci, 25*(16), 4131-4140. doi:10.1523/JNEUROSCI.0350-05.2005

Fekete, A., Nakamura, Y., Yang, Y. M., Herlitze, S., Mark, M. D., DiGregorio, D. A., & Wang, L. Y. (2019). Underpinning heterogeneity in synaptic transmission by presynaptic ensembles of distinct morphological modules. *Nat Commun, 10*(1), 826. doi:10.1038/s41467-019-08452-2

Fiona, N., Lee, D. C., Schrumpf, L. A., Mazurek, M. E., Lo, V. L., Gill, S. K., & Maselli, R. A. (2017). Effect of 3,4-diaminopyridine at the murine neuromuscular junction. *Muscle Nerve, 55*(2), 223-231. doi:doi:10.1002/mus.25208

Flet, L., Polard, E., Guillard, O., Leray, E., Allain, H., Javaudin, L., & Edan, G. (2010). 3,4-Diaminopyridine safety in clinical practice: an observational, retrospective cohort study. *Journal of Neurology, 257*(6), 937-946. doi:10.1007/s00415-009-5442-6

Flink, M. T. (2003). *The role of L-type calcium ion channels in release of acetylcholine from motor nerve terminals following passive transfer of lambert-eaton myasthenic syndrome to mature mice.* (Doctor of Philosophy). Michigan State University, ProQuest Dissertations & Theses Global database.

Flink, M. T., & Atchison, W. D. (2002). Passive transfer of Lambert-Eaton syndrome to mice induces dihydropyridine sensitivity of neuromuscular transmission. *J Physiol, 543*(Pt 2), 567-576. doi:10.1113/jphysiol.2002.021048

Flink, M. T., & Atchison, W. D. (2003). Iberiotoxin-induced block of Ca2+-activated K+ channels induces dihydropyridine sensitivity of ACh release from mammalian motor nerve terminals. *J Pharmacol Exp Ther, 305*(2), 646-652. doi:10.1124/jpet.102.046102

Ford, K. J., & Davis, G. W. (2014). Archaerhodopsin voltage imaging: synaptic calcium and BK channels stabilize action potential repolarization at the Drosophila neuromuscular junction. *J Neurosci, 34*(44), 14517-14525. doi:10.1523/JNEUROSCI.2203-14.2014

Forsythe, I. D., Tsujimoto, T., Barnes-Davies, M., Cuttle, M. F., & Takahashi, T. (1998). Inactivation of presynaptic calcium current contributes to synaptic depression at a fast central synapse. *Neuron, 20*(4), 797-807. doi:10.1016/s0896-6273(00)81017-x

Fukunaga, H., Engel, A., Osame, M., & Lambert, E. H. (1982). Paucity and disorganisation of presynaptic membrane active zones in the Lambert-Eaton myasthenic syndrome. *Muscle Nerve, 5*(686).

Fukunaga, H., Engel, A. G., Lang, B., Newsom-Davis, J., & Vincent, A. (1983). Passive transfer of Lambert-Eaton myasthenic syndrome with IgG from man to mouse depletes the presynaptic membrane active zones. *Proc Natl Acad Sci U S A, 80*(24), 7636-7640. doi:10.1073/pnas.80.24.7636

Fukuoka, T., Engel, A. G., Lang, B., Newsom-Davis, J., Prior, C., & Wray, D. W. (1987). Lambert-Eaton myasthenic syndrome: I. Early morphological effects of IgG on the presynaptic membrane active zones. *Ann Neurol, 22*(2), 193-199. doi:10.1002/ana.410220203

Gaffield, M. A., Tabares, L., & Betz, W. J. (2009). The spatial pattern of exocytosis and post-exocytic mobility of synaptopHluorin in mouse motor nerve terminals. *J Physiol, 587*(Pt 6), 1187-1200. doi:10.1113/jphysiol.2008.166728

Geiger, J. R., & Jonas, P. (2000). Dynamic control of presynaptic Ca(2+) inflow by fast-inactivating K(+) channels in hippocampal mossy fiber boutons. *Neuron, 28*(3), 927-939. doi:10.1016/s0896-6273(00)00164-1

Ginebaugh, S. P., Cyphers, E. D., Lanka, V., Ortiz, G., Miller, E. W., Laghaei, R., & Meriney, S. D. (2020). The Frog Motor Nerve Terminal Has Very Brief Action Potentials and Three Electrical Regions Predicted to Differentially Control Transmitter Release. *J Neurosci, 40*(18), 3504-3516. doi:10.1523/JNEUROSCI.2415-19.2020

Giovannini, F., Sher, E., Webster, R., Boot, J., & Lang, B. (2002). Calcium channel subtypes contributing to acetylcholine release from normal, 4-aminopyridine-treated and myasthenic syndrome auto-antibodies-affected neuromuscular junctions. *Br J Pharmacol, 136*(8), 1135-1145. doi:10.1038/sj.bjp.0704818

Grinnell, A. D., & Herrera, A. A. (1980). Physiological regulation of synaptic effectiveness at frog neuromuscular junctions. *J Physiol, 307*, 301-317. doi:10.1113/jphysiol.1980.sp013436

Grissmer, S., Nguyen, A. N., Aiyar, J., Hanson, D. C., Mather, R. J., Gutman, G. A., . . . Chandy, K. G. (1994). Pharmacological characterization of five cloned voltage-gated K+ channels, types Kv1.1, 1.2, 1.3, 1.5, and 3.1, stably expressed in mammalian cell lines. *Mol Pharmacol, 45*(6), 1227-1234.

Gruget, C., Bello, O., Coleman, J., Krishnakumar, S. S., Perez, E., Rothman, J. E., . . . Donaldson, S. H., Jr. (2020). Synaptotagmin-1 membrane binding is driven by the C2B domain and assisted cooperatively by the C2A domain. *Sci Rep, 10*(1), 18011. doi:10.1038/s41598-020-74923-y

Gruget, C., Coleman, J., Bello, O., Krishnakumar, S. S., Perez, E., Rothman, J. E., . . . Donaldson, S. H., Jr. (2018). Rearrangements under confinement lead to increased binding energy of Synaptotagmin-1 with anionic membranes in Mg(2+) and Ca(2). *FEBS Lett, 592*(9), 1497-1506. doi:10.1002/1873-3468.13040

Guo, F., Wang, C. Y., Wang, S., Zhang, J., Yan, Y. J., Guan, Z. Y., & Meng, F. J. (2019). Alteration in gene expression profile of thymomas with or without myasthenia gravis linked with the nuclear factor-kappaB/autoimmune regulator pathway to myasthenia gravis pathogenesis. *Thorac Cancer, 10*(3), 564-570. doi:10.1111/1759-7714.12980

Gustavsson, N., & Han, W. (2009). Calcium-sensing beyond neurotransmitters: functions of synaptotagmins in neuroendocrine and endocrine secretion. *Biosci Rep, 29*(4), 245-259. doi:10.1042/BSR20090031

Han, X., Wang, C. T., Bai, J., Chapman, E. R., & Jackson, M. B. (2004). Transmembrane segments of syntaxin line the fusion pore of Ca2+-triggered exocytosis. *Science, 304*(5668), 289-292. doi:10.1126/science.1095801

Haroldsen, P. E., Garovoy, M. R., Musson, D. G., Zhou, H., Tsuruda, L., Hanson, B., & O'Neill, C. A. (2015a). Genetic variation in aryl N-acetyltransferase results in significant differences in the pharmacokinetic and safety profiles of amifampridine (3,4-diaminopyridine) phosphate. *Pharmacol Res Perspect, 3*(1), e00099. doi:10.1002/prp2.99

Haroldsen, P. E., Musson, D. G., Hanson, B., Quartel, A., & O'Neill, C. A. (2015b). Effects of Food Intake on the Relative Bioavailability of Amifampridine Phosphate Salt in Healthy Adults. *Clin Ther, 37*(7), 1555-1563. doi:10.1016/j.clinthera.2015.05.498

Hastings, W. (1970). Monte Carlo sampling methods using Markov chains and their applications. *Biometrika, 57,* 97-109.

Hayashi, T., McMahon, H., Yamasaki, S., Binz, T., Hata, Y., Sudhof, T. C., & Niemann, H. (1994). Synaptic vesicle membrane fusion complex: action of clostridial neurotoxins on assembly. *EMBO J, 13*(21), 5051-5061.

Hepburn, I., Chen, W., Wils, S., & De Schutter, E. (2012). STEPS: efficient simulation of stochastic reaction-diffusion models in realistic morphologies. *BMC Syst Biol, 6,* 36. doi:10.1186/1752-0509-6-36

Heredia, D. J., Schubert, D., Maligireddy, S., Hennig, G. W., & Gould, T. W. (2016). A Novel Striated Muscle-Specific Myosin-Blocking Drug for the Study of Neuromuscular Physiology. *Front Cell Neurosci, 10,* 276. doi:10.3389/fncel.2016.00276

Herrmann, D. N., Horvath, R., Sowden, J. E., Gonzalez, M., Sanchez-Mejias, A., Guan, Z., . . . Zuchner, S. (2014). Synaptotagmin 2 mutations cause an autosomal-dominant form of lambert-eaton myasthenic syndrome and nonprogressive motor neuropathy. *Am J Hum Genet, 95*(3), 332-339. doi:10.1016/j.ajhg.2014.08.007

Heuser, J. E., & Reese, T. S. (1981). Structural changes after transmitter release at the frog neuromuscular junction. *J Cell Biol, 88*(3), 564-580. doi:10.1083/jcb.88.3.564

Heuser, J. E., Reese, T. S., Dennis, M. J., Jan, Y., Jan, L., & Evans, L. (1979). Synaptic vesicle exocytosis captured by quick freezing and correlated with quantal transmitter release. *J Cell Biol, 81*(2), 275-300. doi:10.1083/jcb.81.2.275

Heuser, J. E., Reese, T. S., & Landis, D. M. (1974). Functional changes in frog neuromuscular junctions studied with freeze-fracture. *J Neurocytol, 3*(1), 109-131. doi:10.1007/BF01111936

Hines, M. L., & Carnevale, N. T. (1997). The NEURON simulation environment. *Neural Comput, 9*(6), 1179-1209. doi:10.1162/neco.1997.9.6.1179

Hines, M. L., & Carnevale, N. T. (2001). NEURON: a tool for neuroscientists. *Neuroscientist, 7*(2), 123-135. doi:10.1177/107385840100700207

Hoch, W., McConville, J., Helms, S., Newsom-Davis, J., Melms, A., & Vincent, A. (2001). Auto-antibodies to the receptor tyrosine kinase MuSK in patients with myasthenia gravis without acetylcholine receptor antibodies. *Nat Med, 7*(3), 365-368. doi:10.1038/85520

Hochbaum, D. R., Zhao, Y., Farhi, S. L., Klapoetke, N., Werley, C. A., Kapoor, V., . . . Cohen, A. E. (2014). All-optical electrophysiology in mammalian neurons using engineered microbial rhodopsins. *Nat Methods, 11*(8), 825-833. doi:10.1038/nmeth.3000

Hodgkin, A. L., & Huxley, A. F. (1939). Action Potentials Recorded from Inside a Nerve Fibre. *Nature, 144,* 710-711. doi:10.1038/144710a0

Hodgkin, A. L., & Huxley, A. F. (1945). Resting and action potentials in single nerve fibres. *J Physiol, 104*(2), 176-195. doi:10.1113/jphysiol.1945.sp004114

Hodgkin, A. L., & Huxley, A. F. (1952a). The components of membrane conductance in the giant axon of Loligo. *J Physiol, 116*(4), 473-496. doi:10.1113/jphysiol.1952.sp004718

Hodgkin, A. L., & Huxley, A. F. (1952b). Currents carried by sodium and potassium ions through the membrane of the giant axon of Loligo. *J Physiol, 116*(4), 449-472. doi:10.1113/jphysiol.1952.sp004717

Hodgkin, A. L., & Huxley, A. F. (1952c). The dual effect of membrane potential on sodium conductance in the giant axon of Loligo. *J Physiol, 116*(4), 497-506. doi:10.1113/jphysiol.1952.sp004719

Hodgkin, A. L., & Huxley, A. F. (1952d). Propagation of electrical signals along giant nerve fibers. *Proc R Soc Lond B Biol Sci, 140*(899), 177-183. doi:10.1098/rspb.1952.0054

Hodgkin, A. L., & Huxley, A. F. (1952e). A quantitative description of membrane current and its application to conduction and excitation in nerve. *J Physiol, 117*(4), 500-544. doi:10.1113/jphysiol.1952.sp004764

Hodgkin, A. L., Huxley, A. F., & Katz, B. (1952). Measurement of current-voltage relations in the membrane of the giant axon of Loligo. *J Physiol, 116*(4), 424-448. doi:10.1113/jphysiol.1952.sp004716

Hofer, G. F., Hohenthanner, K., Baumgartner, W., Groschner, K., Klugbauer, N., Hofmann, F., & Romanin, C. (1997). Intracellular Ca2+ inactivates L-type Ca2+ channels with a Hill coefficient of approximately 1 and an inhibition constant of approximately 4 microM by reducing channel's open probability. *Biophys J, 73*(4), 1857-1865. doi:10.1016/S0006-3495(97)78216-X

Homan, A. E., Laghaei, R., Dittrich, M., & Meriney, S. D. (2018). Impact of spatiotemporal calcium dynamics within presynaptic active zones on synaptic delay at the frog neuromuscular junction. *J Neurophysiol, 119*(2), 688-699. doi:10.1152/jn.00510.2017

Hoppa, M. B., Gouzer, G., Armbruster, M., & Ryan, T. A. (2014). Control and plasticity of the presynaptic action potential waveform at small CNS nerve terminals. *Neuron, 84*(4), 778-789. doi:10.1016/j.neuron.2014.09.038

Hu, H., Shao, L. R., Chavoshy, S., Gu, N., Trieb, M., Behrens, R., . . . Storm, J. F. (2001). Presynaptic Ca2+-activated K+ channels in glutamatergic hippocampal terminals and their role in spike repolarization and regulation of transmitter release. *J Neurosci, 21*(24), 9585-9597.

Huang, Y. L., Walker, A. S., & Miller, E. W. (2015). A Photostable Silicon Rhodamine Platform for Optical Voltage Sensing. *J Am Chem Soc, 137*(33), 10767-10776. doi:10.1021/jacs.5b06644

Hui, E., Bai, J., Wang, P., Sugimori, M., Llinas, R. R., & Chapman, E. R. (2005). Three distinct kinetic groupings of the synaptotagmin family: candidate sensors for rapid and delayed exocytosis. *Proc Natl Acad Sci U S A, 102*(14), 5210-5214. doi:10.1073/pnas.0500941102

Imredy, J. P., & Yue, D. T. (1994). Mechanism of Ca(2+)-sensitive inactivation of L-type Ca2+ channels. *Neuron, 12*(6), 1301-1318. doi:10.1016/0896-6273(94)90446-4

Ishida, N., Kobayashi, E., Kondo, Y., Matsushita, R., & Komai, K. (2015). Pharmacokinetics and safety of 3,4-diaminopyridine base in healthy Japanese volunteers. *Int J Clin Pharmacol Ther, 53*(8), 674-680. doi:10.5414/CP202133

Ishikawa, T., Nakamura, Y., Saitoh, N., Li, W. B., Iwasaki, S., & Takahashi, T. (2003). Distinct roles of Kv1 and Kv3 potassium channels at the calyx of Held presynaptic terminal. *J Neurosci, 23*(32), 10445-10453.

Jackman, S. L., & Regehr, W. G. (2017). The Mechanisms and Functions of Synaptic Facilitation. *Neuron, 94*(3), 447-464. doi:10.1016/j.neuron.2017.02.047

Jackman, S. L., Turecek, J., Belinsky, J. E., & Regehr, W. G. (2016). The calcium sensor synaptotagmin 7 is required for synaptic facilitation. *Nature, 529*(7584), 88-91. doi:10.1038/nature16507

Jan, Y. N., Jan, L. Y., & Dennis, M. J. (1977). Two mutations of synaptic transmission in Drosophila. *Proc R Soc Lond B Biol Sci, 198*(1130), 87-108. doi:10.1098/rspb.1977.0087

Johnston, I., Lang, B., Leys, K., & Newsom-Davis, J. (1994). Heterogeneity of calcium channel autoantibodies detected using a small-cell lung cancer line derived from a Lambert-Eaton myasthenic syndrome patient. *Neurology, 44*(2), 334-338. doi:10.1212/wnl.44.2.334

Kaczmarek, L. K., & Zhang, Y. (2017). Kv3 Channels: Enablers of Rapid Firing, Neurotransmitter Release, and Neuronal Endurance. *Physiol Rev, 97*(4), 1431-1468. doi:10.1152/physrev.00002.2017

Kaeser, P. S., Deng, L., Wang, Y., Dulubova, I., Liu, X., Rizo, J., & Sudhof, T. C. (2011). RIM proteins tether Ca2+ channels to presynaptic active zones via a direct PDZ-domain interaction. *Cell, 144*(2), 282-295. doi:10.1016/j.cell.2010.12.029

Kaeser, P. S., & Regehr, W. G. (2014). Molecular mechanisms for synchronous, asynchronous, and spontaneous neurotransmitter release. *Annu Rev Physiol, 76*, 333-363. doi:10.1146/annurev-physiol-021113-170338

Kalemkerian, G. P., Akerley, W., Bogner, P., Borghaei, H., Chow, L. Q., Downey, R. J., . . . National Comprehensive Cancer, N. (2013). Small cell lung cancer. *J Natl Compr Canc Netw, 11*(1), 78-98. doi:10.6004/jnccn.2013.0011

Katz, B., & Miledi, R. (1965a). The Measurement of Synaptic Delay, and the Time Course of Acetylcholine Release at the Neuromuscular Junction. *Proc R Soc Lond B Biol Sci, 161*, 483-495. doi:10.1098/rspb.1965.0016

Katz, B., & Miledi, R. (1965b). Propagation of Electric Activity in Motor Nerve Terminals. *Proc R Soc Lond B Biol Sci, 161*, 453-482. doi:10.1098/rspb.1965.0015

Katz, B., & Miledi, R. (1968). The effect of local blockage of motor nerve terminals. *J Physiol, 199*(3), 729-741. doi:10.1113/jphysiol.1968.sp008675

Katz, B., & Thesleff, S. (1957a). The interaction between edrophonium (tensilon) and acetylcholine at the motor end-plate. *Br J Pharmacol Chemother, 12*(2), 260-264. doi:10.1111/j.1476-5381.1957.tb00131.x

Katz, B., & Thesleff, S. (1957b). A study of the desensitization produced by acetylcholine at the motor end-plate. *J Physiol, 138*(1), 63-80. doi:10.1113/jphysiol.1957.sp005838

Katz, E., Ferro, P. A., Cherksey, B. D., Sugimori, M., Llinas, R., & Uchitel, O. D. (1995). Effects of Ca2+ channel blockers on transmitter release and presynaptic currents at the frog neuromuscular junction. *J Physiol, 486 (Pt 3)*, 695-706. doi:10.1113/jphysiol.1995.sp020845

Katz, E., Protti, D. A., Ferro, P. A., Rosato Siri, M. D., & Uchitel, O. D. (1997). Effects of Ca2+ channel blocker neurotoxins on transmitter release and presynaptic currents at the mouse neuromuscular junction. *Br J Pharmacol, 121*(8), 1531-1540. doi:10.1038/sj.bjp.0701290

Keogh, M., Sedehizadeh, S., & Maddison, P. (2011). Treatment for Lambert-Eaton myasthenic syndrome. *Cochrane Database Syst Rev*(2), CD003279. doi:10.1002/14651858.CD003279.pub3

Kerr, R. A., Bartol, T. M., Kaminsky, B., Dittrich, M., Chang, J. C., Baden, S. B., . . . Stiles, J. R. (2008). Fast Monte Carlo Simulation Methods for Biological Reaction-Diffusion Systems in Solution and on Surfaces. *SIAM J Sci Comput, 30*(6), 3126. doi:10.1137/070692017

Kesner, V. G., Oh, S. J., Dimachkie, M. M., & Barohn, R. J. (2018). Lambert-Eaton Myasthenic Syndrome. *Neurol Clin, 36*(2), 379-394. doi:10.1016/j.ncl.2018.01.008

Kirsch, G. E., & Drewe, J. A. (1993). Gating-dependent mechanism of 4-aminopyridine block in two related potassium channels. *J Gen Physiol, 102*(5), 797-816. doi:10.1085/jgp.102.5.797

Kirsch, G. E., & Narahashi, T. (1978). 3,4-diaminopyridine. A potent new potassium channel blocker. *Biophys J, 22*(3), 507-512. doi:10.1016/S0006-3495(78)85503-9

Komai, K., Iwasa, K., & Takamori, M. (1999). Calcium channel peptide can cause an autoimmune-mediated model of Lambert-Eaton myasthenic syndrome in rats. *J Neurol Sci, 166*(2), 126-130. doi:10.1016/s0022-510x(99)00125-2

Kshatri, A. S., Gonzalez-Hernandez, A., & Giraldez, T. (2018). Physiological Roles and Therapeutic Potential of Ca(2+) Activated Potassium Channels in the Nervous System. *Front Mol Neurosci, 11*, 258. doi:10.3389/fnmol.2018.00258

Kulkarni, R. U., & Miller, E. W. (2017). Voltage Imaging: Pitfalls and Potential. *Biochemistry, 56*(39), 5171-5177. doi:10.1021/acs.biochem.7b00490

Laghaei, R., Ma, J., Tarr, T. B., Homan, A. E., Kelly, L., Tilvawala, M. S., . . . Dittrich, M. (2018). Transmitter release site organization can predict synaptic function at the neuromuscular junction. *J Neurophysiol, 119*(4), 1340-1355. doi:10.1152/jn.00168.2017

Lambert, E. H., Eaton, L. M., & Rooke, E. D. (1956). Defect of neuromuscular conduction associated with malignant neoplasms. *American journal of physiology*(187), 612-613.

Lang, B., Molenaar, P. C., Newsom-Davis, J., & Vincent, A. (1984). Passive transfer of Lambert-Eaton myasthenic syndrome in mice: decreased rates of resting and evoked release of acetylcholine from skeletal muscle. *J Neurochem, 42*(3), 658-662. doi:10.1111/j.1471-4159.1984.tb02733.x

Lang, B., Newsom-Davis, J., Prior, C., & Wray, D. (1983). Antibodies to motor nerve terminals: an electrophysiological study of a human myasthenic syndrome transferred to mouse. *J Physiol, 344*(Nov; 344), 335-345. doi:10.1113/jphysiol.1983.sp014943

Lapicque, L. (2007). Quantitative investigations of electrical nerve excitation treated as polarization. 1907. *Biol Cybern, 97*(5-6), 341-349. doi:10.1007/s00422-007-0189-6

Leao, R. M., Kushmerick, C., Pinaud, R., Renden, R., Li, G. L., Taschenberger, H., . . . von Gersdorff, H. (2005). Presynaptic Na+ channels: locus, development, and recovery from inactivation at a high-fidelity synapse. *J Neurosci, 25*(14), 3724-3738. doi:10.1523/JNEUROSCI.3983-04.2005

Lee, A., Wong, S. T., Gallagher, D., Li, B., Storm, D. R., Scheuer, T., & Catterall, W. A. (1999). Ca2+/calmodulin binds to and modulates P/Q-type calcium channels. *Nature, 399*(6732), 155-159. doi:10.1038/20194

Lee, J., Ueda, A., & Wu, C. F. (2008). Pre- and post-synaptic mechanisms of synaptic strength homeostasis revealed by slowpoke and shaker K+ channel mutations in Drosophila. *Neuroscience, 154*(4), 1283-1296. doi:10.1016/j.neuroscience.2008.04.043

Lee, M. C., Hsiao, T. H., Chuang, H. N., Lee, L. W., Chi, P. L., Tsai, H. M., . . . Hsu, C. P. (2020). Molecular profiling of thymoma with myasthenia gravis: Risk factors of developing myasthenia gravis in thymoma patients. *Lung Cancer, 139*, 157-164. doi:10.1016/j.lungcan.2019.11.007

Lee, U. S., & Cui, J. (2010). BK channel activation: structural and functional insights. *Trends Neurosci, 33*(9), 415-423. doi:10.1016/j.tins.2010.06.004

Lemeignan, M., Millart, H., Lamiable, D., Molgo, J., & Lechat, P. (1984). Evaluation of 4-aminopyridine and 3,4-diaminopyridine penetrability into cerebrospinal fluid in anesthetized rats. *Brain Res, 304*(1), 166-169. doi:10.1016/0006-8993(84)90875-8

Lennon, V. A., Kryzer, T. J., Griesmann, G. E., O'Suilleabhain, P. E., Windebank, A. J., Woppmann, A., . . . Lambert, E. H. (1995). Calcium-channel antibodies in the Lambert-Eaton syndrome and other paraneoplastic syndromes. *N Engl J Med, 332*(22), 1467-1474. doi:10.1056/NEJM199506013322203

Li, F., Pincet, F., Perez, E., Eng, W. S., Melia, T. J., Rothman, J. E., & Tareste, D. (2007). Energetics and dynamics of SNAREpin folding across lipid bilayers. *Nat Struct Mol Biol, 14*(10), 890-896. doi:10.1038/nsmb1310

Li, L., Li, D. P., Chen, S. R., Chen, J., Hu, H., & Pan, H. L. (2014). Potentiation of high voltage-activated calcium channels by 4-aminopyridine depends on subunit composition. *Mol Pharmacol, 86*(6), 760-772. doi:10.1124/mol.114.095505

Lindgren, C. A., & Moore, J. W. (1989). Identification of ionic currents at presynaptic nerve endings of the lizard. *J Physiol, 414*, 201-222. doi:10.1113/jphysiol.1989.sp017684

Lindquist, S., & Stangel, M. (2011). Update on treatment options for Lambert-Eaton myasthenic syndrome: focus on use of amifampridine. *Neuropsychiatr Dis Treat, 7*, 341-349. doi:10.2147/NDT.S10464

Lindquist, S., & Stangel, M. (2014). 3,4-Diaminopyridine (amifampridine) for the treatment of Lambert–Eaton myasthenic syndrome. *Expert Opinion on Orphan Drugs, 2*(3), 293-300. doi:10.1517/21678707.2014.887464

Llinas, R., Steinberg, I. Z., & Walton, K. (1981). Relationship between presynaptic calcium current and postsynaptic potential in squid giant synapse. *Biophys J, 33*(3), 323-351. doi:10.1016/S0006-3495(81)84899-0

Lorenzoni, P. J., Scola, R. H., Kay, C. S. K., Werneck, L. C., Horvath, R., & Lochmuller, H. (2018). How to Spot Congenital Myasthenic Syndromes Resembling the Lambert-Eaton Myasthenic Syndrome? A Brief Review of Clinical, Electrophysiological, and Genetics Features. *Neuromolecular Med, 20*(2), 205-214. doi:10.1007/s12017-018-8490-1

Luneau, C. J., Williams, J. B., Marshall, J., Levitan, E. S., Oliva, C., Smith, J. S., . . . et al. (1991). Alternative splicing contributes to K+ channel diversity in the mammalian central nervous system. *Proc Natl Acad Sci U S A, 88*(9), 3932-3936. doi:10.1073/pnas.88.9.3932

Luo, F., Dittrich, M., Cho, S., Stiles, J. R., & Meriney, S. D. (2015). Transmitter release is evoked with low probability predominately by calcium flux through single channel openings at the frog neuromuscular junction. *J Neurophysiol, 113*(7), 2480-2489. doi:10.1152/jn.00879.2014

Luo, F., Dittrich, M., Stiles, J. R., & Meriney, S. D. (2011). Single-pixel optical fluctuation analysis of calcium channel function in active zones of motor nerve terminals. *J Neurosci, 31*(31), 11268-11281. doi:10.1523/JNEUROSCI.1394-11.2011

Luo, F., & Sudhof, T. C. (2017). Synaptotagmin-7-Mediated Asynchronous Release Boosts High-Fidelity Synchronous Transmission at a Central Synapse. *Neuron, 94*(4), 826-839 e823. doi:10.1016/j.neuron.2017.04.020

Ma, J., Kelly, L., Ingram, J., Price, T. J., Meriney, S. D., & Dittrich, M. (2014). New insights into short-term synaptic facilitation at the frog neuromuscular junction. *J Neurophysiol, 113*, 16.

MacDougall, D. D., Lin, Z., Chon, N. L., Jackman, S. L., Lin, H., Knight, J. D., & Anantharam, A. (2018). The high-affinity calcium sensor synaptotagmin-7 serves multiple roles in regulated exocytosis. *J Gen Physiol, 150*(6), 783-807. doi:10.1085/jgp.201711944

Maddison, P. (2012). Treatment in Lambert-Eaton myasthenic syndrome. *Ann N Y Acad Sci, 1275*, 78-84. doi:10.1111/j.1749-6632.2012.06769.x

Maddison, P., Lang, B., Mills, K., & Newsom-Davis, J. (2001). Long term outcome in Lambert-Eaton myasthenic syndrome without lung cancer. *J Neurol Neurosurg Psychiatry, 70*(2), 212-217. doi:10.1136/jnnp.70.2.212

Maddison, P., McConville, J., Farrugia, M. E., Davies, N., Rose, M., Norwood, F., . . . Hilton-Jones, D. (2011). The use of rituximab in myasthenia gravis and Lambert-Eaton myasthenic syndrome. *J Neurol Neurosurg Psychiatry, 82*(6), 671-673. doi:10.1136/jnnp.2009.197632

Maddison, P., Newsom-Davis, J., Mills, K. R., & Souhami, R. L. (1999). Favourable prognosis in Lambert-Eaton myasthenic syndrome and small-cell lung carcinoma. *Lancet, 353*(9147), 117-118. doi:10.1016/S0140-6736(05)76153-5

Mainero, C., Inghilleri, M., Pantano, P., Conte, A., Lenzi, D., Frasca, V., . . . Pozzilli, C. (2004). Enhanced brain motor activity in patients with MS after a single dose of 3,4-diaminopyridine. *Neurology, 62*(11), 2044-2050. doi:10.1212/01.wnl.0000129263.14219.a8

Mallart, A. (1984). Presynaptic currents in frog motor endings. *Pflugers Arch, 400*(1), 8-13. doi:10.1007/BF00670529

Maric, D., Maric, I., Smith, S. V., Serafini, R., Hu, Q., & Barker, J. L. (1998). Potentiometric study of resting potential, contributing K+ channels and the onset of Na+ channel excitability in embryonic rat cortical cells. *Eur J Neurosci, 10*(8), 2532-2546. doi:10.1046/j.1460-9568.1998.00284.x

Martens, S., Kozlov, M. M., & McMahon, H. T. (2007). How synaptotagmin promotes membrane fusion. *Science, 316*(5828), 1205-1208. doi:10.1126/science.1142614

Martin-Moutot, N., De Haro, L., & Seagar, M. (2008). Distinct evolution of calcium channel antibody types in Lambert-Eaton myasthenic syndrome. *J Neuroimmunol, 197*(1), 47-53. doi:10.1016/j.jneuroim.2008.04.001

Martina, M., Metz, A. E., & Bean, B. P. (2007). Voltage-dependent potassium currents during fast spikes of rat cerebellar Purkinje neurons: inhibition by BDS-I toxin. *J Neurophysiol, 97*(1), 563-571. doi:10.1152/jn.00269.2006

Martina, M., Schultz, J. H., Ehmke, H., Monyer, H., & Jonas, P. (1998). Functional and molecular differences between voltage-gated K+ channels of fast-spiking interneurons and pyramidal neurons of rat hippocampus. *J Neurosci, 18*(20), 8111-8125.

Martina, M., Yao, G. L., & Bean, B. P. (2003). Properties and functional role of voltage-dependent potassium channels in dendrites of rat cerebellar Purkinje neurons. *J Neurosci, 23*(13), 5698-5707.

Maselli, R. A., Ng, J. J., Anderson, J. A., Cagney, O., Arredondo, J., Williams, C., . . . Wollmann, R. L. (2009). Mutations in LAMB2 causing a severe form of synaptic congenital myasthenic syndrome. *J Med Genet, 46*(3), 203-208. doi:10.1136/jmg.2008.063693

Matveev, V., Bertram, R., & Sherman, A. (2011). Calcium cooperativity of exocytosis as a measure of Ca(2)+ channel domain overlap. *Brain Res, 1398*, 126-138. doi:10.1016/j.brainres.2011.05.011

McKay, B. E., & Turner, R. W. (2004). Kv3 K+ channels enable burst output in rat cerebellar Purkinje cells. *Eur J Neurosci, 20*(3), 729-739. doi:10.1111/j.1460-9568.2004.03539.x

McLachlan, E. M., & Martin, A. R. (1981). Non-linear summation of end-plate potentials in the frog and mouse. *J Physiol, 311*, 307-324. doi:10.1113/jphysiol.1981.sp013586

Melom, J. E., Akbergenova, Y., Gavornik, J. P., & Littleton, J. T. (2013). Spontaneous and evoked release are independently regulated at individual active zones. *J Neurosci, 33*(44), 17253-17263. doi:10.1523/JNEUROSCI.3334-13.2013

Meriney, S. D., & Dittrich, M. (2013). Organization and function of transmitter release sites at the neuromuscular junction. *J Physiol, 591*(13), 3159-3165. doi:10.1113/jphysiol.2012.248625

Meriney, S. D., Hulsizer, S. C., Lennon, V. A., & Grinnell, A. D. (1996). Lambert-Eaton myasthenic syndrome immunoglobulins react with multiple types of calcium channels in small-cell lung carcinoma. *Ann Neurol, 40*(5), 739-749. doi:10.1002/ana.410400510

Meriney, S. D., & Lacomis, D. (2018). Reported direct aminopyridine effects on voltage-gated calcium channels is a high-dose pharmacological off-target effect of no clinical relevance. *Journal of Biological Chemistry, 293*(41), 16100-16100. doi:10.1074/jbc.L118.005425 PMID - 30315087

Metropolis, N., Rosenbluth, A., Rosenbluth, M., Teller, A., & Teller, E. (1953). Equations of state calculations by fast computing machines. *J Chem Phys, 21*, 1087-1092.

Meunier, F. M. (1984). Relationship between presynaptic membrane potential and acetylcholine release in synaptosomes from Torpedo electric organ. *J Physiol, 354*, 121-137. doi:10.1113/jphysiol.1984.sp015367

Miesenbock, G., De Angelis, D. A., & Rothman, J. E. (1998). Visualizing secretion and synaptic transmission with pH-sensitive green fluorescent proteins. *Nature, 394*(6689), 192-195. doi:10.1038/28190

Miller, E. W. (2016). Small molecule fluorescent voltage indicators for studying membrane potential. *Curr Opin Chem Biol, 33*, 74-80. doi:10.1016/j.cbpa.2016.06.003

Mintz, I. M., Venema, V. J., Swiderek, K. M., Lee, T. D., Bean, B. P., & Adams, M. E. (1992). P-type calcium channels blocked by the spider toxin omega-Aga-IVA. *Nature, 355*(6363), 827-829. doi:10.1038/355827a0

Miralles, F., & Solsona, C. (1996). Activity-dependent modulation of the presynaptic potassium current in the frog neuromuscular junction. *J Physiol, 495 (Pt 3)*, 717-732. doi:10.1113/jphysiol.1996.sp021628

Mochida, S., Westenbroek, R. E., Yokoyama, C. T., Zhong, H., Myers, S. J., Scheuer, T., . . . Catterall, W. A. (2003). Requirement for the synaptic protein interaction site for reconstitution of synaptic transmission by P/Q-type calcium channels. *Proc Natl Acad Sci U S A, 100*(5), 2819-2824. doi:10.1073/pnas.262787699

Molgó, J., Lundh, H., & Thesleff, S. (1980). Potency of 3,4-diaminopyridine and 4-aminopyridine on mammalian neuromuscular transmission and the effect of pH changes. *Eur J Pharmacol, 6*(1), 25-34. doi:doi:10.1016/0014-2999(80)90378-7

Motomura, M., Lang, B., Johnston, I., Palace, J., Vincent, A., & Newsom-Davis, J. (1997). Incidence of serum anti-P/O-type and anti-N-type calcium channel autoantibodies in the Lambert-Eaton myasthenic syndrome. *J Neurol Sci, 147*(1), 35-42. doi:10.1016/s0022-510x(96)05303-8

Muqeem, T., Ghosh, B., Pinto, V., Lepore, A. C., & Covarrubias, M. (2018). Regulation of Nociceptive Glutamatergic Signaling by Presynaptic Kv3.4 Channels in the Rat Spinal Dorsal Horn. *J Neurosci, 38*(15), 3729-3740. doi:10.1523/JNEUROSCI.3212-17.2018

Nagel, A., Engel, A. G., Lang, B., Newsom-Davis, J., & Fukuoka, T. (1988). Lambert-Eaton myasthenic syndrome IgG depletes presynaptic membrane active zone particles by antigenic modulation. *Ann Neurol, 24*(4), 552-558. doi:10.1002/ana.410240412

Nagwaney, S., Harlow, M. L., Jung, J. H., Szule, J. A., Ress, D., Xu, J., . . . McMahan, U. J. (2009). Macromolecular connections of active zone material to docked synaptic vesicles and presynaptic membrane at neuromuscular junctions of mouse. *J Comp Neurol, 513*(5), 457-468. doi:10.1002/cne.21975

Nakamura, Y., Harada, H., Kamasawa, N., Matsui, K., Rothman, J. S., Shigemoto, R., . . . Takahashi, T. (2015). Nanoscale distribution of presynaptic Ca(2+) channels and its impact on vesicular release during development. *Neuron, 85*(1), 145-158. doi:10.1016/j.neuron.2014.11.019

Nakamura, Y., & Takahashi, T. (2007). Developmental changes in potassium currents at the rat calyx of Held presynaptic terminal. *J Physiol, 581*(Pt 3), 1101-1112. doi:10.1113/jphysiol.2007.128702

Nakao, Y. K., Motomura, M., Fukudome, T., Fukuda, T., Shiraishi, H., Yoshimura, T., . . . Eguchi, K. (2002). Seronegative Lambert-Eaton myasthenic syndrome: study of 110 Japanese patients. *Neurology, 59*(11), 1773-1775. doi:10.1212/01.wnl.0000037485.56217.5f

Natera-de Benito, D., Bestue, M., Vilchez, J. J., Evangelista, T., Topf, A., Garcia-Ribes, A., . . . Nascimento, A. (2016a). Long-term follow-up in patients with congenital myasthenic syndrome due to RAPSN mutations. *Neuromuscul Disord, 26*(2), 153-159. doi:10.1016/j.nmd.2015.10.013

Natera-de Benito, D., Dominguez-Carral, J., Muelas, N., Nascimento, A., Ortez, C., Jaijo, T., . . . Vilchez, J. J. (2016b). Phenotypic heterogeneity in two large Roma families with a congenital myasthenic syndrome due to CHRNE 1267delG mutation. A long-term follow-up. *Neuromuscul Disord, 26*(11), 789-795. doi:10.1016/j.nmd.2016.08.005

Neher, E., & Sakaba, T. (2008). Multiple roles of calcium ions in the regulation of neurotransmitter release. *Neuron, 59*(6), 861-872. doi:10.1016/j.neuron.2008.08.019

Newcomb, R., Szoke, B., Palma, A., Wang, G., Chen, X., Hopkins, W., . . . Miljanich, G. (1998). Selective peptide antagonist of the class E calcium channel from the venom of the tarantula Hysterocrates gigas. *Biochemistry, 37*(44), 15353-15362. doi:10.1021/bi981255g

Newsom-Davis, J. (1998). A treatment algorithm for Lambert-Eaton myasthenic syndrome. *Ann N Y Acad Sci, 841*, 817-822. doi:10.1111/j.1749-6632.1998.tb11023.x

Newsom-Davis, J. (2003). Therapy in myasthenia gravis and Lambert-Eaton myasthenic syndrome. *Semin Neurol, 23*(2), 191-198. doi:10.1055/s-2003-41135

Newsom-Davis, J., & Murray, N. M. (1984). Plasma exchange and immunosuppressive drug treatment in the Lambert-Eaton myasthenic syndrome. *Neurology, 34*(4), 480-485. doi:10.1212/wnl.34.4.480

Nikol'kii, E. E., Bukharaeva, E. A., Samigullin, D. V., & Gainulo, R. (2002). Characteristics of the time course of evoked secretion of transmitter quanta in different parts of the motor nerve ending in the frog. *Neurosci Behav Physiol, 32*(3), 265-274. doi:10.1023/a:1015010307181

Nishimune, H., Badawi, Y., Mori, S., & Shigemoto, K. (2016). Dual-color STED microscopy reveals a sandwich structure of Bassoon and Piccolo in active zones of adult and aged mice. *Sci Rep, 6*, 27935. doi:10.1038/srep27935

Nishimune, H., Sanes, J. R., & Carlson, S. S. (2004). A synaptic laminin-calcium channel interaction organizes active zones in motor nerve terminals. *Nature, 432*(7017), 580-587. doi:10.1038/nature03112

Oh, S. J. (2016). Myasthenia gravis Lambert-Eaton overlap syndrome. *Muscle Nerve, 53*(1), 20-26. doi:10.1002/mus.24921

Oh, S. J. (2020). Amifampridine to treat Lambert-Eaton myasthenic syndrome. *Drugs Today (Barc), 56*(10), 623-641. doi:10.1358/dot.2020.56.10.3137144

Oh, S. J., Hatanaka, Y., Claussen, G. C., & Sher, E. (2007). Electrophysiological differences in seropositive and seronegative Lambert-Eaton myasthenic syndrome. *Muscle Nerve, 35*(2), 178-183. doi:10.1002/mus.20672

Ojala, K. S., Ginebaugh, S. P., Wu, M., Miller, E. W., Ortiz, G., Covarrubias, M., & Meriney, S. D. (2021). A high affinity, partial antagonist effect of 3,4-diaminopyridine mediates action potential broadening and enhancement of transmitter release at NMJs. *J Biol Chem*, 100302. doi:10.1016/j.jbc.2021.100302

Olivera, B. M., Miljanich, G. P., Ramachandran, J., & Adams, M. E. (1994). Calcium channel diversity and neurotransmitter release: the omega-conotoxins and omega-agatoxins. *Annu Rev Biochem, 63*, 823-867. doi:10.1146/annurev.bi.63.070194.004135

Otsu, N. (1979). A Threshold Selection Method from Gray-Level Histograms. *IEEE Transactions on Systems, Man, and Cybernetic*, *9*(1), 62-66. doi:10.1109/TSMC.1979.4310076

Ovsepian, S. V., & Vesselkin, N. P. (2006). Serotonergic modulation of synaptic transmission and action potential firing in frog motoneurons. *Brain Res, 1102*(1), 71-77. doi:10.1016/j.brainres.2006.04.035

Pancrazio, J. J., Viglione, M. P., & Kim, Y. I. (1989). Effects of Bay K 8644 on spontaneous and evoked transmitter release at the mouse neuromuscular junction. *Neuroscience, 30*(1), 215-221. doi:10.1016/0306-4522(89)90366-7

Pang, Z. P., Melicoff, E., Padgett, D., Liu, Y., Teich, A. F., Dickey, B. F., . . . Sudhof, T. C. (2006a). Synaptotagmin-2 is essential for survival and contributes to Ca2+ triggering of neurotransmitter release in central and neuromuscular synapses. *J Neurosci, 26*(52), 13493-13504. doi:10.1523/JNEUROSCI.3519-06.2006

Pang, Z. P., Sun, J., Rizo, J., Maximov, A., & Sudhof, T. C. (2006b). Genetic analysis of synaptotagmin 2 in spontaneous and Ca2+-triggered neurotransmitter release. *EMBO J, 25*(10), 2039-2050. doi:10.1038/sj.emboj.7601103

Park, K. H., Jung, J., Lee, J. H., & Hong, Y. H. (2016). Blood Transcriptome Profiling in Myasthenia Gravis Patients to Assess Disease Activity: A Pilot RNA-seq Study. *Exp Neurobiol, 25*(1), 40-47. doi:10.5607/en.2016.25.1.40

Parsons, K. T., & Kwok, W. W. (2002). Linear B-cell epitopes in Lambert-Eaton myasthenic syndrome defined by cell-free synthetic peptide binding. *J Neuroimmunol, 126*(1-2), 190-195. doi:10.1016/s0165-5728(02)00063-2

Pattillo, J. M., Artim, D. E., Simples, J. E., Jr., & Meriney, S. D. (1999). Variations in onset of action potential broadening: effects on calcium current studied in chick ciliary ganglion neurones. *J Physiol, 514 (Pt 3)*, 719-728. doi:10.1111/j.1469-7793.1999.719ad.x

Pattillo, J. M., Yazejian, B., DiGregorio, D. A., Vergara, J. L., Grinnell, A. D., & Meriney, S. D. (2001). Contribution of presynaptic calcium-activated potassium currents to transmitter release regulation in cultured Xenopus nerve-muscle synapses. *Neuroscience, 102*(1), 229-240. doi:10.1016/s0306-4522(00)00453-x

Pawson, P. A., Grinnell, A. D., & Wolowske, B. (1998a). Quantitative freeze-fracture analysis of the frog neuromuscular junction synapse--I. Naturally occurring variability in active zone structure. *J Neurocytol, 27*(5), 361-377. doi:10.1023/a:1006942909544

Pawson, P. A., Grinnell, A. D., & Wolowske, B. (1998b). Quantitative freeze-fracture analysis of the frog neuromuscular junction synapse--II. Proximal-distal measurements. *J Neurocytol, 27*(5), 379-391. doi:10.1023/a:1006995010453

Peled, E. S., & Isacoff, E. Y. (2011). Optical quantal analysis of synaptic transmission in wild-type and rab3-mutant Drosophila motor axons. *Nat Neurosci, 14*(4), 519-526. doi:10.1038/nn.2767

Pellkofer, H. L., Voltz, R., & Kuempfel, T. (2009). Favorable response to rituximab in a patient with anti-VGCC-positive Lambert-Eaton myasthenic syndrome and cerebellar dysfunction. *Muscle Nerve, 40*(2), 305-308. doi:10.1002/mus.21315

Peper, K., Dreyer, F., Sandri, C., Akert, K., & Moor, H. (1974). Structure and ultrastructure of the frog motor endplate. A freeze-etching study. *Cell Tissue Res, 149*(4), 437-455. doi:10.1007/BF00223024

Peterka, D. S., Takahashi, H., & Yuste, R. (2011). Imaging voltage in neurons. *Neuron, 69*(1), 9-21. doi:10.1016/j.neuron.2010.12.010

Pfenninger, K., Akert, K., Moor, H., & Sandri, C. (1972). The fine structure of freeze-fractured presynaptic membranes. *J Neurocytol, 1*(2), 129-149. doi:10.1007/BF01099180

Podleski, T., & Changeux, J. P. (1969). Effects associated with permeability changes caused by gramicidin A in electroplax membrane. *Nature, 221*(5180), 541-545. doi:10.1038/221541a0

Polman, C. H., Bertelsmann, F. W., van Loenen, A. C., & Koetsier, J. C. (1994). 4-Aminopyridine in the Treatment of Patients With Multiple Sclerosis: Long-term Efficacy and Safety. *Archives of Neurology, 51*(3), 292-296. doi:10.1001/archneur.1994.00540150090022

Popovic, M. A., Foust, A. J., McCormick, D. A., & Zecevic, D. (2011). The spatio-temporal characteristics of action potential initiation in layer 5 pyramidal neurons: a voltage imaging study. *J Physiol, 589*(17), 4167-4187. doi:10.1113/jphysiol.2011.209015

Preibisch, S., Saalfeld, S., & Tomancak, P. (2009). Globally optimal stitching of tiled 3D microscopic image acquisitions. *Bioinformatics, 25*(11), 1463-1465. doi:10.1093/bioinformatics/btp184

Pumplin, D. W., Reese, T. S., & Llinas, R. (1981). Are the presynaptic membrane particles the calcium channels? *Proc Natl Acad Sci U S A, 78*(11), 7210-7213. doi:10.1073/pnas.78.11.7210

Rettig, J., Wunder, F., Stocker, M., Lichtinghagen, R., Mastiaux, F., Beckh, S., . . . et al. (1992). Characterization of a Shaw-related potassium channel family in rat brain. *EMBO J, 11*(7), 2473-2486.

Reuter, H. (1979). Properties of two inward membrane currents in the heart. *Annu Rev Physiol, 41*, 413-424. doi:10.1146/annurev.ph.41.030179.002213

Rizo, J., & Rosenmund, C. (2008). Synaptic vesicle fusion. *Nat Struct Mol Biol, 15*(7), 665-674. doi:10.1038/nsmb.1450

Roberts, A., Perera, S., Lang, B., Vincent, A., & Newsom-Davis, J. (1985). Paraneoplastic myasthenic syndrome IgG inhibits 45Ca2+ flux in a human small cell carcinoma line. *Nature, 317*(6039), 737-739. doi:10.1038/317737a0

Robitaille, R., Adler, E. M., & Charlton, M. P. (1990). Strategic location of calcium channels at transmitter release sites of frog neuromuscular synapses. *Neuron, 5*(6), 773-779. doi:10.1016/0896-6273(90)90336-e

Robitaille, R., Adler, E. M., & Charlton, M. P. (1993a). Calcium channels and calcium-gated potassium channels at the frog neuromuscular junction. *J Physiol Paris, 87*(1), 15-24. doi:10.1016/0928-4257(93)90020-t

Robitaille, R., & Charlton, M. P. (1992). Presynaptic calcium signals and transmitter release are modulated by calcium-activated potassium channels. *J Neurosci, 12*(1), 297-305.

Robitaille, R., Garcia, M. L., Kaczorowski, G. J., & Charlton, M. P. (1993b). Functional colocalization of calcium and calcium-gated potassium channels in control of transmitter release. *Neuron, 11*(4), 645-655. doi:10.1016/0896-6273(93)90076-4

Robitaille, R., & Tremblay, J. P. (1987). Non-uniform release at the frog neuromuscular junction: evidence of morphological and physiological plasticity. *Brain Res, 434*(1), 95-116. doi:10.1016/0165-0173(87)90019-1

Rodríguez Cruz, P. M., Belaya, K., Basiri, K., Sedghi, M., Farrugia, M. E., Holton, J. L., . . . Beeson, D. (2016). Clinical features of the myasthenic syndrome arising from mutations in GMPPB. *Journal of Neurology, Neurosurgery & Psychiatry, 87*(8), 802-809. doi:10.1136/jnnp-2016-313163

Rodríguez Cruz, P. M., Cossins, J., de Paula Estephan, E., Munell, F., Selby, K., Hirano, M., . . . Beeson, D. (2019). The clinical spectrum of the congenital myasthenic syndrome resulting from COL13A1 mutations. *Brain, 142*(6), 1547-1560. doi:10.1093/brain/awz107

Rodriguez Cruz, P. M., Palace, J., & Beeson, D. (2018). The Neuromuscular Junction and Wide Heterogeneity of Congenital Myasthenic Syndromes. *Int J Mol Sci, 19*(6). doi:10.3390/ijms19061677

Rogers, R. S., & Nishimune, H. (2017). The role of laminins in the organization and function of neuromuscular junctions. *Matrix Biol, 57-58*, 86-105. doi:10.1016/j.matbio.2016.08.008

Rosenthal, J. J., & Bezanilla, F. (2000). Seasonal variation in conduction velocity of action potentials in squid giant axons. *Biol Bull, 199*(2), 135-143. doi:10.2307/1542873

Rosenthal, J. J., Vickery, R. G., & Gilly, W. F. (1996). Molecular identification of SqKv1A. A candidate for the delayed rectifier K channel in squid giant axon. *J Gen Physiol, 108*(3), 207-219. doi:10.1085/jgp.108.3.207

Rowan, M. J., DelCanto, G., Yu, J. J., Kamasawa, N., & Christie, J. M. (2016). Synapse-Level Determination of Action Potential Duration by K(+) Channel Clustering in Axons. *Neuron, 91*(2), 370-383. doi:10.1016/j.neuron.2016.05.035

Rowan, M. J., Tranquil, E., & Christie, J. M. (2014). Distinct Kv channel subtypes contribute to differences in spike signaling properties in the axon initial segment and presynaptic boutons of cerebellar interneurons. *J Neurosci, 34*(19), 6611-6623. doi:10.1523/JNEUROSCI.4208-13.2014

Rowan, M. J. M., & Christie, J. M. (2017). Rapid State-Dependent Alteration in Kv3 Channel Availability Drives Flexible Synaptic Signaling Dependent on Somatic Subthreshold Depolarization. *Cell Rep, 18*(8), 2018-2029. doi:10.1016/j.celrep.2017.01.068

Rudy, B., & McBain, C. J. (2001). Kv3 channels: voltage-gated K+ channels designed for high-frequency repetitive firing. *Trends Neurosci, 24*(9), 517-526. doi:10.1016/s0166-2236(00)01892-0

Ruiz, R., Cano, R., Casanas, J. J., Gaffield, M. A., Betz, W. J., & Tabares, L. (2011). Active zones and the readily releasable pool of synaptic vesicles at the neuromuscular junction of the mouse. *J Neurosci, 31*(6), 2000-2008. doi:10.1523/JNEUROSCI.4663-10.2011

Sabatini, B. L., & Regehr, W. G. (1996). Timing of neurotransmission at fast synapses in the mammalian brain. *Nature, 384*(6605), 170-172. doi:10.1038/384170a0

Sabatini, B. L., & Regehr, W. G. (1997). Control of neurotransmitter release by presynaptic waveform at the granule cell to Purkinje cell synapse. *J Neurosci, 17*(10), 3425-3435.

Sakaba, T., & Neher, E. (2001). Preferential potentiation of fast-releasing synaptic vesicles by cAMP at the calyx of Held. *Proc Natl Acad Sci U S A, 98*(1), 331-336. doi:10.1073/pnas.021541098

Sakaba, T., & Neher, E. (2003). Involvement of actin polymerization in vesicle recruitment at the calyx of Held synapse. *J Neurosci, 23*(3), 837-846.

Sanders, D. B. (1998). 3,4-Diaminopyridine (DAP) in the treatment of Lambert-Eaton myasthenic syndrome (LEMS). *Ann N Y Acad Sci, 841*(1), 811-816. doi:10.1111/j.1749-6632.1998.tb11022.x

Sanders, D. B., Juel, V. C., Harati, Y., Smith, A. G., Peltier, A. C., Marburger, T., . . . Dapper Study, T. (2018). 3,4-diaminopyridine base effectively treats the weakness of Lambert-Eaton myasthenia. *Muscle Nerve, 57*(4), 561-568. doi:10.1002/mus.26052

Sanders, D. B., Massey, J. M., Sanders, L. L., & Edwards, L. J. (2000). A randomized trial of 3,4-diaminopyridine in Lambert-Eaton myasthenic syndrome. *Neurology, 54*(3), 603-607. doi:10.1212/wnl.54.3.603

Santafe, M. M., Lanuza, M. A., Garcia, N., & Tomas, J. (2006). Muscarinic autoreceptors modulate transmitter release through protein kinase C and protein kinase A in the rat motor nerve terminal. *Eur J Neurosci, 23*(8), 2048-2056. doi:10.1111/j.1460-9568.2006.04753.x

Santafe, M. M., Salon, I., Garcia, N., Lanuza, M. A., Uchitel, O. D., & Tomas, J. (2003). Modulation of ACh release by presynaptic muscarinic autoreceptors in the neuromuscular junction of the newborn and adult rat. *Eur J Neurosci, 17*(1), 119-127. doi:10.1046/j.1460-9568.2003.02428.x

Schaarschmidt, G., Wegner, F., Schwarz, S. C., Schmidt, H., & Schwarz, J. (2009). Characterization of voltage-gated potassium channels in human neural progenitor cells. *PLoS One, 4*(7), e6168. doi:10.1371/journal.pone.0006168

Schoser, B., Eymard, B., Datt, J., & Mantegazza, R. (2017). Lambert-Eaton myasthenic syndrome (LEMS): a rare autoimmune presynaptic disorder often associated with cancer. *J Neurol, 264*(9), 1854-1863. doi:10.1007/s00415-017-8541-9

Sclip, A., Acuna, C., Luo, F., & Sudhof, T. C. (2018). RIM-binding proteins recruit BK-channels to presynaptic release sites adjacent to voltage-gated Ca(2+)-channels. *EMBO J, 37*(16). doi:10.15252/embj.201798637

Sheean, G. L., Murray, N. M., Rothwell, J. C., Miller, D. H., & Thompson, A. J. (1998). An open-labelled clinical and electrophysiological study of 3,4 diaminopyridine in the treatment of fatigue in multiple sclerosis. *Brain, 121 (Pt 5)*(5), 967-975. doi:10.1093/brain/121.5.967

Sheng, J., He, L., Zheng, H., Xue, L., Luo, F., Shin, W., . . . Wu, L. G. (2012). Calcium-channel number critically influences synaptic strength and plasticity at the active zone. *Nat Neurosci, 15*(7), 998-1006. doi:10.1038/nn.3129

Sheng, Z. H., Westenbroek, R. E., & Catterall, W. A. (1998). Physical link and functional coupling of presynaptic calcium channels and the synaptic vesicle docking/fusion machinery. *J Bioenerg Biomembr, 30*(4), 335-345. doi:10.1023/a:1021985521748

Shieh, P., Sharma, K., Kohrman, B., & Oh, S. J. (2019). Amifampridine Phosphate (Firdapse) Is Effective in a Confirmatory Phase 3 Clinical Trial in LEMS. *Journal of clinical neuromuscular disease, 20*(3), 111-119. doi:10.1097/CND.0000000000000239

Skeie, G. O., Apostolski, S., Evoli, A., Gilhus, N. E., Illa, I., Harms, L., . . . European Federation of Neurological, S. (2010). Guidelines for treatment of autoimmune neuromuscular transmission disorders. *Eur J Neurol, 17*(7), 893-902. doi:10.1111/j.1468-1331.2010.03019.x

Slater, C. R. (2015). The functional organization of motor nerve terminals. *Prog Neurobiol, 134*, 55-103. doi:10.1016/j.pneurobio.2015.09.004

Smith, C. C., & Brownstone, R. M. (2020). Spinal motoneuron firing properties mature from rostral to caudal during postnatal development of the mouse. *J Physiol, 598*(23), 5467-5485. doi:10.1113/JP280274

Smith, D. O., Conklin, M. W., Jensen, P. J., & Atchison, W. D. (1995). Decreased calcium currents in motor nerve terminals of mice with Lambert-Eaton myasthenic syndrome. *J Physiol, 487*(1), 115-123. doi:10.1113/jphysiol.1995.sp020865

Snutch, T. P., & Reiner, P. B. (1992). Ca2+ channels: diversity of form and function. *Curr Opin Neurobiol, 2*(3), 247-253. doi:10.1016/0959-4388(92)90111-w

Sollner, T., Whiteheart, S. W., Brunner, M., Erdjument-Bromage, H., Geromanos, S., Tempst, P., & Rothman, J. E. (1993). SNAP receptors implicated in vesicle targeting and fusion. *Nature, 362*(6418), 318-324. doi:10.1038/362318a0

Sosa, M. A., & Zengel, J. E. (1993). Use of mu-conotoxin GIIIA for the study of synaptic transmission at the frog neuromuscular junction. *Neurosci Lett, 157*(2), 235-238. doi:10.1016/0304-3940(93)90745-7

Southan, A. P., & Robertson, B. (2000). Electrophysiological characterization of voltage-gated K(+) currents in cerebellar basket and purkinje cells: Kv1 and Kv3 channel subfamilies are present in basket cell nerve terminals. *J Neurosci, 20*(1), 114-122.

Stanley, E. F. (2016). The Nanophysiology of Fast Transmitter Release. *Trends Neurosci, 39*(3), 183-197. doi:10.1016/j.tins.2016.01.005

Stefan, M. I., Bartol, T. M., Sejnowski, T. J., & Kennedy, M. B. (2014). Multi-state modeling of biomolecules. *PLoS Comput Biol, 10*(9), e1003844. doi:10.1371/journal.pcbi.1003844

Stephens, G. J., Garratt, J. C., Robertson, B., & Owen, D. G. (1994). On the mechanism of 4-aminopyridine action on the cloned mouse brain potassium channel mKv1.1. *J Physiol, 477*(Pt 2), 187-196. doi:10.1113/jphysiol.1994.sp020183

Stergiou, C., Lazaridis, K., Zouvelou, V., Tzartos, J., Mantegazza, R., Antozzi, C., . . . Tzartos, S. J. (2016). Titin antibodies in "seronegative" myasthenia gravis--A new role for an old antigen. *J Neuroimmunol, 292*, 108-115. doi:10.1016/j.jneuroim.2016.01.018

Stiles, J. R., Van Helden, D., Bartol, T. M., Jr., Salpeter, E. E., & Salpeter, M. M. (1996). Miniature endplate current rise times less than 100 microseconds from improved dual recordings can be modeled with passive acetylcholine diffusion from a synaptic vesicle. *Proc Natl Acad Sci U S A, 93*(12), 5747-5752. doi:10.1073/pnas.93.12.5747

Strupp, M., Teufel, J., Zwergal, A., Schniepp, R., Khodakhah, K., & Feil, K. (2017). Aminopyridines for the treatment of neurologic disorders. *Neurol Clin Pract, 7*(1), 65-76. doi:10.1212/CPJ.0000000000000321

Sudhof, T. C. (2012). The presynaptic active zone. *Neuron, 75*(1), 11-25. doi:10.1016/j.neuron.2012.06.012

Sudhof, T. C. (2013). A molecular machine for neurotransmitter release: synaptotagmin and beyond. *Nat Med, 19*(10), 1227-1231. doi:10.1038/nm.3338

Sun, X. P., Yazejian, B., & Grinnell, A. D. (2004). Electrophysiological properties of BK channels in Xenopus motor nerve terminals. *J Physiol, 557*(Pt 1), 207-228. doi:10.1113/jphysiol.2003.060509

Swadlow, H. A., & Waxman, S. G. (2012). Axonal conduction delays. *Scholarpedia, 7*(6), 1451.

Tabares, L., Ruiz, R., Linares-Clemente, P., Gaffield, M. A., Alvarez de Toledo, G., Fernandez-Chacon, R., & Betz, W. J. (2007). Monitoring synaptic function at the neuromuscular junction of a mouse expressing synaptopHluorin. *J Neurosci, 27*(20), 5422-5430. doi:10.1523/JNEUROSCI.0670-07.2007

Takahashi, M., Seagar, M. J., Jones, J. F., Reber, B. F., & Catterall, W. A. (1987). Subunit structure of dihydropyridine-sensitive calcium channels from skeletal muscle. *Proc Natl Acad Sci U S A, 84*(15), 5478-5482. doi:10.1073/pnas.84.15.5478

Takamori, M. (2008). Lambert-Eaton myasthenic syndrome: search for alternative autoimmune targets and possible compensatory mechanisms based on presynaptic calcium homeostasis. *J Neuroimmunol, 201-202*, 145-152. doi:10.1016/j.jneuroim.2008.04.040

Takamori, M., Hamada, T., Komai, K., Takahashi, M., & Yoshida, A. (1994). Synaptotagmin can cause an immune-mediated model of Lambert-Eaton myasthenic syndrome in rats. *Ann Neurol, 35*(1), 74-80. doi:10.1002/ana.410350112

Takamori, M., Iwasa, K., & Komai, K. (1998). Antigenic sites of the voltage-gated calcium channel in Lambert-Eaton myasthenic syndrome. *Ann N Y Acad Sci, 841*, 625-635. doi:10.1111/j.1749-6632.1998.tb10994.x

Takamori, M., Komai, K., & Iwasa, K. (2000a). Antibodies to calcium channel and synaptotagmin in Lambert-Eaton myasthenic syndrome. *Am J Med Sci, 319*(4), 204-208. doi:10.1097/00000441-200004000-00002

Takamori, M., Maruta, T., & Komai, K. (2000b). Lambert-Eaton myasthenic syndrome as an autoimmune calcium-channelopathy. *Neurosci Res, 36*(3), 183-191. doi:10.1016/s0168-0102(99)00135-2

Takamori, M., Takahashi, M., Yasukawa, Y., Iwasa, K., Nemoto, Y., Suenaga, A., . . . Nakamura, T. (1995). Antibodies to recombinant synaptotagmin and calcium channel subtypes in Lambert-Eaton myasthenic syndrome. *J Neurol Sci, 133*(1-2), 95-101. doi:10.1016/0022-510x(95)00162-u

Tanabe, T., Takeshima, H., Mikami, A., Flockerzi, V., Takahashi, H., Kangawa, K., . . . Numa, S. (1987). Primary structure of the receptor for calcium channel blockers from skeletal muscle. *Nature, 328*(6128), 313-318. doi:10.1038/328313a0

Tarr, T. B., Dittrich, M., & Meriney, S. D. (2013a). Are unreliable release mechanisms conserved from NMJ to CNS? *Trends Neurosci, 36*(1), 14-22. doi:10.1016/j.tins.2012.09.009

Tarr, T. B., Lacomis, D., Reddel, S. W., Liang, M., Valdomir, G., Frasso, M., . . . Meriney, S. D. (2014). Complete reversal of Lambert-Eaton myasthenic syndrome synaptic impairment by the combined use of a K+ channel blocker and a Ca2+ channel agonist. *J Physiol, 592*(16), 3687-3696. doi:10.1113/jphysiol.2014.276493

Tarr, T. B., Malick, W., Liang, M., Valdomir, G., Frasso, M., Lacomis, D., . . . Meriney, S. D. (2013b). Evaluation of a novel calcium channel agonist for therapeutic potential in Lambert-Eaton myasthenic syndrome. *J Neurosci, 33*(25), 10559-10567. doi:10.1523/JNEUROSCI.4629-12.2013

Taschenberger, H., Leao, R. M., Rowland, K. C., Spirou, G. A., & von Gersdorff, H. (2002). Optimizing synaptic architecture and efficiency for high-frequency transmission. *Neuron, 36*(6), 1127-1143. doi:10.1016/s0896-6273(02)01137-6

Taschenberger, H., & von Gersdorff, H. (2000). Fine-tuning an auditory synapse for speed and fidelity: developmental changes in presynaptic waveform, EPSC kinetics, and synaptic plasticity. *J Neurosci*, *20*(24), 9162-9173.

Thakkar, N., Guptill, J. T., Ales, K., Jacobus, D., Jacobus, L., Peloquin, C., . . . Group, D. S. (2017). Population Pharmacokinetics/Pharmacodynamics of 3,4-Diaminopyridine Free Base in Patients With Lambert-Eaton Myasthenia. *CPT Pharmacometrics Syst Pharmacol, 6*(9), 625-634. doi:10.1002/psp4.12218

Thurtell, M. J., & Leigh, R. J. (2012). Treatment of Nystagmus. *Current Treatment Options in Neurology, 14*(1), 60-72. doi:10.1007/s11940-011-0154-5

Tim, R. W., Massey, J. M., & Sanders, D. B. (2000). Lambert-Eaton myasthenic syndrome: electrodiagnostic findings and response to treatment. *Neurology, 54*(11), 2176-2178. doi:10.1212/wnl.54.11.2176

Titulaer, M. J., Klooster, R., Potman, M., Sabater, L., Graus, F., Hegeman, I. M., . . . Verschuuren, J. J. (2009). SOX antibodies in small-cell lung cancer and Lambert-Eaton myasthenic syndrome: frequency and relation with survival. *J Clin Oncol, 27*(26), 4260-4267. doi:10.1200/JCO.2008.20.6169

Titulaer, M. J., Lang, B., & Verschuuren, J. J. (2011a). Lambert-Eaton myasthenic syndrome: from clinical characteristics to therapeutic strategies. *Lancet Neurol, 10*(12), 1098-1107. doi:10.1016/S1474-4422(11)70245-9

Titulaer, M. J., Maddison, P., Sont, J. K., Wirtz, P. W., Hilton-Jones, D., Klooster, R., . . . Verschuuren, J. J. (2011b). Clinical Dutch-English Lambert-Eaton Myasthenic syndrome (LEMS) tumor association prediction score accurately predicts small-cell lung cancer in the LEMS. *J Clin Oncol, 29*(7), 902-908. doi:10.1200/JCO.2010.32.0440

Titulaer, M. J., & Verschuuren, J. J. (2008). Lambert-Eaton myasthenic syndrome: tumor versus nontumor forms. *Ann N Y Acad Sci, 1132*, 129-134. doi:10.1196/annals.1405.030

Tremblay, J. P., Robitaille, R., & Grenon, G. (1984). Distribution of spontaneous release along the frog neuromuscular junction. *Neurosci Lett, 51*(2), 247-252. doi:10.1016/0304-3940(84)90559-7

Tseng, Q., Duchemin-Pelletier, E., Deshiere, A., Balland, M., Guillou, H., Filhol, O., & Thery, M. (2012). Spatial organization of the extracellular matrix regulates cell-cell junction positioning. *Proc Natl Acad Sci U S A, 109*(5), 1506-1511. doi:10.1073/pnas.1106377109

Tseng, Q., Wang, I., Duchemin-Pelletier, E., Azioune, A., Carpi, N., Gao, J., . . . Balland, M. (2011). A new micropatterning method of soft substrates reveals that different tumorigenic signals can promote or reduce cell contraction levels. *Lab Chip, 11*(13), 2231-2240. doi:10.1039/c0lc00641f

Tsien, R. W. (1983). Calcium channels in excitable cell membranes. *Annu Rev Physiol, 45*, 341-358. doi:10.1146/annurev.ph.45.030183.002013

Tsien, R. W., Lipscombe, D., Madison, D. V., Bley, K. R., & Fox, A. P. (1988). Multiple types of neuronal calcium channels and their selective modulation. *Trends Neurosci, 11*(10), 431-438. doi:10.1016/0166-2236(88)90194-4

Tsuchitani, C. (1997). Input from the medial nucleus of trapezoid body to an interaural level detector. *Hear Res, 105*(1-2), 211-224. doi:10.1016/s0378-5955(96)00212-2

Urbano, F. J., Piedras-Renteria, E. S., Jun, K., Shin, H. S., Uchitel, O. D., & Tsien, R. W. (2003). Altered properties of quantal neurotransmitter release at endplates of mice lacking P/Q-type Ca2+ channels. *Proc Natl Acad Sci U S A, 100*(6), 3491-3496. doi:10.1073/pnas.0437991100

Urbano, F. J., Rosato-Siri, M. D., & Uchitel, O. D. (2002). Calcium channels involved in neurotransmitter release at adult, neonatal and P/Q-type deficient neuromuscular junctions (Review). *Molecular membrane biology, 19*(4), 293-300. doi:10.1080/0968768021000035087 PMID - 12512776

Vatanpour, H., & Harvey, A. L. (1995). Modulation of acetylcholine release at mouse neuromuscular junctions by interaction of three homologous scorpion toxins with K+ channels. *Br J Pharmacol, 114*(7), 1502-1506. doi:10.1111/j.1476-5381.1995.tb13377.x

Vega-Saenz de Miera, E., Moreno, H., Fruhling, D., Kentros, C., & Rudy, B. (1992). Cloning of ShIII (Shaw-like) cDNAs encoding a novel high-voltage-activating, TEA-sensitive, type-A K+ channel. *Proc Biol Sci, 248*(1321), 9-18. doi:10.1098/rspb.1992.0036

Vincent, A., Lang, B., & Newsom-Davis, J. (1989). Autoimmunity to the voltage-gated calcium channel underlies the Lambert-Eaton myasthenic syndrome, a paraneoplastic disorder. *Trends Neurosci, 12*(12), 496-502. doi:10.1016/0166-2236(89)90109-4

Voelker, R. (2019). Drug Approved for Rare Muscle Weakening Syndrome. *JAMA, 321*(3), 239. doi:10.1001/jama.2018.21321

Wachman, E. S., Poage, R. E., Stiles, J. R., Farkas, D. L., & Meriney, S. D. (2004). Spatial Distribution of Calcium Entry Evoked by Single Action Potentials within the Presynaptic Active Zone. *J Neurosci, 24*(12), 2877-2885. doi:10.1523/JNEUROSCI.1660-03.2004

Wang, L. Y., Gan, L., Forsythe, I. D., & Kaczmarek, L. K. (1998). Contribution of the Kv3.1 potassium channel to high-frequency firing in mouse auditory neurones. *J Physiol, 509 (Pt 1),* 183-194. doi:10.1111/j.1469-7793.1998.183bo.x

Wang, X., Pinter, M. J., & Rich, M. M. (2010). Ca2+ dependence of the binomial parameters p and n at the mouse neuromuscular junction. *J Neurophysiol, 103*(2), 659-666. doi:10.1152/jn.00708.2009

Whittaker, R. G., Herrmann, D. N., Bansagi, B., Hasan, B. A., Lofra, R. M., Logigian, E. L., . . . Lochmuller, H. (2015). Electrophysiologic features of SYT2 mutations causing a treatable neuromuscular syndrome. *Neurology, 85*(22), 1964-1971. doi:10.1212/WNL.0000000000002185

Wigmore, M. A., & Lacey, M. G. (2000). A Kv3-like persistent, outwardly rectifying, Cs+-permeable, K+ current in rat subthalamic nucleus neurones. *J Physiol, 527 Pt 3,* 493-506. doi:10.1111/j.1469-7793.2000.t01-1-00493.x

Wirtz, P. W., Smallegange, T. M., Wintzen, A. R., & Verschuuren, J. J. (2002). Differences in clinical features between the Lambert-Eaton myasthenic syndrome with and without cancer: an analysis of 227 published cases. *Clin Neurol Neurosurg, 104*(4), 359-363. doi:10.1016/s0303-8467(02)00054-9

Wirtz, P. W., Titulaer, M. J., Gerven, J. M., & Verschuuren, J. J. (2010). 3,4-diaminopyridine for the treatment of Lambert-Eaton myasthenic syndrome. *Expert Rev Clin Immunol, 6*(6), 867-874. doi:10.1586/eci.10.57

Wirtz, P. W., Verschuuren, J. J., van Dijk, J. G., de Kam, M. L., Schoemaker, R. C., van Hasselt, J. G., . . . van Gerven, J. M. (2009). Efficacy of 3,4-diaminopyridine and pyridostigmine in the treatment of Lambert-Eaton myasthenic syndrome: a randomized, double-blind, placebo-controlled, crossover study. *Clin Pharmacol Ther, 86*(1), 44-48. doi:10.1038/clpt.2009.35

Witting, N., Crone, C., Duno, M., & Vissing, J. (2015). Clinical and neurophysiological response to pharmacological treatment of DOK7 congenital myasthenia in an older patient. *Clin Neurol Neurosurg, 130,* 168-170. doi:10.1016/j.clineuro.2015.01.010

Wood, S. J., & Slater, C. R. (2001). Safety factor at the neuromuscular junction. *Prog Neurobiol, 64*(4), 393-429. doi:10.1016/s0301-0082(00)00055-1

Wu, M., White, H. V., Boehm, B. A., Meriney, C. J., Kerrigan, K., Frasso, M., . . . Meriney, S. D. (2018a). New Cav2 calcium channel gating modifiers with agonist activity and therapeutic potential to treat neuromuscular disease. *Neuropharmacology, 131*(P.N.A.S 111 2014), 176-189. doi:10.1016/j.neuropharm.2017.12.022

Wu, Z.-Z., Chen, S.-R., & Pan, H.-L. (2018b). Reply to Meriney and Lacomis: Comment on direct aminopyridine effects on voltage-gated Ca2+ channels. *Journal of Biological Chemistry, 293*(41), 16101-16101. doi:10.1074/jbc.rl118.005655 PMID - 30315088

Wu, Z.-Z., Li, D.-P., Chen, S.-R., & Pan, H.-L. (2009). Aminopyridines Potentiate Synaptic and Neuromuscular Transmission by Targeting the Voltage-activated Calcium Channel β Subunit. *Journal of Biological Chemistry, 284*(52), 36453-36461. doi:10.1074/jbc.m109.075523 PMID - 19850918

Wyatt, R. M., & Balice-Gordon, R. J. (2008). Heterogeneity in synaptic vesicle release at neuromuscular synapses of mice expressing synaptopHluorin. *J Neurosci, 28*(1), 325-335. doi:10.1523/JNEUROSCI.3544-07.2008

Xu, Y. F., Hewett, S. J., & Atchison, W. D. (1998). Passive transfer of Lambert-Eaton myasthenic syndrome induces dihydropyridine sensitivity of ICa in mouse motor nerve terminals. *J Neurophysiol, 80*(3), 1056-1069. doi:10.1152/jn.1998.80.3.1056

Yamada, W. M., & Zucker, R. S. (1992). Time course of transmitter release calculated from simulations of a calcium diffusion model. *Biophys J, 61*(3), 671-682. doi:10.1016/S0006-3495(92)81872-6

Yang, H., Zhang, G., & Cui, J. (2015). BK channels: multiple sensors, one activation gate. *Front Physiol, 6*, 29. doi:10.3389/fphys.2015.00029

Yang, Y. M., & Wang, L. Y. (2006). Amplitude and kinetics of action potential-evoked Ca2+ current and its efficacy in triggering transmitter release at the developing calyx of Held synapse. *J Neurosci, 26*(21), 5698-5708. doi:10.1523/JNEUROSCI.4889-05.2006

Yazejian, B., DiGregorio, D. A., Vergara, J. L., Poage, R. E., Meriney, S. D., & Grinnell, A. D. (1997). Direct measurements of presynaptic calcium and calcium-activated potassium currents regulating neurotransmitter release at cultured Xenopus nerve-muscle synapses. *J Neurosci, 17*(9), 2990-3001.

Yi, J. S., Guptill, J. T., Stathopoulos, P., Nowak, R. J., & O'Connor, K. C. (2018). B cells in the pathophysiology of myasthenia gravis. *Muscle Nerve, 57*(2), 172-184. doi:10.1002/mus.25973

Yokoyama, S., Imoto, K., Kawamura, T., Higashida, H., Iwabe, N., Miyata, T., & Numa, S. (1989). Potassium channels from NG108-15 neuroblastoma-glioma hybrid cells. Primary structure and functional expression from cDNAs. *FEBS Lett*, *259*(1), 37-42. doi:10.1016/0014-5793(89)81488-7

Yoon, C. H., Owusu-Guha, J., Smith, A., & Buschur, P. (2020). Amifampridine for the Management of Lambert-Eaton Myasthenic Syndrome: A New Take on an Old Drug. *Ann Pharmacother, 54*(1), 56-63. doi:10.1177/1060028019864574

Zalewski, N. L., Lennon, V. A., Lachance, D. H., Klein, C. J., Pittock, S. J., & McKeon, A. (2016). P/Q- and N-type calcium-channel antibodies: Oncological, neurological, and serological accompaniments. *Muscle Nerve, 54*(2), 220-227. doi:10.1002/mus.25027

Zefirov, A. L., & Khalilov, I. A. (1985). [Characteristics of electrical activity in different sections of nerve endings in the frog]. *Biull Eksp Biol Med, 99*(1), 7-10.

Zemel, B. M., Ritter, D. M., Covarrubias, M., & Muqeem, T. (2018). A-Type KV Channels in Dorsal Root Ganglion Neurons: Diversity, Function, and Dysfunction. *Front Mol Neurosci, 11*, 253. doi:10.3389/fnmol.2018.00253

Zhong, N., & Zucker, R. S. (2005). cAMP acts on exchange protein activated by cAMP/cAMP-regulated guanine nucleotide exchange protein to regulate transmitter release at the crayfish neuromuscular junction. *J Neurosci*, *25*(1), 208-214. doi:10.1523/JNEUROSCI.3703-04.2005